Dark Halos of Wide Triple Systems of Galaxies

V. P. Dolgachev[1], L. M. Domozhilova[1], and A. D. Chernin[1,2]

[1]*Sternberg Astronomical Institute, Universitetskiĭ pr. 13, Moscow, 119899 Russia*

[2]*Tuorla Observatory, Turku, Finland*

Received July 10, 2001

Abstract—A new class of metagalactic system—wide triple systems of galaxies with characteristic scale lengths of ∼1 Mpc—are analyzed. Dynamical models of such systems are constructed, and the amount of dark mass contained in them is estimated. In principle, kinematic data for wide triplets allow two types of models: with individual galactic halos and with a common halo for the entire system. A choice between the two models can be made based on X-ray observations of these systems, which can determine whether clustering and hierarchical evolution continues on scales of ∼1 Mpc or whether systems with such scale lengths are in a state of virial quasi-equilibrium. © *2002 MAIK "Nauka/Interperiodica"*.

1. INTRODUCTION

Wide galaxy triplets represent a new class of metagalactic system. The first (and so far only) list of these objects was published by Trofimov and Chernin [1]. This list contains data for 108 systems, of which one third are "likely physically associated" systems, according to the statistical criterion of Anosova [2]. The characteristic size of these systems is close to 1 Mpc, much greater than the sizes of compact galaxy triplets studied by Karachentsev's group at the Special Astrophysical Observatory ($\simeq 0.05$ Mpc) [3−5]. We accordingly we refer to systems in our list as wide and those studied by Karachentsev's group as compact triplets. A detailed comparative analysis of wide and compact galaxy triplets can be found in the review by Geller and Huchra [6].

Studies of wide galaxy triplets can shed new light on a number of fundamental problems in astronomy and cosmology. One is the formation and dynamical evolution of cosmic structures with various scale lengths. This is closely related to the problem (at least as important) of hidden mass in various galaxy systems. What is the mass of dark matter in systems with spatial scale lengths ∼1 Mpc? What is the distribution of this mass: is it concentrated in individual galactic halos, or does it form common halos for the triplet systems as a whole? The answers to these questions have a bearing on important evolutionary questions. Is there an ongoing process of clustering and hierarchical evolution on scale lengths of ∼1 Mpc? Or are systems with such scale lengths in a state of virial quasi-equilibrium?

In this work, we use numerical simulations to analyze both alternatives for wide triplets: (1) galaxies with individual halos and (2) galaxies moving in a common quasi-stationary halo for the entire system. The kinematic data on wide triplets that we use as the initial observations for our simulations can be interpreted and reproduced (with almost equal accuracy) in terms of both types of models. This raises the question of new observations that could distinguish between alternative models, and thereby provide definitive answers to the evolutionary questions indicated above.

We propose the X-ray structure of wide triplets as a critical observational test. X-ray observations of the systems considered could make it possible to establish whether the X-ray flux (emitted by hot gas) comes from the halos of individual galaxies or from a common halo for the system as a whole.

2. WIDE TRIPLETS OF GALAXIES: PRINCIPAL PARAMETERS

As a dynamical system, a galaxy triplet can be characterized by its mean radial velocity

$$\langle V \rangle = \sum V_k / 3, \quad k = 1, 2, 3; \tag{1}$$

where V_k is the radial velocity of a component of the triplet corrected for the solar motion and the rms velocity of a triplet component after subtraction of the mean velocity is

$$\sigma_r = [(1/3) \sum (V_k - \langle V \rangle)^2]^{1/2}, \tag{2}$$
$$k = 1, 2, 3.$$

The distance between two galaxies in a triplet is

$$R_{ik} = x_{ik} \langle V \rangle H^{-1}, \tag{3}$$

Table 1. Observed parameters of triple systems of galaxies

Systems	σ_r, km/s	r_h, kpc	τ	v, km/s	r, kpc
Compact	101	$43h^{-1}$	0.07	172	$51h^{-1}$
Wide	84	$556h^{-1}$	0.96	143	$668h^{-1}$

where x_{ik} is the angular separation between the two components and H is the Hubble constant. The harmonic mean distance between the components is

$$r_h = [(1/3) \sum R_{ik}^{-1}]^{-1}, \qquad (4)$$
$$i, k = 1, 2, 3, i \neq k.$$

The dimensionless crossing time normalized to the Hubble time (H^{-1}) is

$$\tau = 2H(r_h/\sigma_r). \qquad (5)$$

The projections σ_r and r_h are statistically related to the three-dimensional parameters σ and r by the formulas

$$\sigma = \sqrt{3}\sigma_r, \quad r = (2/\sqrt{3})r_h. \qquad (6)$$

As a source of observational data on galaxy triplets, we used the original catalog of Karachentsev *et al.* [3], which contains 84 compact triplets, and catalog [1], which contains 108 wide triplets and is based on catalogs of galaxy groups in the Northern [6] and Southern [7] skies.

According to the rigorous isolation criterion of [2], 46 compact and 38 wide triplets appear to be physically bound.

Table 1 gives the median values of the main parameters of the probable physical triplets: the velocity dispersion σ_r(km/s), mean harmonic distance r_h of the triplet (kpc), dimensionless crossing time τ, three-dimensional velocities V, and r values computed according to (6). We used a normalized Hubble constant of $h = H/75$ km s^{-1} Mpc^{-1}.

Both wide and compact triplets consist primarily of giant galaxies with luminous masses of $M_h = (1-2) \times 10^{11} M_\odot$.

Compact and wide triplets have appreciably different physical parameters. The most conspicuous of these is their sizes, which differ by more than an order of magnitude. Compact systems are so small that their sizes are comparable to (or possibly smaller than) the radius of the dark halo surrounding giant galaxy. Therefore, these galaxies do not interact at all like three point masses. In contrast, the mutual distances between galaxies in wide triplets are much greater than the radius of the halo of a single galaxy, and the systems can be adequately described using a three-body model, at least as a first approximation [8].

The second difference is no less important. As is evident from Table 1, the dimensionless crossing times for compact triplets are an order of magnitude less than unity, whereas the crossing times for wide triplets are close to unity. A dimensionless crossing time of $\tau \sim 0.1$ implies that the galaxies must have made at least several crossings during the lifetime of the system, making it feasible for the system to attain virial equilibrium. When $\tau \sim 1$, (as for wide triplets), the system is dynamically young and in a state that is far from virialization.

It is well known that the most reliable determinations of luminous and dark masses can be made for systems with extreme sizes: rich clusters and isolated galaxies [9]. On the contrary, estimating the masses of groups of galaxies is a very difficult task, for two reasons: (1) the observational data used to estimate the masses are neither varied nor numerous, and usually include only the line-of-sight velocity and angular separation between the components of the system, and (2) there is no well-developed theory for the derivation of the total mass of a system based on its kinematic characteristics.

The mass extremator for groups is usually used, defined by the following virial relation:

$$M_{\mathrm{vir}} = \alpha(V^2 R/G), \qquad (7)$$

where M_{vir} is the virial mass of the system, V the characteristic velocity (line-of-sight velocity dispersion referred to the system barycenter), R the size of the system (mean harmonic distance between the system components), G the gravitational constant, and α a dimensionless factor. It is usually assumed that α can be derived from the virial theorem, taking into account the effects of projection. This approach yields (see, e.g., [10])

$$\alpha = 9\pi/2. \qquad (8)$$

Numerical simulations have shown that this extremator can indeed work (statistically for ensembles of groups [11], if not for individual groups), provided that the systems and their ensembles are in virial equilibrium.

The relative contribution of dark matter is usually characterized by the mass/luminosity ratio (M/L). For rich clusters and galactic halos, this ratio is

$$M/L = 300h M_\odot/L_\odot \qquad (9)$$

and

$$M/L = 30 - 100 M_\odot/L_\odot, \qquad (10)$$

respectively. These results show that the mass of dark matter exceeds that of luminous matter by factors of 3–10 and 10–50 in galaxies and rich clusters, respectively, if we assume that $M/L \approx 10$ in solar units for galaxies of all types. On average, the mass/luminosity

ratio increases with the scale length of the system. This was first established by Karachentsev [12] based on then-available data on double galaxies and groups, clusters, and superclusters of galaxies (see also [13]). See [10] for the current status of the problem and a list of references.

X-ray observations provide a new and very important tool for studying groups of galaxies (see [14, 15] and references therein). By measuring the temperature of the X-ray-emitting gas and the volume filled by this gas, it is possible to estimate the total mass of the group using an extremator that is essentially the virial extremator, as long as the group is in virial equilibrium and the gas is in thermal and hydrostatic equilibrium in the potential well of the gravitational field of the group. This technique was used to calculate the masses of a dozen compact groups, which were found to be $\sim 10^{13} M_{\odot}$ [14].

Returning to the masses of galaxy triplets, we note that virial masses cannot be derived from the characteristic velocities and sizes of either type of triplet system, albeit for different reasons. The standard virial-mass extremator based on (7) and (8) is calculated assuming that the galaxies are point masses. However, this is not the case for compact triplets, since the gravitational potential of their members differs from that for a sum of point masses. On the other hand, the virial extremator assumes virial equilibrium, which is not valid for wide triplets of galaxies. Thus, although we can formally calculate the virial masses for compact and wide triplets using (7) and (8), these may differ substantially from the actual masses.

Zheng *et al.* [16] suggested a more self-consistent model for the mass distribution in compact systems. We ran computer simulations for models taking into account dynamical friction, tidal effects, and possible galaxy mergers. These models show that observed compact triplets (like close binaries [17]) result from the evolution of compact systems initially consisting of four to six components. Taking this into account, we obtained trustworthy estimates for the typical masses and mass/luminosity ratios for compact triplets:

$$M = 1.7 \times 10^{12} M_{\odot}, \qquad (11)$$
$$M/L = 50 \pm 20 M_{\odot}/L_{\odot}.$$

These results show that the dark (unseen) mass through which the compact triplet moves exceeds the luminous mass by a factor of three to seven [16].

When applied to compact triplets, the virial extremator (7) and (8) yields a virial mass of $M_{\mathrm{vir}} = 2.5 \times 10^{12} h^{-1} M_{\odot}$. The masses in formula (11) does not differ strongly from that given by the virial extremator. This is unlikely a coincidence and appears to indicate that the current dynamical condition of

the system of galaxies can be accurately described by the system's gravitational potential and depends only weakly on its previous history.

Note that kinematic estimates [as in Eq. (11)] yield only the mass of the system within the volume in which the galaxies move; the total mass of the common halo of a group could be significantly (an order of magnitude) higher than implied by X-ray observations of compact groups (see above). For wide triplets, the extremator in (7) and (8) yields $M_{\mathrm{vir}} = 1.5 \times 10^{12} h^{-1} M_{\odot}$. This is approximately equal to (or smaller than) the masses of compact triplets within the volume in which the galaxies move. We will see in the next section that the virial values severely underestimate the masses of wide triplets. Realistic estimates for the masses of such systems can be obtained via numerical simulations of their dynamics. It is also important that simulations can provide a clear picture of the dynamical states of such systems.

3. MODEL FOR INDIVIDUAL GALAXY HALOS

Our numerical simulations of wide triplets are based on two important observational facts: (1) wide triplets are dynamically young objects and (2) they are in a state far from virial equilibrium. We further assume that the components of a triplet were at rest 12 ± 3 Gyr ago. This is essentially the same as the assumption made in a well known model of the Local Group [18], that the centers of mass of the two major galaxies of the group were at rest at a specified time in the past (≈ 10 Gyr ago). From a state of rest, the galaxies begin to approach each other under the influence of their mutual gravitational attraction. Models with the motion of several bodies with zero initial velocities are usually referred to as free-fall models. As in [18], we assume that the free-falling galaxies in a wide triplet can be treated like point masses. In both the Local Group and wide triplets, the distances between the galaxies are 600–800 kpc, which far exceeds the size of any galaxy, even including its halo. We further assume for the sake of simplicity that the galaxies in the triplet have equal masses. We regularize close encounters using a soft potential scheme, as in [19].

We computed a total of eight model versions, each involving the analysis of 60 different initial triangular configurations of the system. We followed the dynamical evolution of each model to 20 Gyr, but the dynamical state of the system in the interval 10–15 Gyr was fixed at 11 equidistant times. Each of the eight versions had different lengths for the sides of the initial triangle, which were in the range 1–3 Mpc (the distance between the Milky Way and the Andromeda Galaxy in the model of [18] when the two bodies

Table 2. Simulations of wide triplets. Model with individual galactic halos

Version	$M_i, 10^{12}M_\odot$	S, Mpc	v, km/s	r, kpc	τ	$M_{\text{vir}}, 10^{12}M_\odot$
1	0.3	1.438	24.3	967.8	0.9825	0.391
2	1	1.438	94.9	528.8	0.1350	0.329
3	3	1.438	134.2	666.6	0.1249	0.807
4	3	3	56.6	1932.5	0.8488	0.430
5	3	4	29.7	3193.0	2.6500	0.191
6	3	2	145.3	714.9	0.1087	1.003
7	3	2.25	119.3	936.4	0.1911	0.904
8	4	3	78.6	1715.5	0.5512	0.752

Table 3. Computed parameters of wide triplets: 10 samples consisting of 50 elements made up of merged versions $3 + 9$

Sample	v, km/s	r, kpc	τ	$M_{\text{vir}}, 10^{12}M_\odot$
1	145.9	665.5	0.688	1.091
2	160.8	640.2	1.504	0.818
3	150.7	675.4	1.455	0.759
4	147.2	631.0	1.036	0.974
5	145.5	656.2	1.350	0.989
6	130.8	730.6	1.061	0.948
7	149.0	767.0	1.486	0.941
8	134.6	709.7	1.291	0.919
9	126.8	686.2	0.938	0.973
10	115.6	688.6	0.688	0.823

were at rest), and different masses for the individual galaxies, which were in the range $(0.3-4)\times10^{13}M_\odot$. Our dataset contains a total of $8 \times 60 \times 11 = 5280$ snapshots of the states of the triplet. Each state is specified by five indices: the initial leg of the equilateral triangle S, mass of the bodies M_i, two numbers defining the initial configuration of the triangle, and the registration time t.

Table 2 gives the principal characteristics of the model states. The masses M_i of the system components and parameter S are given for the initial time. The median three-dimensional rms velocity of the system after subtraction of the mean velocity (3D) V and the three-dimensional mean harmonic distance r between the galaxies are ensemble parameters. Finally, the table gives the median dimensionless crossing time τ and virial mass. The notation for these parameters and their meanings follow from the formulas given in Section 2.

The first comment that arises from an analysis of Table 2 concerns the masses of the systems. The virial

masses M_{vir} of the systems based on the standard extremator (Section 2) were systematically smaller than the masses inferred in the numerical simulations. If the virial mass is $(0.2-1)\times10^{12}M_\odot$, the actual mass of the system should be $(0.9-12) \times10^{12}M_\odot$. It follows that the virial extremator appreciably underestimates the masses, and this is a general conclusion flowing from the numerical simulations.

It is evident from Table 2 that the rms velocity V varies from $24-150$ km/s, which includes the observed value of ≈140 km/s encountered in versions 3 and 6. We accordingly selected versions 3 and 6 for further statistical analysis. We combined these models into a single statistical set containing 1320 states. We then used a random-number generator to draw ten samples, each made up of 50 elements.

Table 3 shows the degree of proximity between the quantities obtained in this way and the observed values listed in Table 1. All samples represent the statistics of the 38 probable physical triplets fairly well: the differences between the observed values and the statistically computed dynamical characteristics in Table 3 never exceed $10-20\%$. This accuracy can be considered quite acceptable in view of the observational errors, especially the errors in the measured velocities of galaxies in groups.

(Curiously, the median values for r and V from Table 3, $r_{mm} = 686$ kpc and $V_{mm} = 146$ km/s, nearly coincide with the observed values.)

Note that not only the median r and V values agree with the observations: the observed distributions of these parameters also agree well with those produced by the numerical simulations. This is shown by Fig. 1, which presents the distributions of the rms velocity and mutual distances between galaxies for samples 3 and 9. The observed distributions (thin lines) are adopted from [1] (we converted σ_r and r_h into r and V using the formulas from Section 2).

In both model versions reflected in the samples in Table 3, the masses of the bodies were set equal
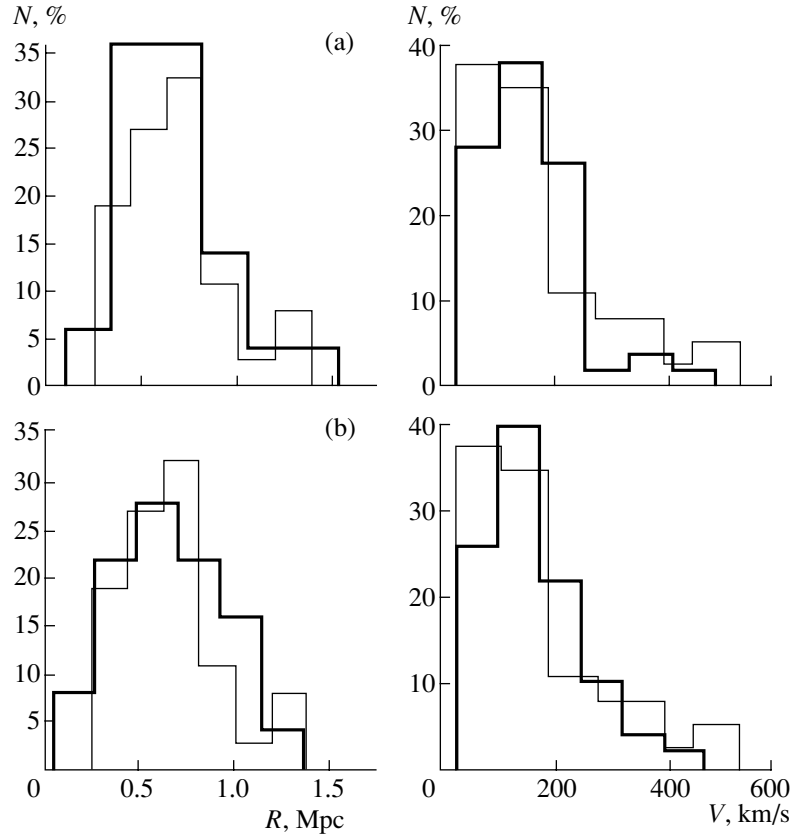
Fig. 1. Distribution of the mean harmonic distance and rms velocity for models with individual galaxy coronas for (a) sample 3 and (b) sample 9. The thin line shows the observations.

to $M_i = 3 \times 10^{12} M_\odot$. Consequently, the statistical estimate of the total mass for a typical wide triplet is

$$M = 9 \times 10^{12} M_\odot \approx 10^{13} M_\odot. \qquad (12)$$

4. MODEL WITH A COMMON HALO FOR THE SYSTEM

We have already pointed out that the dark matter in the systems of galaxies could be distributed either in individual halos of the member galaxies or in a common halo for the entire triplet system.

To make the structure of the halo more detailed, we will assume that the common halo of a triplet consists of a spherical core whose center coincides with that of the system and a spherical corona of variable density surrounding the core. The corona core is taken to have uniform density ρ_o, with the density of the corona varying as the inverse square of the barycentric distance r:

$$\rho = \rho_0 \left(\frac{r_0}{r}\right)^2, \quad \text{if} \quad r > r_0,$$

$$\rho = \rho_0, \qquad \qquad \text{if} \quad r < r_0.$$

We set the core radius equal to 20 kpc. Let us choose ρ_o so that the mass of the corona is equal to the

total mass of the triplet in the models described in Section 3 ($\approx 10^{13} M_\odot$), and the radius of the corona so that it does not exceed the initial length of the maximum side of the triangle made up by the three galaxies (in earlier versions), 2×10^6 pc. With these assumptions about the mass and radius of the corona, we find $\rho_o = 0.995 \times 10^{13} M_\odot/pc^3$. We will refer to this as the standard density. We adopt for our common-halo model the same initial conditions as in the free-fall model ($V_i^{(o)} = 0$, $i = 1, 2, 3$). The three bodies would then move in a fixed plane, and the differential equations of motion for the three bodies in a barycentric coordinate system in the core–corona scheme acquire the form

$$\begin{cases} \frac{d^2 x_1}{dt^2} = fm_2 \frac{x_2 - x_1}{\Delta_{12}^3} + fm_3 \frac{x_3 - x_1}{\Delta_{13}^3} - f \frac{\text{mc}(r_1)}{r_1^3} x_1 \\ \frac{d^2 y_1}{dt^2} = fm_2 \frac{y_2 - y_1}{\Delta_{12}^3} + fm_3 \frac{y_3 - y_1}{\Delta_{13}^3} - f \frac{\text{mc}(r_1)}{r_1^3} y_1 \\ \frac{d^2 x_2}{dt^2} = fm_1 \frac{x_1 - x_2}{\Delta_{12}^3} + fm_3 \frac{x_3 - x_2}{\Delta_{23}^3} - f \frac{\text{mc}(r_2)}{r_2^3} x_2 \\ \frac{d^2 y_2}{dt^2} = fm_1 \frac{y_1 - y_2}{\Delta_{12}^3} + fm_3 \frac{y_3 - y_2}{\Delta_{23}^3} - f \frac{\text{mc}(r_2)}{r_2^3} y_2 \\ \frac{d^2 x_3}{dt^2} = fm_1 \frac{x_1 - x_3}{\Delta_{13}^3} + fm_2 \frac{x_2 - x_3}{\Delta_{23}^3} - f \frac{\text{mc}(r_3)}{r_3^3} x_3 \\ \frac{d^2 y_3}{dt^2} = fm_1 \frac{y_1 - y_3}{\Delta_{13}^3} + fm_2 \frac{y_2 - y_3}{\Delta_{23}^3} - f \frac{\text{mc}(r_3)}{r_3^3} y_3, \end{cases}$$

$$(13)$$
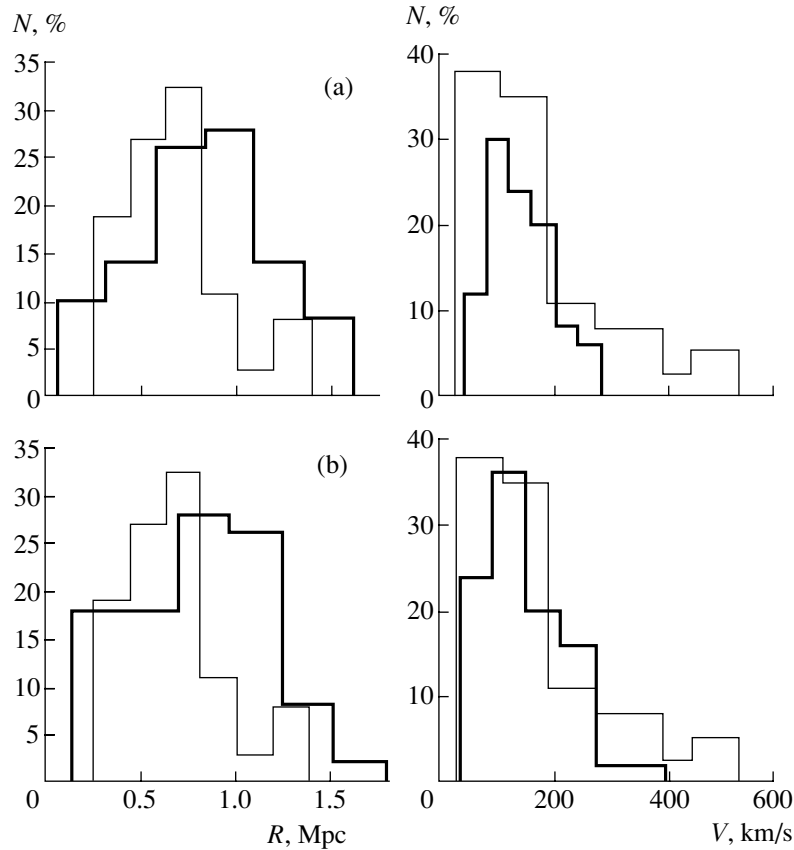
Fig. 2. Distribution of harmonic mean distance and rms velocity for models with a common corona around the triplet for (a) sample 3 and (b) sample 4. The thin line shows the observations.

where x_i, y_i, and m_i are the barycentric coordinates and mass of the body P_i $(i = 1, 2, 3)$, f is the gravitational constant, Δ_{ij} are the distances between bodies P_i and P_j, $\mathrm{mc}(r_i) = 3.3343 \times 10^9 + 5.001416 \times 10^6 r_i$ $(i = 1, 2, 3)$, and r_i is the barycentric radius vector of the body P_i.

The results of the numerical integration are described below.

Table 4 gives the principal parameters of numerical models for the wide triplets derived from an analysis of the eight model versions. These are characterized by the initial masses of the triplet components M_i, initial leg of the equilateral right triangle made up by the three bodies S, median rms velocity V, mean harmonic distance r, crossing time τ, and virial mass M_{vir}. These parameter values were computed for a 12–15 Gyr time interval.

An analysis of Table 4 in terms of the closeness of the median r and V to the observed values indicates that model versions 3, 4, 8, and 9 are the most acceptable. (The range of corona densities and masses in these versions span a factor of three.) For further statistical reduction, we combined these versions into a single dataset. We computed 60 trajectories for the

three-body system in each version. We chose four points on each trajectory in a 12–15 Gyr time interval. In this way, we finally obtained a dataset containing a total of $4 \times 4 \times 60 = 960$ states.

We further reduced the dataset using the same scheme as in Section 3. The results are summarized in Table 5. Figure 2 shows the histograms for the two best versions of the common-corona model. The bold lines show the results of the numerical simulations and thin lines the observations.

5. CONCLUSIONS: X-RAY OBSERVATIONS—A CRITICAL TEST

As is evident from Table 5 and Fig. 2, the common-halo models (Section 4) can reproduce the observational data nearly as well as models with individual galactic halos (Section 3). The discrepancies with the observations are slightly greater for the common-corona model but are not large enough to justify discarding these models in favor of models with individual halos. Given the observational errors, both models are acceptable as far as the available data on the kinematic and geometric properties of real systems are concerned.

Table 4. Median values of the parameters of wide triplets. Common-halo model

Version	M_i, $10^{12} M_\odot$	S, Mpc	ρ	v, km/s	r, kpc	τ	$M_{\rm vir}$, $10^{12} M_\odot$
1	0.3	1.438	ρ_0	104.6	1054	0.994	2.62
2	3	1.438	ρ_0	174.5	751	0.481	5.15
3	1	1.438	ρ_0	126.6	942	0.766	2.99
4	3	1.438	$1/3\rho_0$	114.6	834	0.693	2.62
5	0.3	2	ρ_0	124.8	1175	0.908	4.43
6	3	2	ρ_0	147.2	1159	0.818	4.98
7	1	2	ρ_0	141.4	1110	0.742	5.10
8	3	2	$1/3\rho_0$	227.5	524	0.223	6.24

Additional observational data are required to distinguish between the two types of models. We believe that X-ray observations of wide triplets of galaxies could serve as a critical test. X-ray observations of clusters and groups of galaxies have become an important source of data on the hidden masses in these systems [14, 15, 20–24]. Diffuse X-ray emission is produced by hot intergalactic gas filling the gravitational potential wells of clusters and groups and carries information about the spatial structure of these systems, as well as the amount of hidden mass in them. X-ray observations of clusters and groups of galaxies have been obtained using high-sensitivity, high-spatial-resolution instruments operating at soft energies of 0.1–3 keV, such as those aboard the CHANDRA and XMM NEWTON space observatories. These same X-ray telescopes are suitable for observations of the X-ray emission of wide triplets of galaxies.

Assuming that the hot X-ray gas is in hydrostatic and thermodynamic equilibrium in the gravitational field of the dark halos, we can estimate its temperature using the virial-type relation [23] $T{\rm keV} \simeq 0.1\alpha \frac{M}{10^{12} M_\odot}(R/100 \text{ kpc})^{-1}$, where M, R are the halo mass and radius. The dimensionless factor $\alpha = 1$–0.3 depends on the mass distribution in the halo and can be determined from observations of the surface brightness of the source. In the case of individual halos with masses $M \simeq 10^{12} M_\odot$ and sizes $R \simeq 100$ kpc, this formula yields $T \simeq 0.1$–0.3 keV. Since the temperature is proportional to the mass-to-size ratio of the system, more or less the same value is obtained for a triplet with a common corona. The inferred temperature is close to those of the X-ray halos of giant isolated galaxies. (The temperatures of compact groups with up to 30–100 galaxies are somewhat higher, about 1 keV; even higher temperatures, up to 10 keV, characterize the X-ray halos of the richest clusters of galaxies.) Triplets of both types

Table 5. Computed statistics of wide triplets with a common halo: 10 samples of 50 elements from merged versions 3 + 4

Version	v, km/s	r, kpc	τ	$M_{\rm vir}$, $10^{12} M_\odot$
1	140.0	903.5	0.6460	3.865
2	145.7	895.6	0.6250	3.740
3	134.3	842.5	0.7130	3.425
4	138.3	807.4	0.6100	4.460
5	147.9	967.5	0.5690	3.310
6	136.8	938.2	0.6320	4.095
7	147.6	715.7	0.6390	4.695
8	140.0	940.3	0.5285	4.240
9	143.6	902.2	0.5810	3.015
10	135.3	972.0	0.5820	4.255

are expected to have X-ray brightness in the range $B_x \simeq 10^{-10}$–10^{-12} erg/cm^2.

Despite their similar temperatures and X-ray surface brightnesses, the two types of possible wide triplets considered should have different spatial structures. In the case of individual galactic halos, the X-ray emission should be concentrated toward the galaxies and the extended source should exhibit a three-component structure. If the triplet has a common corona, its X-ray emission should be concentrated toward the center of mass of the system and not toward the individual galaxies. If the angular resolution is sufficient (say, $10'$ or better), this difference between the spatial structures should be clearly detectable. Thus, X-ray observations can be expected to resolve the problem of the distribution of hidden mass in wide triplets of galaxies.

In addition, distinguishing between the two models for wide triplets will make it possible to draw

more general conclusions concerning the dynamics and evolutionary status of cosmic structures with spatial scale lengths of ~ 1 Mpc and mass scales of $\sim 10^{13} M_\odot$; i.e., it will become clear whether these structures are in a state of ongoing formation via gravitational hierarchical clustering and free collapse or whether they have already reached a steady state and virial quasi-equilibrium. In turn, new constraints may help further refine our understanding of the formation of observed cosmic structures.

REFERENCES

1. A. V. Trofimov and A. D. Chernin, Astron. Zh. **72**, 308 (1995) [Astron. Rep. **39**, 272 (1995)].
2. Zh. P. Anosova, Astrophys. J. **26–27**, 653 (1988).
3. I. D. Karachentsev, V. E. Karachentseva, and V. S. Lebedev, Izv. Spets. Astrofiz. Obs. **27**, 67 (1989).
4. I. D. Karachentsev, V. E. Karachentseva, and A. I. Shcherbanovskiĭ, Izv. Spets. Astrofiz. Obs. **19**, 3 (1985).
5. I. D. Karachentsev, V. E. Karachentseva, and A. I. Shcherbanovskiĭ, Izv. Spets. Astrofiz. Obs. **11**, 3 (1979).
6. M. J. Geller and J. P. Huchra, Astrophys. J., Suppl. Ser. **52**, 61 (1983).
7. M. A. G. Maia, L. N. da Costa, and D. W. Latham, Astrophys. J., Suppl. Ser. **69**, 809 (1989).
8. V. P. Dolgachev and A. D. Chernin, Astron. Zh. **74**, 328 (1997) [Astron. Rep. **41**, 284 (1997)].
9. N. A. Bahcall, L. M. Lubin, and V. Dorman, Astrophys. J. Lett. **447**, L81 (1995).
10. J. Binney and S. Tremaine, *Galactic Dynamics* (Princeton Univ. Press, Princeton, 1987).
11. M. J. Valtonen, Vistas Astron. **32**, 23 (1988).
12. I. D. Karachentsev, Astrofizika **2**, 82 (1966).
13. I. D. Karachentsev, Astron. Astrophys. Trans. **6**, 1 (1994).
14. J. S. Mulchaey, AIP Conf. Proc. **336**, 243 (1995).
15. A. I. Zabludoff and J. S. Mulchaey, Astrophys. J. Lett. **498**, L5 (1998).
16. J.-Q. Zheng, M. J. Valtonen, and A. D. Chernin, Astron. J. **105**, 2047 (1993).
17. S. Wiren, J.-Q. Zheng, M. J. Valtonen, and A. D. Chernin, Astron. J. **111**, 160 (1996).
18. F. D. Kahn and L. Voltjer, Astrophys. J. **130**, 705 (1959).
19. S. J. Aareth, Mon. Not. R. Astron. Soc. **126**, 223 (1963).
20. L. P. David, C. Jones, W. Forman, and S. Daines, Astrophys. J. **428**, 544 (1994).
21. J. S. Mulchaey and A. I. Zabludov, Astrophys. J. **496**, 73 (1998).
22. A. I. Zabludov and J. S. Mulchaey, Astrophys. J. **496**, 39 (1998).
23. J. S. Mulchaey, Annu. Rev. Astron. Astrophys. **338**, 289 (2000).
24. A. D. Chernin, V. P. Dolgachev, and L. M. Domozhilova, Mon. Not. R. Astron. Soc. **319**, 851 (2000).

Translated by A. Dambis

Spatial Structure of the Old Open Cluster NGC 2420

Z. I. Peikov[1], R. M. Rusev[1], and T. Ruseva[2]

[1]St. Climent Okhridsky Sofia University, Sofia, Bulgaria

[2]Institute of Astronomy, Sofia, Bulgaria

Received April 14, 2000

Abstract—The spatial structure of the intermediate and outer regions of the old open cluster NGC 2420 is analyzed using data from the catalog of Paparó. The differential and integrated distributions of the projected [$\Delta F(r)$ and $F(r)$] and spatial [$\Delta f(r)$ and $f(r)$] stellar densities are obtained for various subsystems of cluster stars using Kholopov's star-count method. Analysis of these curves shows that: (1) the cluster has at least three distinct spatial zones with different stellar-density gradients, (2) the each cluster subsystem has a layered structure, and (3) the spatial structure of the cluster changes systematically in the transition to subsystems containing fainter main-sequence stars. Empirical relations describing the structure of the cluster are also derived. Similar structural features can also be found in other globular and open clusters. © *2002 MAIK "Nauka/Interperiodica".*

1. INTRODUCTION

Our studies of the deep spatial structure of a number of globular and open clusters—M56 [1] , M12 [2] , NGC 6535 [3] , NGC 6171 [4], NGC 5466 [5], M 92 [6], the Pleiades, Praesepe, and Coma Berenices [7]—have enabled us to detect and analyze systematic changes in the cluster structures as a function of the limiting magnitude of faint-star subsystems of the clusters. This effect is visible below the transition region between the subgiant branch and the main-sequence turnoff on the (V, $B-V$) diagrams for the clusters and is manifest as an increase in the radii of spatial zones of the clusters and a change in the radial stellar densities with increasing limiting magnitude for stars of various subsystems.

Many authors, including Kholopov [8], believe that, as far as their structure, dynamics, and evolution is concerned, globular and open clusters differ only in their mass (number of stars) and age; i.e., there is a universality in their structure and, probably, in their formation. The observed differences are mainly due to their different ages and total masses. Following this idea, we suggest that the systematic changes in the globular-cluster structures we have analyzed should also appear in open clusters. This possibility is supported by our earlier work [7]. It follows that the observed effect appears to express some general relationship in the structures of both globular and open clusters, and a more complete analysis is of considerable interest.

In accordance with our research program, we analyze here the spatial structure of the old open cluster NGC 2420 in detail. We consider various subsystems of the cluster that include stars located above, near, and below the main-sequence turnoff. We compare the structure of this cluster with those of some other clusters we have studied. The Galactic position of NGC 2420 ($l = 198°$, $b = +20°$), its (V, $B-V$) diagram (Fig. 1b), and the structural parameters listed in [9] make this cluster a typical old, open stellar aggregate intermediate between young open clusters and old globular clusters of the Galaxy.

2. FORMULATION OF THE PROBLEM

We constructed the stellar-density distributions for different subsystems of the cluster by applying a star-count technique to the data of Paparó [9]. This catalog gives the rectangular coordinates and B and V magnitudes of 1890 cluster and field stars located within a ring centered on NGC 2420, which has projected inner and outer radii of $r_1 \approx 6'$ and $r_2 \approx 25'$, respectively.

We must bear in mind the following characteristic feature of open clusters: the total number of stars in NGC 2420 included in [9] is not so as large as the number of stars usually analyzed in globular clusters. Therefore, when applying Kholopov's [8, 10] star-count technique to construct the distributions of the projected stellar density $F(r)$ for a given subsystem (r is the distance from the cluster center), we come up against the problem of poor statistics. The number of stars N within each ring zone of a given series used for the star counts is small, and the fractional errors in the inferred projected densities (computed assuming a Poisson distribution of stars within each zone [8]) become important: $\Delta F/F = 1/\sqrt{N}$. This
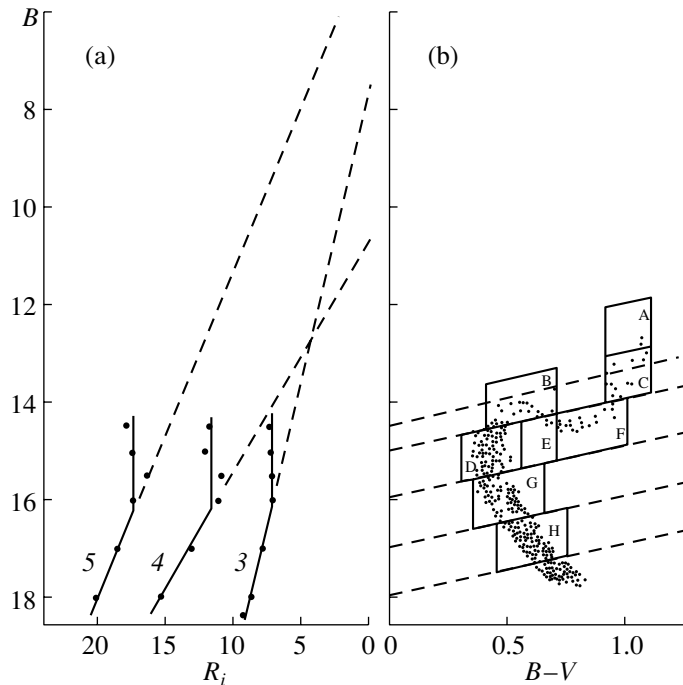
Fig. 1. (a) B vs. R_i and (b) V vs. $B-V$ diagrams for the open cluster NGC 2420, illustrating the systematic change in its structure.

makes conclusions about the behavior of the derived $F(r)$ curves uncertain. To avoid this, it is common to increase the width of the ring zones used, thereby increasing the number of stars within these zones and decreasing the fractional errors in the $F(r)$ curve. However, substantially increasing the zone widths smoothens real (and spurious) details in the distribution of the projected stellar density in the cluster, making them difficult to detect.

With these considerations in mind, we developed a refined version of Kholopov's technique for constructing $F(r)$, which we published in our earlier paper [11]. This version provides a successful compromise between the smoothness of $F(r)$ and statistical completeness, making it possible to identify large-scale features in the $F(r)$ curves with confidence. We also adopted an additional criterion: we consider features in the $F(r)$ curves to be real if they appear in different directions and at approximately the same distances from the center of the cluster.

3. DIFFERENTIAL AND INTEGRATED FUNCTIONS OF THE PROJECTED AND SPATIAL STELLAR DENSITY

We used the data from [9] and a refined version of Kholopov's technique [10, 11] (which assumes that the cluster is spherically symmetric) to construct the following distributions of the projected stellar density in the cluster as a function of the distance r from the center (defining the center to have the mean coordinates of all the stars):

$\Delta F(r, \varphi, \Delta B)$—differential curves for eight 90° radial cluster sectors projected onto the plane of the sky at azimuth intervals φ of 45° (i.e., in eight different directions from the cluster center) and including stars in the magnitude intervals $\Delta B < 15^m$, $15 < \Delta B < 16^m$, $16 < \Delta B < 17^m$, and $17 < \Delta B < 18^m$;

$\Delta F(r, \Delta B)$—differential curves averaged over all directions from the cluster center for the same B magnitude intervals;

$F(r, B)$—integrated curves averaged over all directions from the cluster center and including stars to limiting magnitudes of $B = 14.4, 15, 16, 17, 18$, and $18^m.4$.

$\Delta F_{gr}(r)$—differential curves averaged over all directions and including stars from groups A + C + F + E + B, D, G, and H located near the principal sequences of stars in the $(V, B-V)$ diagram for the cluster.

All ΔB intervals, limiting B magnitudes, and groups are shown on the $(V, B-V)$ diagram in Fig. 1b, which we have adopted from [9]. We use B rather than V magnitudes to facilitate future comparisons of the results reported here with those of our earlier analyses for other globular clusters. We obtained all curves using four series of overlapping ring zones with different widths $\Delta = 0.4, 1.0, 1.5, 2.0$ mm shifted with respect to each other by
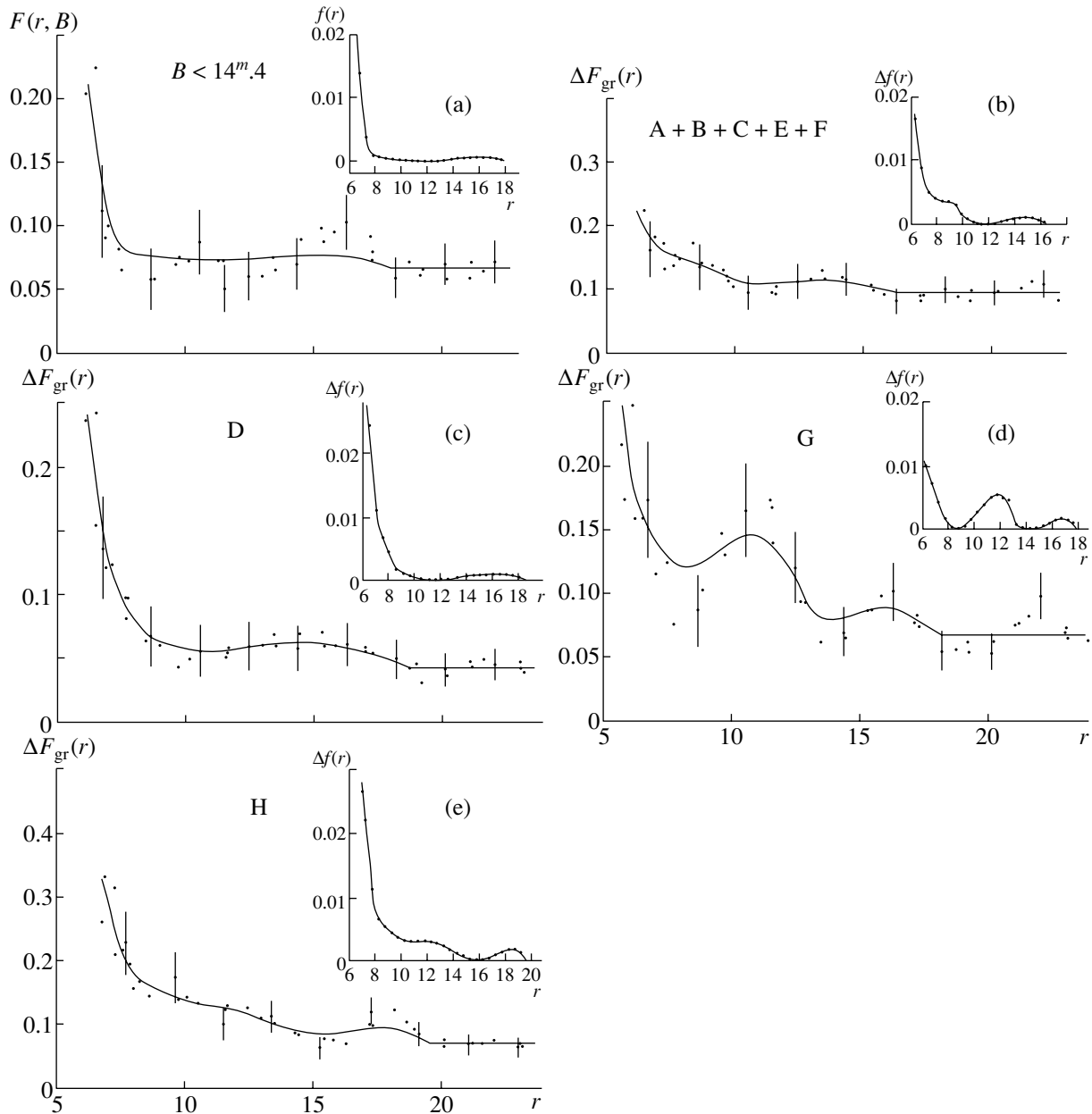
Fig. 2. Differential and integrated curves of the projected and spatial stellar density in NGC 2420 for various limiting B magnitudes and groups of stars (indicated on the plots). See text for the units.

$\Delta\Delta = 0.2, 0.5, 0.75, 1.0$ mm, taking into account the error in the interval [8]. We smoothed the curves using the technique described in [11]. Figure 2 illustrates some of the $F(r, B)$ and $\Delta F_{gr}(r)$ curves plotted in terms of the number of stars per square arcminute as a function of r (in arcmin). The vertical bars show the standard errors computed assuming that the distribution of stars within each zone is Poisson [8]. None of the curves reaches the cluster center, since this region is not included in [9]; i.e., we can analyze only the intermediate and outer regions of NGC 2420.

Our $\Delta F_{gr}(r)$ curves bear only a general resem-

blance to those reported by Paparó [9], since the curves in [9] are highly smoothed and (as pointed out above) have lost most of their details.

When computing the differential and integrated stellar-density distributions $\Delta f(r, \Delta B)$, $f(r, B)$ and $\Delta f_{gr}(r)$, we took the cluster radius R_c for each curve $\Delta F(r, \Delta B)$, $F(r, B)$, and $\Delta F_{gr}(r)$ to be the distance where the curve crossed the mean projected density of field stars ΔF_ϕ, F_ϕ, and $\Delta F_{gr\phi}$ derived from star counts made around the cluster. These radii are listed in the last column of Table 1 (in arcmin) as parameters the $R_5 = R_c$.

Table 1. Radii of spatial regions

$B, \Delta B$, group	R_3	R_4	R_5
14^m4	$7.5'$	$12.0'$	$18.0'$
15^m0	7.41 ± 0.38	12.29 ± 0.99	17.61 ± 1.45
A + B + C + E + F (15.5)	7.3	11.0	16.5
15.0−16.0 (D)	7.32 ± 0.57	11.31 ± 0.64	17.37 ± 1.12
16.0−17.0 (G)	7.99 ± 0.40	13.23 ± 0.90	18.63 ± 0.85
17.0−18.0 (H)	8.68 ± 0.66	15.35 ± 0.64	20.24 ± 0.90
18^m4	9.44 ± 0.49	−	−

We computed $\Delta f(r, \Delta B)$, $f(r, B)$, and $\Delta f_{\mathrm{gr}}(r)$ from the corresponding $\Delta F(r, \Delta B)$, $F(r, B)$, and $\Delta F_{\mathrm{gr}}(r)$ using the refined version of Kholopov's numerical technique (see [8, 11]; $a = 1$, spherical symmetry), with two series of overlapping ring zones of width $\Delta = 0.25'$ and $0.5'$. Some of the $f(r, B)$ and $\Delta f_{\mathrm{gr}}(r)$ curves in Fig. 2 (number of stars per cubic arcminute) are inset in the corresponding F and ΔF_{gr} plots.

4. ANALYSIS OF THE STELLAR-DENSITY DISTRIBUTIONS

4.1. Spatial regions in the Cluster Structure.

All curves ΔF, F, ΔF_{gr}, Δf, f, and Δf_{gr} enable us to confidently identify three distinct spatial zones in the cluster, with the density gradient varying only slightly or remaining approximately constant throughout each zone and changing abruptly at the zone boundaries, often breaking the monotonic behavior of F and f (Fig. 2). Following are the zones according to Kholopov's [8] terminology, listed in order of increasing distance r from the cluster center.

Zone III—The outer core region of radius R_3, defined as the boundary between the cluster core and corona.

Zone IV—The inner corona of radius R_4.

Zone V—The outer corona of radius R_5, which we took to be the cluster radius, R_c.

The low stellar density and its fluctuations in the corona region sometimes make it difficult or even impossible to identify certain zones for a particular subsystem of stars in different directions from the cluster center.

The first two zones—the central core of radius R_1 (Zone I) and the inner core of radius R_2 (Zone II)—cannot be identified, due to the incompleteness of [9] in the central region of NGC 2420. In his previous paper [12], Paparó reports an R_2 value of about $3.3'$. Table 1 summarizes the mean radii R_i (where i is the zone number) and their standard deviations (both in arcmin) for different directions from the cluster center. Figure 3 compares some of the R_i values for each zone with the corresponding limiting B magnitude for stars of the given subsystem. R_i are also in arcmin.

4.2. The Layered Structure of NGC 2420

Another interesting fact that we established by analyzing the ΔF, F, ΔF_{gr}, Δf, f, and Δf_{gr} curves is that the density in the inner regions of most of the zones is higher than the mean gradient for the corresponding region, whereas the situation is reversed at the zone boundaries. This effect is manifest as a step and wave in the ΔF, F, ΔF_{gr}, Δf, f, and Δf_{gr} curves. In addition, these curves cease to be monotonic (Fig. 2), and exhibit local density minima at the zone boundaries and maxima inside the zones. It is clear that these extrema are not due to chance fluctuations, since they appear in the curves for all cluster subsystems and in different directions from the cluster center.

We used numerical values of $\Delta F(r, \varphi, \Delta B)$ to plot various contours of the differential stellar density for four cluster subsystems, shown in Fig. 4. The shaded regions correspond to the projected stellar densities (number of stars per square arcminute) within the bins shown at the lower right-hand corner of the corresponding plot. Also shown in Fig. 4 are the mean density $\Delta F_{\phi}(\varphi, \Delta B)$ of field stars in the given direction and the direction itself. A dot marks the center of each subsystem (the mean coordinates of its member stars). The $\Delta F(r, \varphi, \Delta B) = \mathrm{const}$ contours do not reach the cluster center for the reasons indicated above. The deviations of these contours from a spherical shape in the region of the corona can be attributed to chance fluctuations of the stellar density.

The nonmonotonic behavior of $\Delta F(r, \Delta B)$ and the local minima and maxima in the density distribution in Fig. 2 are conspicuous in Fig. 4. The

boundaries R_i of the spatial zones usually coincide with minima in the stellar-density distribution.

All this suggests that NGC 2420 has a layered structure (at least in the corona region), with individual layers corresponding to the spatial zones indicated above. Between adjacent layers, there is usually a region where the stellar density is very low (approaching zero). In addition, the width of each zone $\Delta R_i = R_i - R_{i-1}$ ($i = 4, 5$) is approximately constant for a given subsystem of the cluster.

The globular clusters analyzed in our previous papers [1−6] exhibit a similar, but slightly different, layered structure. Nonmonotonic behavior of the density-distribution curves has also been noted by other authors in some open and globular clusters (see, e.g., [8]). In our opinion, the difference between the layered structures of open and globular clusters is that the latter have no empty star-free regions between individual layers. Figure 5 illustrates these two types of layered structure (the left and right panels correspond to a globular and open cluster, respectively). Let us assume that the stellar density in a given spherical layer is constant. We obtained histograms (N is the number of stars in a given area) and the corresponding smoothed curves of the projected ($F(r)$) and spatial ($f(r)$) stellar-density distributions assuming that the cluster is spherically symmetric. It is clear that the main features of these curves are similar to those found for real globular clusters (Figs. 2, 4, see also figures in [1−6]). Needless to say, the real structure of clusters is much more complicated than the two limiting cases considered here.

4.3. Systematic Variation of the Structure of the Cluster with Increasing Limiting B Magnitude

We can see from Table 1 and Fig. 3 that, starting with $B \approx 14^m$ (the magnitude of the brightest cluster stars) and down to $B = B_{\lim} = 16^m.16 \pm 0^m.24$, the radii of the spatial zones remain approximately constant ($R_i(B) \approx$ const), whereas at $B > B_{\lim}$ they systematically increase. The maximum and minimum increments are observed for the outermost and innermost zones, respectively. The limiting magnitude $B_{\lim}$ at which R_i begins to change systematically corresponds to the main-sequence turnoff point on the (V, $B-V$) diagram for NGC 2420 (Fig. 1b). This result is similar to those obtained in our previous analyses for other clusters.

We approximated the systematic variation of $R_i(B)$ as a function of B at $B > B_{\lim}$ by the following linear least-squares fit:

$$R_i = a_i B - b_i = a_i(B - B_{0i}),$$
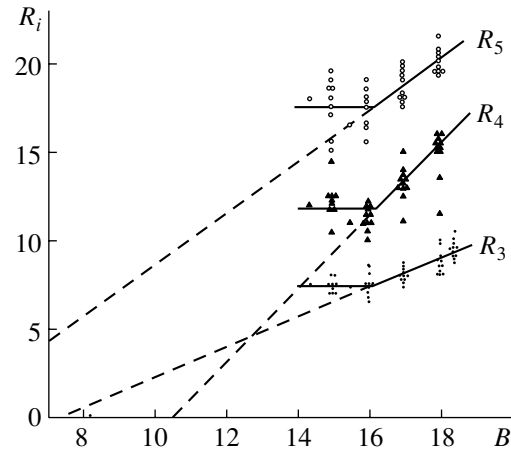$$B > B_{\lim}, \quad i = 3, 4, 5.$$

Fig. 3. Dependence of the radii of the zones of NGC 2420 on the limiting B magnitude.

Here, a_i is the slope of the relation and $B_{0i} = b_i/a_i$, the magnitude of zero radius R_i if the relation is extrapolated to $B < B_{\lim}$ (shown by the dashed lines in Fig. 3). Note that the magnitudes B_{0i} do not differ significantly from each other within the errors. The parameters a_i, b_i, B_{0i}, and $B_{\lim_i}$ for the ith radius are listed in Table 2.

Following the technique that we developed earlier, we computed the relative radii $\widetilde{r}_i = R_i(B)/R_4(B)$ of the spatial zones, listed in Table 2. The resulting $\widetilde{r}_i$ are approximately the same for all limiting B; i.e., $\widetilde{r}_i(B) \approx$ const. This indicates that, to first approximation, $R_i(B)$ increases homologously with B, as in the other clusters we have studied [1−7].

Together with the linear relation $R_i = a_i(B - B_{0i})$, the fact that all zones have the same relative radii implies that, for a homologous cluster, B_{0i} should be the same for all i ($B_{0i} = B_0$), as was pointed out above. We find this parameter by obtaining a least squares fit to the a_i and b_i from Table 2:

$$b_i = B_0 a_i, \quad B_0 = 8^m.1 \pm 2^m.8,$$

where B_0 is the same for all zones. Given the distance to the cluster $r = 2400$ pc [13] and its color excess $E_{B-V} = 0^m.02$ [14], we can determine the absolute magnitude corresponding to B_0: $M_{B_0} = -3^m.8 \pm 2^m.8$.

A comparison of the parameter a_i from Table 2 with the relative radii $\widetilde{r}_i$ leads to the following empirical least-squares relation:

$$a_i = A\widetilde{r}_i,$$

where $A =$ const is given in Table 2. Finally, we derived a unified relation for the size of the homologous spatial structure of the cluster:

$$R = A\widetilde{r}(B - B_0), \quad B > B_{\lim}.$$
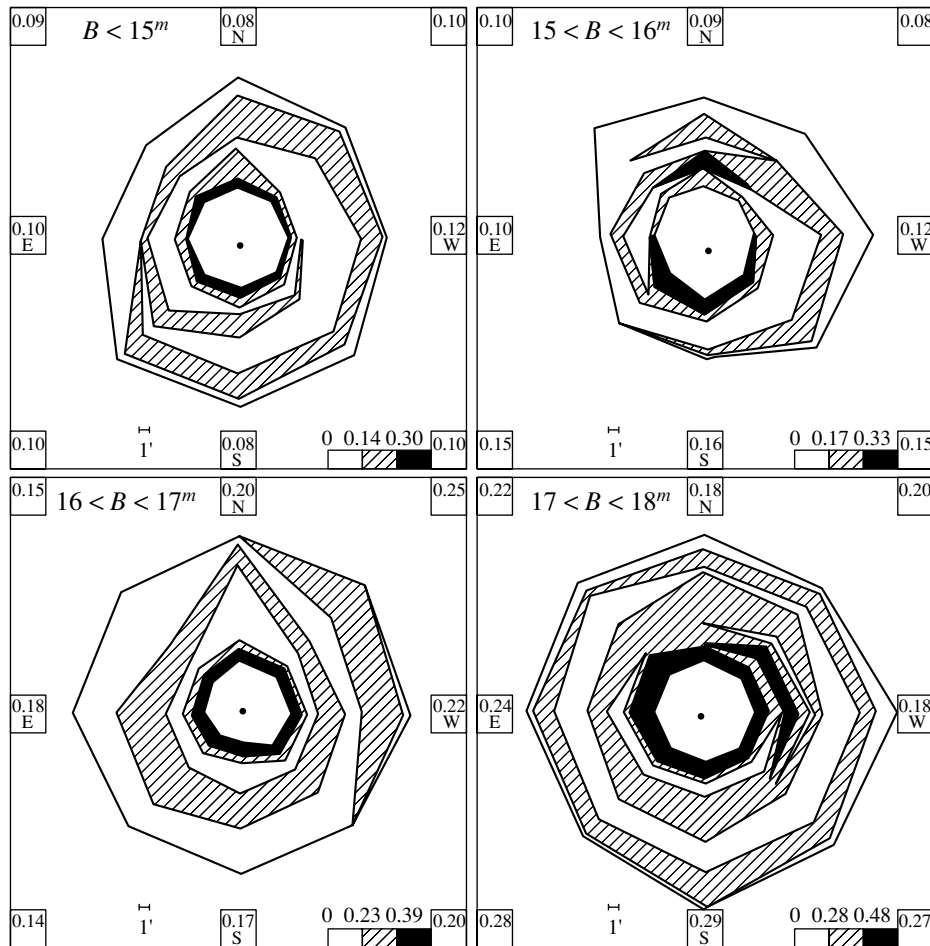
Fig. 4. Contours of projected stellar density for different subsystems of NGC 2420. Shown are the B-magnitude intervals, density of field stars, directions, and projected densities.

Figure 1a illustrates the main results concerning the systematic variation of the structure of NGC 2420. It is evident that, above the main-sequence turnoff point, the spatial structure remains virtually constant and varies systematically below this point: the radii of all zones increase in accordance with a single law. Unfortunately, we cannot analyze another manifestation of systematic variation of the cluster structure that we did in [1−6]—the variations $\Delta f_i(R_i(B), \Delta B)$ of the spatial density at the zone boundaries as a function of the B magnitude. The reason is that the corresponding density often becomes equal to zero (Fig. 2), due to the layered structure of the cluster.

4.4. Results and Discussion

(1) Paparó [9] gives the following mean masses m of stars of various groups ($m_\odot$ is the solar mass):

Group A + B + C + E + F: $m \approx 1.2m_\odot$,

Group D: $m \approx 1.2m_\odot$,

Group G: $m \approx 1.0m_\odot$,

Group H: $m \approx 0.8m_\odot$.

Figure 1a shows that the cluster structure begins to change systematically starting with group D (the main-sequence turnoff point) and that this variation continues toward groups G and H. It is logical to link the observed variation of the cluster structure with that of the mean mass of main-sequence stars for the different cluster subsystems at $B > B_{\lim}$, in accordance with the mass−luminosity relation. In other words, NGC 2420 exhibits structural mass segregation.

(2) The absence of any systematic structural variation at $B < B_{\lim}$ can be explained (as in the other clusters we have analyzed) by observational selection effects. According to stellar evolution theory, all stars located above the main-sequence turnoff point on the $(V, B-V)$ diagram (Fig. 1, groups A, B, C, F, and E) were earlier main-sequence stars near the turnoff point (group D) and have approximately the same mass. This is why these stars maintain their
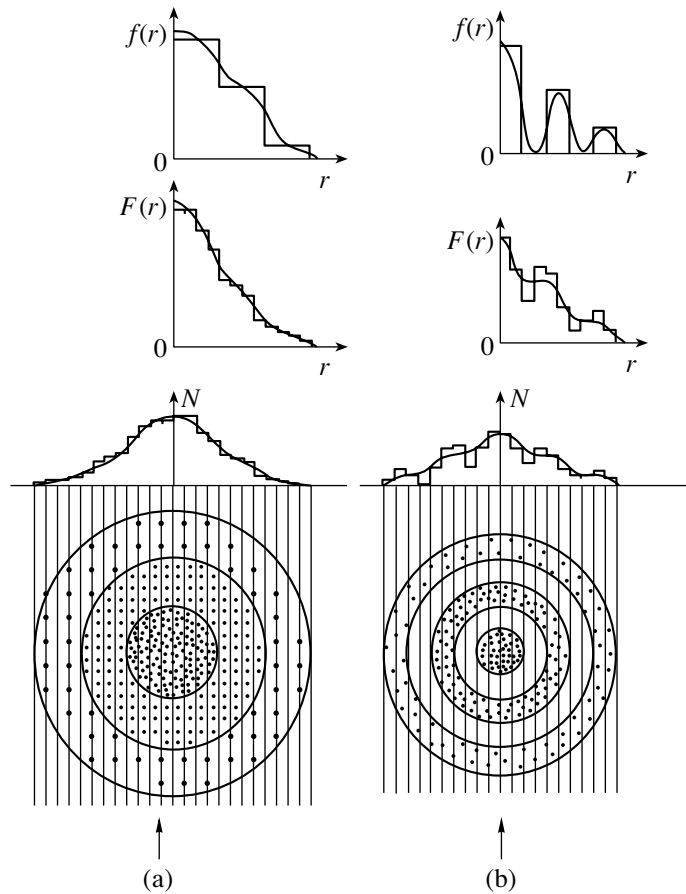
Fig. 5. Structural Models of (a) a globular and (b) an open cluster.

spatial distribution, which is similar to that of their progenitors. Therefore, no systematic variations of the cluster structure are observed at $B < B_{\text{lim}}$. Stars with higher masses, which were located on the zero-age main sequence well above the current turnoff point, have long ago evolved into white dwarfs and neutron stars, and are no longer observed in the cluster. In this connection, we assume that, from a physical point of view, the parameter B_0 (and, correspondingly, M_{B_0}, see above) is equal to the corresponding magnitude of the brightest cluster stars immediately after its formation.

(3) Here, as in other studies, we assume that the origins of the observed systematic variation of the cluster structure (structural mass segregation) should be sought in processes taking place during the formation of the cluster itself, not in its subsequent dynamic evolution driven by stellar encounters and dissipation. The following evidence supports this hypothesis.

(a) This effect is observed predominantly in the cluster corona and becomes stronger with increasing distance from the cluster center r. If it were a result of stellar encounters, the strongest variations would be observed closer to the cluster center, where the stellar density increases.

(b) The effect is observed in clusters with different ages [1−7], from the youngest open clusters to the oldest globular clusters.

We suggest that, after the formation of the cluster, its dynamical evolution tends to destroy the observed structural variation rather than create it.

(4) Using the perigalactic distance $R_{\text{p}} = 8.6$ kpc and mass $M_{\text{c}} = 300 m_{\odot}$ of the cluster, the mass of the Galaxy $M_{\text{g}} = 10^{11} m_{\odot}$, and King's formula $r_t = R_{\text{p}}(M_{\text{c}}/3.5 M_{\text{g}})^{1/3}$, Paparó [9] inferred the tidal radius of the cluster to be $r_t = 8.2$ pc $= 11.7'$ and suggested that the corona of NGC 2420 remains stable out to that distance, whereas stars dissipate due to the tidal field of the Galaxy beyond this radius.

It seems to us that Paparó [9] used overestimated M_{c} and underestimated M_{g} values and that even the outer corona of the cluster (at $r > 11.7'$) is stable against tidal forces.

It is possible that, when crossing the Galactic plane as it moves through the Galaxy, NGC 2420

Table 2. Structural parameters of NGC 2420

i	$\widetilde{r}_i$	a_i	b_i	B_{0i}	$B_{\text{п A}i}$
3	0.620 ± 0.047	0.826 ± 0.093	5.97 ± 1.62	$7^{m}\!.23$	$16^{m}\!.14 \pm 0.30$
4	1.0	2.022 ± 0.159	21.08 ± 2.71	10.42	16.22 ± 0.27
5	1.418 ± 0.112	1.446 ± 0.228	5.85 ± 3.90	4.05	16.13 ± 0.44
	$A = 1.350 \pm 0.444$		$B_0 = 8^{m}\!.16 \pm 2.88$		$B_{\text{lim}} = 16^{m}\!.16 \pm 0.24$

experiences strong tidal forces that tend to disrupt the homology and spherical shape of the cluster.

(5) Finally, we wish to point out that the results described here are not based on our own observational data, but on those of Paparó [9], ruling out errors on our part in the acquisition and reduction of observational data.

In conclusion, we note the following. The fact that similar phenomena are observed in other clusters suggests a common nature for the structure and formation of all clusters, both open and globular as was already pointed out by many authors.

REFERENCES

14. R. M. Rusev and Z. I. Peĭkov, Astron. Zh. **63**, 483 (1986) [Sov. Astron. **30**, 288 (1986)].
 2. Z. I. Peĭkov and R. M. Rusev, Astron. Zh. **65**, 41 (1988) [Sov. Astron. **32**, 21 (1988)].
 3. Z. I. Peĭkov and R. M. Rusev, Astron. Zh. **65**, 317 (1988) [Sov. Astron. **32**, 161 (1988)].
 4. Z. I. Peĭkov and R. M. Rusev, Astron. Zh. **67**, 694 (1990) [Sov. Astron. **34**, 349 (1990)].
 5. Z. I. Peĭkov and R. M. Rusev, Astron. Zh. **76**, 514 (1999) [Astron. Rep. **43**, 445 (1999)].
 6. Z. I. Peĭkov and R. M. Rusev, Astron. Zh. **76**, 571 (1999) [Astron. Rep. **43**, 494 (1999)].
 7. Z. I. Peĭkov, Astron. Zh. **67**, 1141 (1990) [Sov. Astron. **34**, 575 (1990)].
 8. P. N. Kholopov, *Star Clusters* (Nauka, Moscow, 1981).
 9. M. Paparó, Commun. Konkoly Obs. Hungarian Acad. of Sci., No. 81, 103 (1982).
10. P. N. Kholopov, Astron. Zh. **30**, 426 (1953).
11. Z. I. Peĭkov and R. M. Rusev, Astron. Zh. **68**, 78 (1991) [Sov. Astron. **35**, 39 (1991)].
12. M. Paparó, in *Stellar Physics and Evolution: The Role of Star Clusters in Cosmogony and in the Study of Galactic Structure*, Ed. by B. A. Bal àzs (Roland Eötvös Univ., Budapest, 1978), p. 47.
13. F. R. West, Astrophys. J., Suppl. Ser. **14**, 359 (1967); **14**, 384 (1967).
14. R. D. McClure, W. T. Forrester, and J. Gibson, Astrophys. J. **189**, 409 (1974).

Translated by A. Dambis

A Photometric and Spectroscopic Study
of the B[e]/X-ray Transient CI Cam

E. A. Barsukova[1], N. V. Borisov[1], V. P. Goranskiĭ[2], V. M. Lyutyĭ[2], and N. V. Metlova[2]

[1]*Special Astrophysical Observatory, Russian Academy of Sciences, Nizhni Arkhyz,*
Karachai-Cherkessian Republic, 369167 Russia
[2]*Sternberg Astronomical Institute, Universitetskiĭ pr. 13, Moscow, 119899 Russia*
Received July 17, 2001

Abstract—We compare $UBVR$ photometry of CI Cam obtained using facilities at the Sternberg Astronomical Institute in 1998–2001 and medium-resolution spectroscopy obtained at the Special Astrophysical Observatory in the same period. The photometric measurements and fluxes in the Balmer and some Fe II emission lines in the post-outburst quiescent spectrum of CI Cam display cyclic variations with a period of $1100\pm50^{\rm d}$. These variations could be due to orbital motion in a widely separated binary; one component, a giant, produces a reflection effect on the surface facing the other, compact component. Our V-band photometry confirms the $11^{\rm d}7$ period found by Miroshnichenko before the outburst but shows a lower amplitude (3%). We investigate the possibility that this photometric period is the same as the rotational period of the radio jets measured using the VLA. Based on modeling of the radio map, we estimate the inclination of the jet rotation axis to the line of sight, $i = 35°–40°$; the angle between the rotational axis and jet ejection direction, $\theta = 7°–10°$; and the jet spatial velocity, $0.23–0.26\,c$. The equivalent widths and fluxes of various spectral lines show different variation amplitudes during outburst and significantly different behavior during quiescence. We have detected five patterns of behavior, which provide evidence for stratification of the gas and dust envelope surrounding the system. The brightening of the [N II] forbidden line is delayed by $50–250^{\rm d}$ relative to the X-ray outburst maximum. © *2002 MAIK "Nauka/Interperiodica"*.

1. INTRODUCTION

CI Cam (MWC 84, KPD 0415+5552, MW 143, LS V +55°16, IRAS 04156+5552, XTE J0421+560; $4^{\rm h}19^{\rm m}42{\stackrel{\rm s}{.}}11, +55°59'57''{.}7$, 2000) is a well-known B[e] star ($V = 11^{\rm m}6$), X-ray system, and "microquasar." B[e] stars have the following characteristic spectral features [1]: (1) bright hydrogen and helium emission on a blue continuum; (2) numerous bright lines of Fe II and other metals, mainly at low ionization states and with low excitation potentials; (3) forbidden emission lines of metals and other elements ([Fe II], [O I]) in the optical; and (4) strong infrared excesses due to radiation of a hot circumstellar dust. CI Cam displays these characteristics in its spectrum. Since 1932, it has been known as a B star with H_α, He I, and Fe II emission [2, 3]. The star's spectrum was studied in detail in [4, 5]. The results of optical and infrared broad-band photometry are presented in [6]. The star shows a considerable brightness variability, with amplitudes as high as $0^{\rm m}4$ in the V band, leading to its inclusion in the General Catalogue of Variable Stars. Its photometric period, $11^{\rm d}7$, was determined in [5, 7] using data from [6]; the periodic component has an amplitude of $0^{\rm m}3$ in V. The spectral energy distribution can be represented

as a sum of two spectra: B0V + G8II [7] or B0V + K0II [5]. Observations of the cool star's absorption lines were reported in [5]. Thus, CI Cam resembles a symbiotic star whose properties partially overlap with those of B[e] stars. The star's light undergoes appreciable absorption, up to $A_V = 3^{\rm m}$, a sizable fraction of it being circumstellar. The distance of CI Cam is 1 kpc [8].

A strong X-ray outburst occurred in April 1998; at its maximum (on April 1, $0^{\rm h}57^{\rm m}$ UT; JD 2450904.54), the star's brightness at 2–12 keV reached 2 Crabs. The increase in the X-ray flux toward the maximum took only several hours [9]. The subsequent drop in flux was also dramatic: during the first two days, the flux decreased on a time scale $\tau_e = 0^{\rm d}56$ (the time for a decrease by a factor of e). By the fourth day, the time scale for the flux decline was $\tau_e = 2^{\rm d}34$ (the decline had slowed appreciably). The X-ray spectrum was soft compared to those of X-ray novae and did not propagate to energies above 60 keV [10]. Emission in the K lines of Fe XXV–Fe XXVI at 6.4–6.9 keV, S XV–S XVI at 2.45–2.62 keV, and the L lines of Si XIII–Si XIV at 1.86–2.01 keV were observed in the spectrum [11].

Optical observations were obtained only after the X-ray maximum, due to the time required for identification of the object. The highest brightness recorded in the outburst was 7.1 in R [12]. The optical and infrared spectrum showed considerable brightening of emission lines [13, 14], with the appearance of strong He II 4686 Å emission [13]. The H and He emission had broad bases, corresponding to expansion rates for matter in the envelope of 1200 km/s [15]. The contribution of emission lines to the photometric measurements increased. A radio source was detected by April 1 and reached a maximum of 120 mJy at 1.4 GHz at 3.83 UT. Light curves for the radio, X-ray, optical, and infrared fluxes are published in [16]. A delay of the outburst maximum with increasing radio wavelength was noted. The rate of decrease in the optical brightness from April 3 to April 10, 1998, was $\tau_e = 3\overset{\text{d}}{.}4 \pm 0\overset{\text{d}}{.}4$.

The radio source has a synchrotron nature. On April 5, it was resolved into a central core and oppositely directed jets; after some time, the jets became S-shaped, like the radio jets of the object SS 433 [17]. The expansion rate of the jets was 26 milliarcseconds/day, or 0.15 c for a distance of 1 kpc [18]. The jet structure is symmetrical and follows spirals diverging on a conical surface. As a Galactic stellar object with jets, CI Cam becomes a member of the class of objects known as "microquasars."

The X-ray flux decreased to the limit of detectability $10 - 15^{\text{d}}$ after the outburst. Increased brightness in the optical was observed until the end of the observing season, JD 2450941 (37^{d}); at the beginning of the next observing season (JD 2451051), the optical brightness was already low and showed a brightening trend [16]. However, radio emission was still detectable over the entire following season JD 2451020−51300, showing a gradual decrease with time [16]. X-ray emission was detected from the object in quiescence in long-exposure BeppoSAX observations; at different epochs, the X-ray emission had a soft spectrum (JD 2451425) [19], hard spectrum (JD 2451445) [20], or was completely undetectable. These observations indicate variability by at least an order of magnitude. A spectroscopic study of CI Cam in December 1998 and January 1999 [19] showed no spectral changes during that time period and a general similarity to the pre-outburst spectrum [4].

The current paper presents the results of our photometric and spectroscopic monitoring of CI Cam in quiescence in 1998−2001 and a comparison of photometrically calibrated spectra taken during the 1998 outburst and in quiescence.

2. PHOTOMETRIC OBSERVATIONS

We commenced our photometric observations on the night of April 3−4, 1998, as soon as we received the announcement of the outburst. We used a SBIG ST-6 CCD camera mounted on the 60-cm Zeiss reflector of the Crimean Laboratory of the Sternberg Astronomical Institute (SAI). For the three subsequent years, N.V. Metlova systematically continued observations with the same telescope and a single-channel UBV photometer designed by V.M. Lyutyĭ. The comparison star, GSC 3723.54 ($V = 10\overset{\text{m}}{.}401$; $B - V = 0\overset{\text{m}}{.}759$; $U - B = 0\overset{\text{m}}{.}336$) and check star GSC 3723.104 ($V = 12\overset{\text{m}}{.}386$; $B - V = 0\overset{\text{m}}{.}617$; $U - B = 0\overset{\text{m}}{.}408$) were photometrically calibrated using the North Polar Sequence. During the 1998−1999 season, we carried out photoelectric BVR observations using the 70-cm reflector of the SAI in Moscow and a single-channel photometer designed by I.M. Volkov and S.Yu. Shugarov. We used a FEU-79 photomultiplier to obtain a response band close to the Johnson R_J band. The BVR magnitudes of the same comparison stars were referred to stars of the catalog [21]. The B and V values for the comparison stars coincided within several hundredths of a magnitude, whereas the R magnitudes were $9\overset{\text{m}}{.}884$ and $12\overset{\text{m}}{.}034$ for the comparison and check star, respectively. The typical uncertainty in a single measurement was $0\overset{\text{m}}{.}02 - 0\overset{\text{m}}{.}03$.

In January 2001, we obtained a series of BVR observations using an Elektron K585 (530×590 pixel) CCD array mounted on the 1-m Zeiss reflector of the Special Astrophysical Observatory (SAO). Our chosen comparison star was GSC 3723.104, which was situated within the CCD field. The preliminary data calibration (bias and dark current correction, flatfielding) was performed in the MIDAS package. The photometry was carried out using software written by V. P. Goranskiĭ for the Windows NT operating system, which implements a technique for the correction of aperture measurements. These data are in good agreement with the photoelectric photometry data, but have better accuracy—$0\overset{\text{m}}{.}005$ in V and R. On JD 2451928 and JD 2451929, we carried out monitoring in the B band over 27 and 28 min with exposure times of 40^{s}. The dispersions of these observations were $0\overset{\text{m}}{.}008$ and $0\overset{\text{m}}{.}007$ for the two nights, respectively, confirming the complete absence of rapid variability on time scales of minutes or tens of minutes, as well as an absence of the flickering characteristic of symbiotic variables.

We also included published data for the $UBVR$ bands [16, 19, 22, 23] in our analysis. We determined the systematic offsets of individual sets of UBV observations from observations that were made simultaneously or close in time and used them to reduce all the data to the most uniform Crimean data set,

Table 1. Photometric observations of CI Cam

JD hel. 24...	V	B	U	R	Detector	Telescope	Observers
50907.2757	9.53	10.67	−	7.89	CCD	60	L, G
50908.2659	10.095	10.967	10.607	−	pe	60	L, G, M
50909.2812	10.21	11.38	−	8.66	CCD	60	L, G
50910.2565	10.38	11.33	−	8.84	CCD	60	L, G
50911.2581	10.60	11.57	−	9.11	CCD	60	L, G
50912.2555	10.73	11.68	−	9.25	CCD	60	L, G
50917.2980	11.21	−	−	9.86	CCD	60	L
50918.3140	11.30	−	−	9.93	CCD	60	L
50920.2840	11.344	12.141	11.741	−	pe	60	M
50922.2995	11.385	12.172	11.783	−	pe	60	M
50927.2826	11.438	12.213	11.808	−	pe	60	M
50929.2743	11.488	12.264	11.908	−	pe	60	M
50933.2732	11.504	12.265	11.897	−	pe	60	M
50934.3195	−	−	11.921	−	pe	60	M
50941.2947	11.59	12.29	12.05	−	pe	60	M
50942.2832	11.53	12.38	12.16	−	pe	60	M
51103.4740	11.648	12.418	12.051	−	pe	60	M
51104.5430	11.720	12.461	12.117	−	pe	60	M
51105.4780	11.690	12.450	12.051	−	pe	60	M
51105.4850	11.673	12.461	12.077	−	pe	60	M
51105.4920	11.683	12.458	12.071	−	pe	60	M
51110.5100	11.659	12.414	12.050	−	pe	60	M
51111.5070	11.607	12.369	12.036	−	pe	60	M
51112.3910	11.675	12.422	12.086	−	pe	60	M
51133.2798	11.606	12.410	12.086	−	pe	60	Sh
51133.2960	11.630	12.398	12.062	−	pe	60	Sh
51133.3062	11.589	12.408	12.038	−	pe	60	Sh
51137.4366	11.644	12.417	12.035	−	pe	60	M
51141.3537	11.655	12.416	12.066	−	pe	60	M
51143.3548	11.626	12.398	−	10.407	pe	70	G
51143.3705	11.644	12.434	−	10.424	pe	70	G
51143.3857	11.658	12.468	−	10.443	pe	70	G
51143.3548	11.626	12.398	−	10.407	pe	70	G
51143.3705	11.644	12.434	−	10.424	pe	70	G
51143.3857	11.658	12.468	−	10.443	pe	70	G
51148.3629	11.607	12.398	−	10.398	pe	70	G
51148.3791	11.617	12.417	−	10.440	pe	70	G

Table 1. (Contd.)

JD hel. 24...	V	B	U	R	Detector	Telescope	Observers
51152.3388	11.681	12.457	12.079	—	pe	60	M
51161.3109	11.681	12.435	12.110	—	pe	60	M
51163.5998	11.660	12.435	12.040	—	pe	60	M
51164.4602	11.652	12.399	12.062	—	pe	60	M
51176.2600	11.677	12.436	12.103	—	pe	60	M
51179.3464	11.633	12.460	—	10.380	pe	70	G
51179.3608	11.643	12.470	—	10.370	pe	70	G
51180.2383	11.666	12.379	12.072	—	pe	60	M
51197.3893	11.649	12.413	12.055	—	pe	60	M
51197.4001	11.636	12.437	12.131	—	pe	60	M
51199.2277	11.686	12.472	12.116	—	pe	60	M
51199.2378	11.667	12.424	12.061	—	pe	60	M
51213.2166	11.623	12.390	—	—	pe	70	G
51213.2207	11.643	12.410	—	10.360	pe	70	G
51213.2389	11.613	12.410	—	10.370	pe	70	G
51213.2490	11.583	12.420	—	10.340	pe	70	G
51218.2389	11.570	12.459	—	10.362	pe	70	G, K
51218.2464	11.609	12.464	—	10.389	pe	70	G, K
51218.2540	11.631	12.428	—	10.348	pe	70	G, K
51218.2612	11.596	12.463	—	10.354	pe	70	G, K
51223.2283	11.663	12.470	—	10.330	pe	70	G, K
51223.2329	11.663	12.470	—	10.330	pe	70	G, K
51223.2425	11.623	12.410	—	10.340	pe	70	G, K
51223.2529	11.633	12.490	—	10.370	pe	70	G, K
51223.2630	11.613	12.420	—	10.340	pe	70	G, K
51227.2442	11.662	12.431	12.053	—	pe	60	M
51232.2840	11.585	12.404	—	10.365	pe	70	G
51232.2974	11.633	12.465	—	10.373	pe	70	G
51232.3059	11.622	12.441	—	10.358	pe	70	G
51235.3438	11.668	12.433	12.091	—	pe	60	M
51235.3636	11.583	12.464	—	10.347	pe	70	G
51235.3771	11.681	12.517	—	10.369	pe	70	G
51264.3012	11.579	12.413	12.037	—	pe	60	M
51265.2567	11.669	12.426	12.077	—	pe	60	M
51287.2855	11.610	12.420	12.117	—	pe	60	M
51420.5427	11.640	12.400	12.095	—	pe	60	M
51440.5108	11.643	12.433	12.051	—	pe	60	M

Table 1. (Contd.)

JD hel. 24...	V	B	U	R	Detector	Telescope	Observers
51485.5330	11.647	12.429	12.061	−	pe	60	M
51485.5639	11.638	12.421	12.049	−	pe	60	M
51485.5708	11.649	12.429	12.079	−	pe	60	M
51485.5771	11.648	12.438	12.066	−	pe	60	M
51485.5837	11.634	12.418	12.029	−	pe	60	M
51485.5910	11.635	12.406	12.067	−	pe	60	M
51485.5972	11.615	12.417	12.101	−	pe	60	M
51485.6048	11.634	12.447	12.045	−	pe	60	M
51485.6111	11.633	12.400	12.050	−	pe	60	M
51485.6180	11.610	12.417	12.071	−	pe	60	M
51485.6246	11.634	12.416	12.046	−	pe	60	M
51485.6319	11.647	12.441	12.063	−	pe	60	M
51492.4350	11.698	12.466	12.107	−	pe	60	M
51492.4461	11.678	12.449	12.102	−	pe	60	M
51492.4572	11.696	12.463	12.132	−	pe	60	M
51493.5305	11.651	12.418	12.072	−	pe	60	M
51493.5371	11.666	12.429	12.039	−	pe	60	M
51493.6246	11.674	12.434	12.095	−	pe	60	M
51493.6322	11.670	12.449	12.107	−	pe	60	M
51499.5344	11.679	12.458	12.085	−	pe	60	M
51499.5414	11.719	12.485	12.114	−	pe	60	M
51502.5240	11.657	12.449	12.102	−	pe	60	M
51502.5313	11.674	12.460	12.097	−	pe	60	M
51502.5386	11.671	12.461	12.102	−	pe	60	M
51514.5609	11.707	12.472	12.132	−	pe	60	M
51514.5679	11.687	12.458	12.150	−	pe	60	M
51525.5179	11.691	12.440	12.040	−	pe	60	M
51525.5249	11.649	12.436	12.084	−	pe	60	M
51525.5315	11.642	12.471	12.097	−	pe	60	M
51526.4565	11.702	12.475	12.144	−	pe	60	M
51526.4631	11.685	12.465	12.118	−	pe	60	M
51645.2979	11.743	12.499	12.185	−	pe	60	M
51645.3048	11.706	12.531	12.295	−	pe	60	M
51822.6055	11.794	12.563	12.200	−	pe	60	M
51831.4368	11.660	12.521	12.301	−	pe	60	M
51836.4257	11.746	12.523	12.220	−	pe	60	M
51842.6180	11.776	12.585	12.370	−	pe	60	M

Table 1. (Contd.)

JD hel. 24...	V	B	U	R	Detector	Telescope	Observers
51842.6246	11.808	12.647	12.506	—	pe	60	M
51882.5555	11.755	12.554	12.244	—	pe	60	M
51882.5625	11.787	12.557	12.256	—	pe	60	M
51882.5694	11.766	12.544	12.170	—	pe	60	M
51882.5760	11.765	12.565	12.207	—	pe	60	M
51882.5829	11.771	12.568	12.197	—	pe	60	M
51882.5895	11.769	12.518	12.191	—	pe	60	M
51882.5965	11.744	12.526	12.177	—	pe	60	M
51925.4042	11.721	12.501	12.157	—	pe	60	M
51925.4118	11.725	12.521	12.180	—	pe	60	M
51926.5173	11.764	12.538	12.196	—	pe	60	M
51926.5260	11.754	12.534	12.268	—	pe	60	M
51927.2860	11.760	12.534	12.188	—	pe	60	M
51927.2920	11.782	12.526	12.166	—	pe	60	M
51928.2664	11.749	12.557	—	10.566	CCD	100	B, G
51928.2674	11.749	12.557	—	10.566	CCD	100	B, G
51929.3068	11.751	12.537	—	10.579	CCD	100	B, G
51930.2810	11.742	12.557	—	10.582	CCD	100	B, G
51932.3709	11.762	12.530	12.187	—	pe	60	M
51932.3782	11.748	12.530	12.222	—	pe	60	M
51932.3851	11.753	12.530	12.187	—	pe	60	M
51932.3914	11.754	12.522	12.191	—	pe	60	M
51932.3987	11.748	12.526	12.178	—	pe	60	M
51932.4053	11.757	12.532	12.212	—	pe	60	M
51932.4126	11.742	12.508	12.214	—	pe	60	M
51932.4195	11.737	12.520	12.200	—	pe	60	M
51932.4264	11.701	12.519	12.187	—	pe	60	M
51934.5163	11.785	12.561	12.230	—	pe	60	M
51935.2836	11.757	12.559	12.213	—	pe	60	M
51935.2898	11.726	12.449	12.126	—	pe	60	M

Notes: Observers: B—E.A. Barsukova, L—V.M. Lyutyĭ, G—V.P. Goranskiĭ, M— N.V. Metlova, K—E.A. Karitskaya (Institute of Astronomy of the Russian Academy of Sciences), Sh—S.Yu. Shugarov (Sternberg Astronomical Institute).

Telescopes: 60—60-cm Zeiss reflector of the SAI Crimean Laboratory; 70—70-cm reflector of the SAI in Moscow; 100—1-m Zeiss reflector of the SAO.

Detectors: CCD—SBIG ST-6 and Elektron K585 cameras (see text), pe—single-channel photoelectric UBV and BVR photometers (see text).

obtained by N.V. Metlova. The results of our observations are collected in Table 1, and light curves for the quiescent state are shown in Fig. 1.

We can see in Fig. 1 a sinusoidal cycle of brightness variations in all bands, with amplitudes of 0^m2U, 0^m15B, and 0^m12V. There is a broad maximum around JD 2451270 and a narrower minimum around JD 2451820. The length of the cycle is $1100^d \pm 50^d$. The dispersion of the V light curve is very low—only 0^m029. The behavior of the star after the outburst differs greatly from that observed before the outburst [6], though the mean brightness level in quiescence did not change. Our data show a clear correlation between the brightness variations in all bands. The correlation coefficient between B and V is 0.84, and that between U and B is 0.82. The corresponding correlation coefficients for the observations published in [6] are only 0.58 and 0.37. The observations of [6] may have lower accuracy. The cyclic behavior of the star after its outburst resembles the periodic variations observed in some symbiotic stars, associated with the reflection effect. In such cases, the period for the variability usually coincides with the orbital period.

To test for the 11^d7 period found by Miroshnichenko [5] in the observations from [6] in our own photometric data, we first subtracted a mean smoothed curve of the 1100^d cycle from the UBV light curves. Such "prewhitening" is widely used in frequency analysis. Further, the residuals were subjected to a frequency analysis using the method of Deeming [24]. Our observations confirm the presence of Miroshnichenko's period only for the V-band data. The dispersion of the residuals in this band is 0^m029. The amplitude spectrum of the harmonic component is shown in Fig. 2. The confidence levels for the peaks in the spectrum were derived from an analysis of the distribution function for the amplitudes of a random series, obtained from the initial series of residuals by randomly shuffling the magnitudes. The amplitude of the peak corresponding to the 11-day period is only 0^m015. The light curve is shown in Fig. 3. The confidence level of this period is very high and exceeds 99.999%, though the amplitude of the light curve, 0^m03, is at least a factor of five lower than that found in [5]. The dispersion of our light curve is 0^m024, so the contribution of the periodic component to the residuals is only $\approx 20\%$. The phases of the light curve in Fig. 3 were computed using the formula

$$\text{Max} = 2451075.56 + 11^d719 \times E. \qquad (1)$$

The uncertainty in the period is $\pm 0^d02$. The good agreement with the value found by Miroshnichenko using independent observations leaves no doubt that
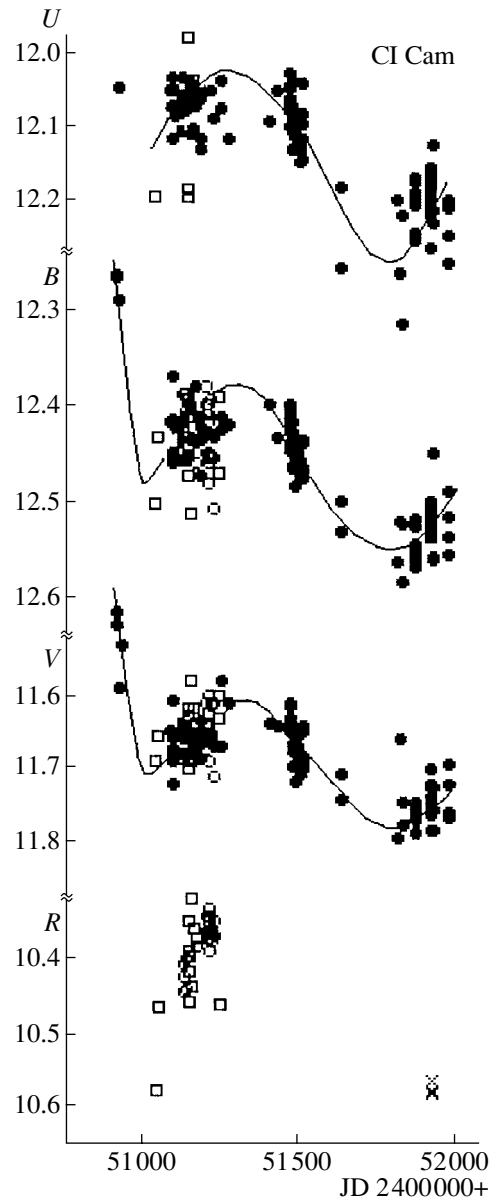
**Fig. 1.** $UBVR$ light curves of CI Cam after the 1998 outburst.

this period is real, despite the fact that no corresponding significant peaks were found in the frequency spectra for the B and U bands. We suggest that this is due to the better accuracy of the V observations. Based on the photometry of [6], we derive the following formula, valid prior to the outburst:

$$\text{Max} = 2448995.64 + 11^d704 \times E. \qquad (2)$$

Here, the period is in the range $11^d69 - 11^d72$. At that time, the amplitudes of the periodic component were 0^m16 B, 0^m13 V, and 0^m10 R. The shape of the light curve in B and R is close to sinusoidal. The V-band light curve has two peaks (cf. Fig. 4 in [5]). The phases computed using (1) and (2) do not agree;
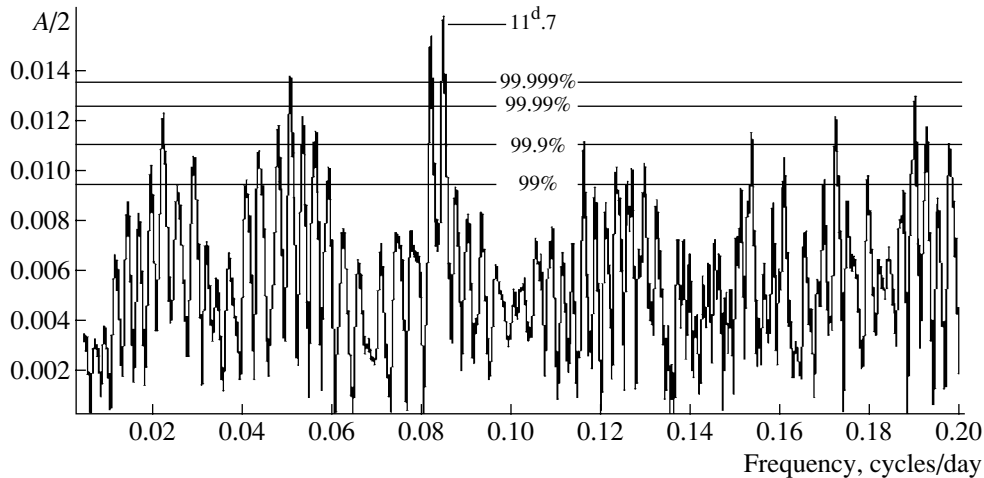
Fig. 2. Amplitude–frequency relation (the amplitude spectrum, after Deeming) for the residuals of the mean light curve with the 1100-day period in the *V* band. The horizontal lines show the indicated confidence levels.
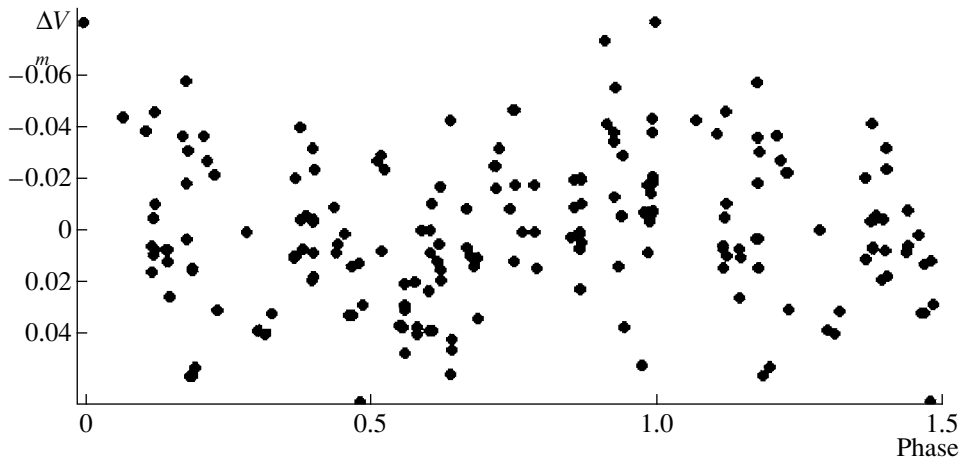
Fig. 3. *V*-band light curve for the residuals folded with the period $11^{d}72$.

the light curves before and after the outburst are best fit by two different periods—$11^{d}69$ and $11^{d}75$. Note that the period $11^{d}7$ was not confirmed in [25] based on CCD photometry acquired in the 1999 observing season.

We investigated the possibility of a connection between the 11-day photometric period and the radio jet rotational period. A $0.6'' \times 0.6''$ VLA radio map for CI Cam is published in [17]; the epoch of the map is not indicated. Two oppositely directed S-shaped jets are apparent, each extending up to $0''3$ from the central source. The structure appears to correspond to one wrap of a spiral diverging on the surface of a cone. If we adopt the jet-propagation rate of [18], $0''026$/day, the resulting time for one turn will be $11^{d}5 \pm 1^{d}0$, very close to the period found by Miroshnichenko. If the periods in the optical and radio are

indeed related, the 11-day period can be interpreted as the rotational period of a star whose dipole magnetic field is inclined to its rotational axis, with the jets ejected along the magnetic-dipole axis.

To test this hypothesis, we computed a rotating-jet model using code written for computations of the shape of the jet of SS 433. We estimated four parameters describing the shape of the radio jet of CI Cam [17]: the inclination of the star's rotational axis to the line of sight i, the angle between the rotational axis and the jet ejection direction θ, the rotational phase when the jet began to be ejected ψ, and the epoch when the radio map was obtained. The parameter ψ is an analog of the precessional phase for the jet of SS 433. It is measured from the time when the angle between the jet and the line of sight was minimum. In the hypothesis being tested, this is the time when the

brightness of the rotating star should be greatest. The adopted rotational period was $11\overset{d}{.}7$.

Our modeling yielded narrow intervals for the angles, $i = 35° - 40°$ and $\theta = 7° - 10°$. The spatial velocity of the jet of CI Cam for these angles and the observed value of $0.15\,c$ projected onto the plane of the sky [18] is $0.23 - 0.26\,c$. We assume that the ejection of the jets began on March 1998, 31.6 UT (JD 2450904.1), with the beginning of the X-ray outburst [9]. The rotational phase ψ at the beginning of the outburst depends on how far the jet had rotated at the epoch of the radio map, and thus on this epoch. Our model already reproduces the radio map well at 78% of the jet rotation period, corresponding to an earliest epoch of April 9.4 UT, 1998, and $\psi = 0.69$. One complete rotation corresponds to April 12.6 UT, 1998, and $\psi = 0.74$. The angle i is determined to within its sign, and, due to the ambiguity in the jet direction relative to the observer, the phase ψ can also have values in the range $\psi = 0.19 - 0.24$. The phases at the beginning of the X-ray outburst are 0.37 and 0.06 according to (1) and (2) and do not fall into the computed ranges for ψ.

The main conclusion of our modeling is that the radio map [18] can be reproduced by a model with jets rotating with the period $11\overset{d}{.}7$ for a specific set of parameters. Moreover, the modeling is potentially able to relate the appearance of the jet to the phase of the light curve for the 11-day period. This will become possible after the publication of VLA radio maps with the corresponding epochs indicated and sufficient improvement in the 11-day period.

3. SPECTROSCOPIC OBSERVATIONS

Our spectroscopic observations of CI Cam began on the night of April 4/5, 1998, during the outburst, on the 6-m telescope of the SAO, using a SP-124 spectrograph. Our subsequent observations were primarily obtained on the 1-m Zeiss reflector of the SAO with a UAGS spectrograph, and continued until January 27, 2001. Spectra were obtained using various CCDs. The preliminary reduction of the spectra in the MIDAS package applied corrections for the bias and dark current. The spectra obtained on individual nights were summed. These were wavelength-calibrated using the spectrum of a neon-argon lamp. The sky background was recorded through the same slit on both sides of a spectrum; it was then summed for CCD frame rows and subtracted. The series of spectra taken on December 6, 2000 used a diaphragm instead of a slit, and the sky background was not recorded separately. These spectra were used solely for radial-velocity determinations. Finally, all the spectra were normalized to a continuum level

of unity. All spectral reduction was performed by E.A. Barsukova. A complete observation log for the spectra, with the dates of observations, spectral ranges, resolutions, numbers of spectra per night, lists of telescopes used, and observers, is presented in Table 2.

The results of our spectroscopic observations during the outburst have already been partially published in [13, 15].

Figures 4a and 4b show a typical quiescent spectrum. It repeats in detail the pre-outburst spectrum by Downes [4] and the spectrum immediately after the outburst by Orlandini *et al.* [19]. Line identifications are indicated in the figure. We used the spectroscopic data and laboratory wavelengths of emission lines from [26−29]. The spectrum displays bright hydrogen and neutral helium emission, numerous permitted iron lines, a weak silicon line at $\lambda6347$ Å, and a forbidden nitrogen line. Our identification of the $\lambda5755$ Å emission line with the forbidden nitrogen line [N II] is beyond doubt and differs from the identification with Fe II in [4] and [19]. The difference of this line's wavelength by 8 Å from the laboratory value noted in [19] is due to misidentification. We find no bright forbidden [Fe II] lines in our spectral range; in particular, we identify the emission at $\lambda \approx 4416$ Å with Fe II $\lambda4414.78$ Å and not [Fe II] as in [19]. Thus, due to the absence of [Fe II] lines in the optical spectrum of CI Cam, the star does not correspond to the standard definition of a B[e] star in this regard.

At first glance, it is difficult to discern any large differences between the quiescent and outburst spectra of CI Cam (see, for instance, [13, 15]). Essentially the same emission lines are observed, with only their relative brightnesses changing. The most obvious changes in the outburst spectrum are the following. Broad pedestals appeared in the Balmer and He I lines, testifying to the presence of matter moving at velocities up to 1200 km/s, although the narrow components visible in quiescence with widths of 200−400 km/s were still present. Bright He II $\lambda4686$ Å emission appeared; this emission is very weak but detectable in quiescence. Strong emission in the Na I D_1 and D_2 doublet also developed; in the outburst, it merged with the broad He I $\lambda5876$ Å line, resembling a hump in the He I profile. As the star's brightness faded and the width of the He I line decreased, the sodium emission became distinct from the He line and then disappeared. It has a complex profile in high-dispersion spectra, with both emission and absorption components, the latter evidently of interstellar origin. In contrast, the [N II] $\lambda5755$ Å forbidden line, which is almost invisible during the outburst, became one of the brightest lines after the outburst. Note that

Table 2. Spectroscopic observations

JD hel. 24...	Date	Range, Å	Resolution, Å	Number of spectra	Telescope	Observers
50908.259	Apr. 4, 1998	3800−6100	4	2	6	P, U
50908.260	Apr. 4, 1998	5000−7400	4	1	6	P, U
50909.176	Apr. 5, 1998	5000−7400	4	1	6	P, U
50909.20	Apr. 5, 1998	3800−6100	4	1	6	P, U
50910.20	Apr. 6, 1998	3800−6100	4	2	6	P, U
50910.205	Apr. 6, 1998	5000−7400	4	3	6	P, U
50923.25	Apr. 19, 1998	3800−6100	7	29	6	P, U, M
50923.266	Apr. 19, 1998	5000−7400	7	2	6	P, U, M
50950.30	May 16, 1998	3800−6100	4	2	6	V1, F
50950.314	May 16, 1998	5000−7400	4	2	6	V1, F
51204.333	Jan. 25, 1999	3800−6100	4	100	6	B1, V1, M, F
51206.30	Jan. 27, 1999	5000−7700	0.23	3	6	B1, M
51398.534	Jan. 8, 1999	5580−7320	4	2	1	B2
51399.538	Aug. 9, 1999	4100−5800	4	2	1	B2
51399.525	Aug. 9, 1999	5580−7290	4	2	1	B2
51400.510	Aug. 10, 1999	4100−5800	4	4	1	B2
51400.531	Aug. 10, 1999	5600−7300	4	4	1	B2
51423.551	Sept. 2, 1999	5590−7330	4	4	1	B2
51423.566	Sept. 2, 1999	4100−5780	4	3	1	B2
51424.551	Sept. 3, 1999	4100−5780	4	4	1	B1, B2
51425.581	Sept. 4, 1999	5600−7300	4	13	1	B1, B2
51426.519	Sept. 5, 1999	4100−5780	4	3	1	B1, B2
51426.561	Sept. 5, 1999	5600−7300	4	5	1	B1, B2
51464.523	Oct. 13, 1999	5600−7320	4	6	1	B3
51464.542	Oct. 13, 1999	4100−5780	4	4	1	B3
51465.434	Oct. 14, 1999	4100−5780	4	4	1	B3
51465.458	Oct. 14, 1999	5600−7320	4	6	1	B3
51485.653	Nov. 3, 1999	4100−5700	4	3	1	B2
51485.666	Nov. 3, 1999	5670−7340	4	4	1	B2
51488.416	Nov. 6, 1999	5670−7320	4	6	1	B2
51488.447	Nov. 6, 1999	4100−5780	4	6	1	B2
51514.288	Dec. 1, 1999	4100−5780	4	10	1	B2, B3
51635.187	Mar. 3, 2000	5660−7330	4	10	1	B2
51810.552	Sept. 23, 2000	5600−7280	4	5	1	V2
51812.555	Sept. 25, 2000	5600−7230	4	10	1	S
51844.500	Oct. 27, 2000	4100−5800	4	11	1	B2
51846.430	Oct. 29, 2000	5600−7240	4	5	1	V2
51848.416	Oct. 31, 2000	5600−7300	4	6	1	B2
51864.375	Nov. 16, 2000	5660−7320	4	9	1	B2
51864.448	Nov. 16, 2000	4100−5780	4	10	1	B2
51880.312	Dec. 1, 2000	5660−7330	4	17	1	B2
51885.319	Dec. 6, 2000	4500−7000	5	164*	6	V1, M, F
51936.243	Jan. 26, 2001	5660−7320	4	10	1	B2
51937.234	Jan. 27, 2001.01	5660−7320	4	4	1	V2

* Aperture spectra through cirrus clouds.

Notes: Observers: B1—E.A. Barsukova, V2—V.V. Vlasyuk, S—N.I. Serafimovich, B2—N.V. Borisov, M—D.N. Monin, U—A.V. Ugryumov, B3—A.N. Burenkov, P—S.A. Pustil'nik, F—S.N. Fabrika, V1—G.G. Valyavin (all observers are staff members of the Special Astrophysical Observatory).

Telescopes: 6—6-m reflector of the SAO, 1—1-m Zeiss reflector of the SAO.

Table 3. Outburst behavior of spectral lines

Line	λ_{lab}, Å	$\text{EW}_{\text{out}}/\text{EW}_{\text{q}}$	$\log(F_{\text{out}}/F_{\text{q}})$	$\log(P_{\text{i}} + P_{\text{e}})(EV)$	Type
H_γ	4340.468	4.86	0.96	1.12	H_α
Fe II	4414.78	2.97	0.80	1.13	H_α
He I	4471.688	12.28	1.43	1.36	He I
Fe II	4583.290	2.89	0.88	1.13	H_α
HFe II	4685.810	132.82	2.49	1.88	He II
H_β	4861.332	3.24	0.87	1.11	H_α
He I(+Fe II)	4921.929	3.79	1.51	1.36	He I
He I	5015.675	22.90	1.68	1.36	He I
Fe II	5197.569	3.49	0.92	1.12	H_α
Fe II	5234.620	5.52	1.09	1.13	H_α
Fe II	5316.609	2.90	0.87	1.13	H_α
Fe II	5534.860	2.70	0.83	1.13	H_α
[N II]	5754.640	0.32	-0.10	1.25	[N II]
He I	5875.792	8.70	1.35	1.36	He I
Fe II	6147.735	2.60	0.98	1.14	Si II
Fe II	6318.000	1.23	0.53	1.14	He I
Si II	6347.091	5.52	1.26	1.26	Si II
Fe II	6385.470	1.00	0.54	1.11	He I
Fe II	6456.376	1.71	0.88	1.14	H_α
Fe II	6491.670	0.94	0.82	1.13	Si II
Fe II	6516.053	1.88	0.77	1.10	H_α
H_α	6562.816	1.21	0.60	1.08	H_α
He I	6678.151	7.92	1.41	1.36	He I
He I	7065.440	4.60	1.23	1.36	He I

this line has almost the same brightness in the pre-outburst spectrum [4], where it was identified as Fe II.

The contribution of line emission to the broad B and V bands (of the $UBVR_J$ system) is ≈10% in quiescence and ≈40% during the outburst; in the R_J band, which includes the very bright H_α emission, these contributions are 38 and 58%, respectively.

(a) Line equivalent widths and fluxes

We measured the equivalent widths of the bright emission lines marked with filled squares in Figs. 4a and 4b and then translated them into fluxes in physical units (erg cm^{-2} s^{-1}) using photometric data. We mainly selected strong unblended lines for this analysis. In cases when lines turned out to be blends and could not be separated, we determined the combined equivalent widths of their components. In addition, we determined the ratios of the equivalent widths and line brightnesses during the outburst and in quiescence. Since there were no observations at the peak of the outburst, we took the mean values for the first two nights of observations, April 4 and 5, 1998, as values describing the outburst. We adopted averages
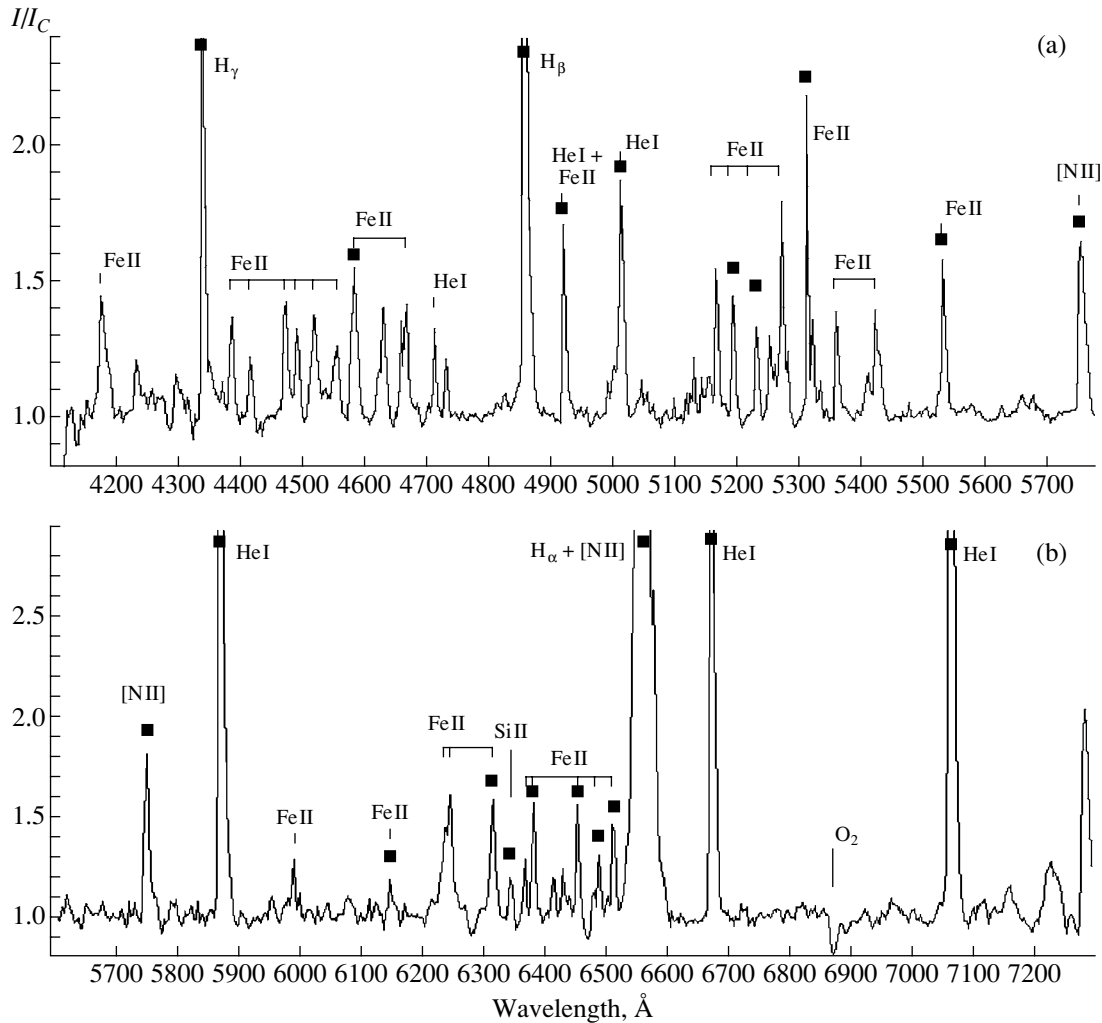
Fig. 4. Spectrum of CI Cam in quiescence in the (a) blue and (b) red. The filled squares mark emission lines selected for measurements.

for the next (1999) observing season for the quiescence values. The results of our measurements of the equivalent width ratios, logarithms of flux ratios, and logarithms of the combined excitation potential (ionization potential + excitation potential) for each line (from [27]) are collected in Table 3.

Figure 5 shows typical time dependences of the equivalent widths. The open circles denote observations by Orlandini *et al.* [19], and the filled circles are our observations. The equivalent widths in [19] agree very well with our own; this is not true for the line fluxes. The flux calculations were likely affected by considerable systematic differences in the photometric data. Typical time dependences for the line fluxes are displayed in Fig. 6. Parameter variations during the 1998 outburst are not shown in Figs. 5 and 6 to better display the post-outburst behavior in quiescence. Most of the plots show only the final decline stage of the outburst. The extent of the changes in

various lines during the outburst is apparent from the data in Table 3. Different lines show appreciably different behaviors. At least five types of behavior can be distinguished; the behavior displayed by each line is indicated in the last column of Table 3.

He II Type

A strong brightening of the emission, with the equivalent width changing by at least a factor of 133 and the flux by a factor of 300 compared to the quiescent state (not shown in the figure due to the difficulty in reproducing such behavior). The He II $\lambda4686$ Å line is probably formed in the immediate vicinity of the compact object.

Hα Type

An intensity increase in outburst by a factor of 5 to 10, with sinusoidal variations of the equivalent widths that precisely reproduce the cycle of the brightness variations (Fig. 5a). The line equivalent widths are correlated with the brightnesses in the $UBVR$ bands.
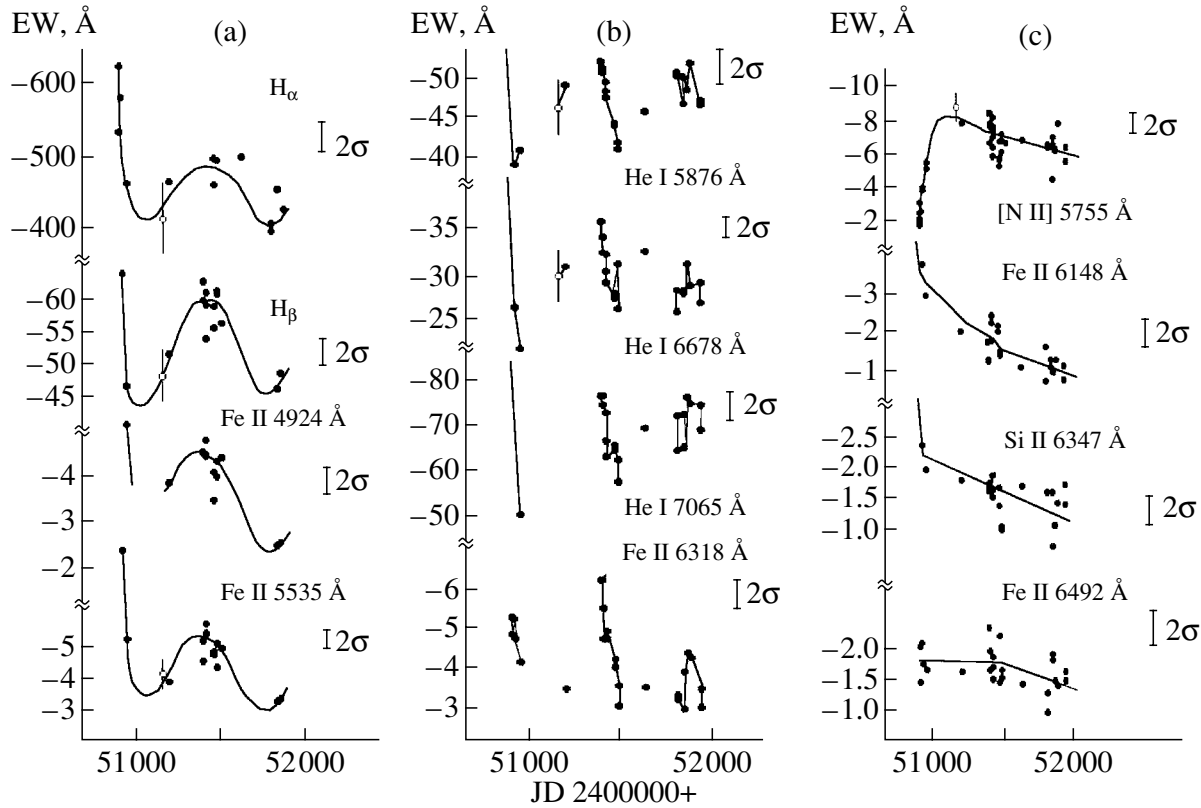
Fig. 5. Time dependence of emission-line equivalent widths. Various types of behavior are shown, characteristic of specific lines: (a) H_α, (b) He I (c, upper curve) [N II], (c, three bottom curves) Si II. The circles are observations from [19]. The vertical bars show the 2σ uncertainties in the equivalent widths.

This behavior is shown by the Balmer lines and most Fe II lines. The equivalent-width variations of these lines independently confirm the 1100-day photometric cycle. The translation of the equivalent widths into fluxes increases the relative amplitude of the cyclic variation from 25 to 43% (Fig. 6, H_β). The formation region for lines of this type of behavior probably lies on the portion of the surface of the normal star facing the compact component near the inner Lagrangian point L_1 and the line intensity varies with orbital phase.

He I Type

Increase in the line flux in outburst by a factor of 15 to 50, with strong, irregular variations of the equivalent width in quiescence (Fig. 5b). Along with all He I lines, this type includes the Fe II $\lambda6318$ and 6385 Å lines. No 1100-day cyclic variations are observed. During the 1999 season (JD 2451399–2451485), when the H_α-type lines exhibited a broad maximum in the time dependence of the equivalent widths, the He I-type lines showed a systematic decrease in their equivalent widths and brightnesses. Note that the X-ray source detected by BeppoSAX had a soft spectrum at the beginning of this season and a hard spectrum by mid-season [19, 20]. It is probable that the behavior of these lines is sensitive

to the X-ray flux from the compact component; we observed a decline in the line fluxes after a weak local X-ray burst. Thus, lines showing He I-type behavior may be formed close to the compact component, possibly in the accretion disk.

Si II Type

An intensity increase in outburst by a factor of 6 to 18, followed by a gradual slow fading. There is no clear observational evidence for a cyclic 1100-day variation. In addition to the Si II $\lambda6347$ Å line, similar behavior is demonstrated by two more lines—Fe II $\lambda6148$ and 6492 Å (Fig. 5c, two bottom graphs).

[N II] Type

The [N II] $\lambda5755$ Å line is present in both the blue and red spectra, so its variations can be followed most thoroughly (Fig. 5c, top). During the outburst, the emission was very weak but detectable, and its equivalent width gradually increased during the brightness decline (Fig. 5c, top). It reached its maximum after the end of the outburst then gradually decreased. During the outburst the flux in this line was constant for ≈ 50 days but suddenly increased by a factor of 1.5 about 250 days later, when the fluxes of all other emission lines had decreased to their quiescent levels;
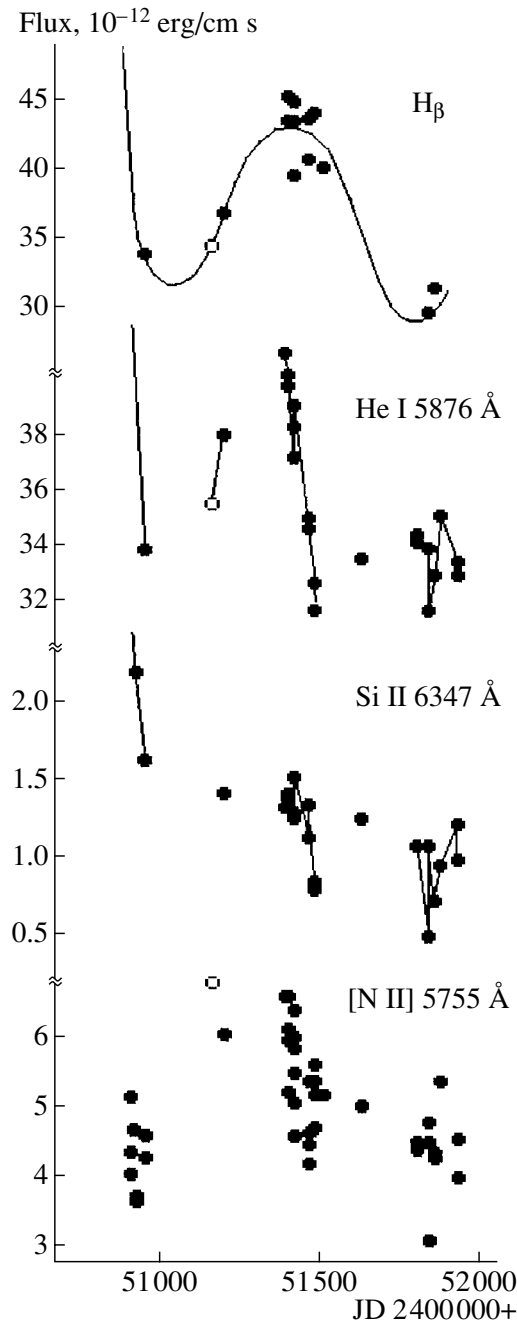
Fig. 6. Time dependences of the fluxes in lines showing different types of behavior.

it had again decreased to its outburst level by early 2001 (Fig. 6, bottom).

The [N II] λ5755 Å forbidden line can only form in extremely rarefied media, which can exist only at the outer boundary of a gas and dust envelope as dense as that of CI Cam. If we suppose that this line's brightening is due to the arrival of a wave of radiation emitted in the outburst to the outer parts of the envelope, the envelope's outer radius is *at least* 50 light days, equivalent to $5''-8''$ for the known distance to

the star. Images with deep limiting magnitudes and in broad photometric bands do not show such a nebula. Accurate measurements of our spectrograms taken with the 6-m telescope with $2''-3''$ resolution show that the brightness-distribution profiles along the slit in the continuum and the [N II] λ5755 Å emission are very similar (they coincide to within $3-5\%$ of the profile half width!). Thus, the above hypothesis can be rejected.

An alternative is that the emission brightening 50
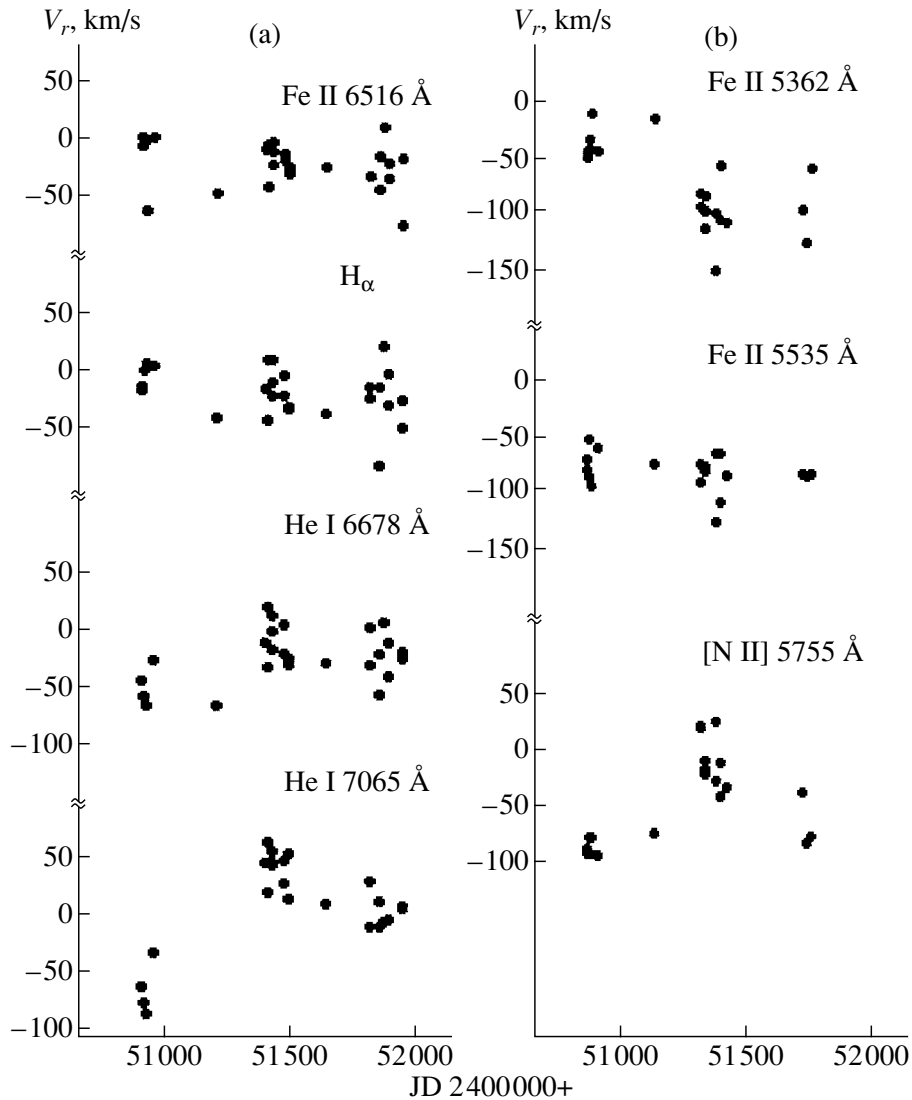
Fig. 7. Radial-velocity curves for some emission lines: (a) in the red, referred to the O_2 $\lambda 6872$ Å absorption band; (b) in the blue, referred to the [O I] $\lambda 5577$ Å telluric line.

to 250 days after the outburst is due to an ejection of rarefied matter beyond the envelope, when some density wave generated by the outburst reaches the outer envelope boundary. The rate of propagation of the wave, 1200 km/s, can be inferred from the widths of the emission line pedestals during the outburst [15, 23]. In this case, the envelope's outer radius is *at least* $0''.02–0''.03$, which is beyond the accuracy of our measurements of a spectrum's width along the slit. A gaseous medium with number density $> 10^5–10^6$ atoms/cm^3 could extend to this angular distance.

The five types of spectral-line behavior confirm the existence of a stratified envelope in the system; the H_α-type behavior, with 1100-day cyclic variations in the equivalent widths of some lines, provides evidence for the presence of a giant in the system, with the re-

flection effect acting on its surface facing the compact object. Figure 8 displays the dependences of the flux ratios in some emission lines on the line total excitation potential during the outburst and in quiescence on a logarithmic scale. The clear dependence between the amplitude of the outburst and the excitation potential confirms the envelope's stratification; matter in the envelope is more strongly ionized and excited the closer it is to the radiation source and the stronger this source is.

(b) Radial velocities

When calibrating the radial velocities for the spectra taken with the UAGS spectrograph of the 1-m Zeiss telescope, we noted considerable systematic errors in the dispersion curve, which varied by 2–3 Å from night to night. These variations are probably due
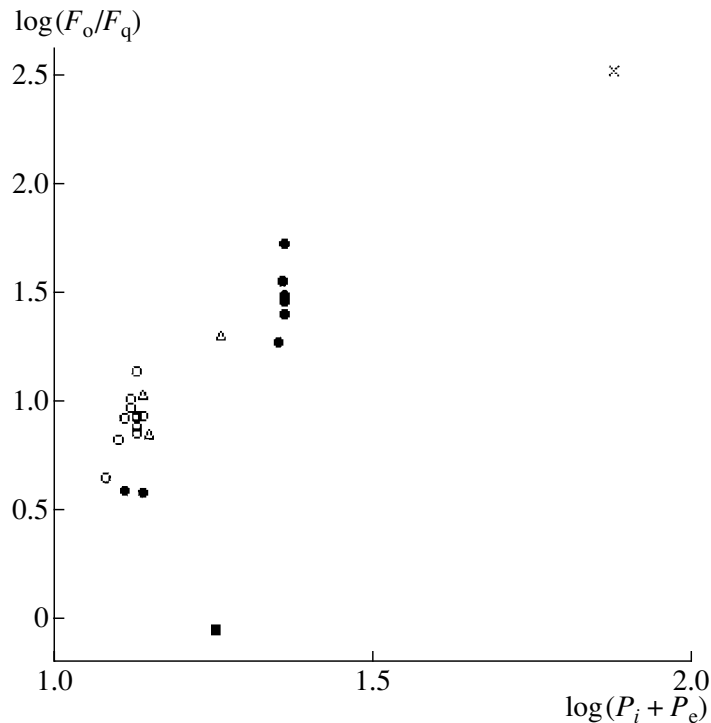
Fig. 8. Dependences of the ratios of fluxes in emission lines during the outburst (F_o) and in quiescence (F_q) on the total excitation potential (the sum of the ionization potential P_i and the excitation potential P_e) on logarithmic scales. The cross marks the He II $\lambda4686$ Å line; the filled circles are He I lines and He I type Fe II lines, the open circles the Balmer lines and Fe II lines showing H_α-type behavior, the triangles lines with Si II-type behavior, and the filled square the [N II] $\lambda5755$ Å line.

to flexing of the instrument. Nevertheless, the internal accuracy in the approximation of the dispersion curves is 0.2−0.4 Å, or 10−20 km/s in velocity. To reduce the systematic errors in our radial velocities, we referred the velocity scale to telluric lines. For the blue spectra, we used the bright sky line, [O I] $\lambda5577$ Å, and for the red spectra, the head of the atmospheric absorption band, O_2 $\lambda6872$ Å, which at our spectral resolution does not resolve into components, appears rather symmetrical, and is a good reference. The systematic difference in the radial velocities for lines in the red and blue may be due to inaccuracy in our determination of the effective wavelength for the O_2 band. Both the sky line and the absorption band are visible in all the spectra. Thus, we were able to obtain uniform series of radial velocities for H_α, [N II] $\lambda5755$ Å and several Fe II and He I lines that are close to the selected reference lines in the spectrum. For the sake of uniformity, we referenced the spectra from the 6-m telescope in the same way. The radial-velocity curves for the selected lines are shown in Fig. 7.

H_α and the Fe II $\lambda5535$ and 6516 Å lines show no radial velocity changes, including during the outburst. This can be understood if the emission source is on the surface of the secondary, near the inner

Lagrangian point; i.e., very close to the system's center of mass. Note that, in a system with an orbital period as high as 1100 days, the velocity amplitudes of the components are expected to be low. A season-to-season radial-velocity variation is observed in the He I $\lambda6678$ and 7065 Å lines; during the outburst, they exhibit a significant systematic velocity of 50−100 km/s toward the observer. This systematic velocity in the helium lines during the outburst could be due to partial screening of the red part of the line profile by matter in the plane of a disk inclined toward the line of sight. A similar systematic velocity with the opposite direction is observed for the Fe II $\lambda5362$ Å line during the outburst. The forbidden [N II] $\lambda5755$ Å line also displays a positive deviation of its velocity during the season of maximum brightness. These lines are probably formed far from the accretion disk, making their behavior different from that of the He I lines. Our observations are encouraging for future observational studies, since they show that the system's orbital motion can be detected in moderate-dispersion spectra in some lines (for example, the He I lines). Additional observations covering at least one more possible orbital cycle are needed.

4. CONCLUSIONS

We have seen that photometric and spectroscopic observations of CI Cam paint a picture of a stellar system with an orbital period of about 1100 days consisting of a giant star and a compact object. The hot continuum may be due to an accretion disk or matter surrounding the compact object. The system is immersed in a dense, strongly stratified gas and dust envelope, similar to the situation with symbiotic systems. Some fraction of the giant's surface near the inner Lagrangian point is heated, giving rise to the reflection effect (at least at the current epoch). The giant may have a late spectral type of G8II—K0II [5, 7].

The compact object may have a strong magnetic field, with the magnetic-dipole axis inclined relative to the rotational axis and a rotational period of $11\overset{d}{.}72$. In quiescence, accretion onto the compact object occurs from the dense circumstellar medium along magnetic-field lines, and we observe hot spots or accretion columns at the poles of the dipole, as occurs for "polars"—dwarf stellar systems. The contribution of the hot spots to the system's total radiation is small, and the amplitude of the variability due to the rotation of the compact object is 3% in V and even less in other bands. However, according to Miroshnichenko [5], this contribution may have been a factor of five higher prior to the outburst. During the outburst, ionized matter changes the structure of the magnetic field. The plasma is accelerated to relativistic speeds ($\approx 0.25\ c$) along the curved dipole lines. Coriolis forces exert significant pressure on the magnetic-field lines, causing the field is be wrapped up in a narrow tube. This could be the mechanism for collimating the jets. The detection of synchrotron radio emission from the jets means that the jet plasma is moving in a strong magnetic field.

Of course, new observations and theoretical computations are needed to test and refine this picture. Accurate photometry and medium-resolution spectroscopic observations covering at least one 1100-day cycle should be able to determine whether the variability cycle reflects the real orbital period. A joint analysis of original VLA radio maps and accurate photometric data could refine our picture of the jet flows and the mechanism for their ejection.

The most well-grounded explanation for the nature of the compact component and the origin of the April 1998 outburst of CI Cam is that the system contains a white dwarf, with the outburst being associated with a thermonuclear explosion of matter accreted onto its surface. This hypothesis is based on the following evidence [19]. First, the two-temperature thermal spectrum of the X-ray radiation during the outburst and the approximately one-week duration of the outburst are in agreement with Iben's [30] computations of a nuclear outburst on the surface of a hot white dwarf with $\approx 1M_\odot$ mass. (However, in similar outbursts in flare novae, no X-rays are observed.) Second, there is no rapid variability (in X-rays or the optical). Third, an expanding envelope is observed in the radio, which can be explained by the ejection of helium- and hydrogen-rich layers as a result of a thermonuclear explosion (supported by the appearance of pedestals of emission in the H and He I lines during the outburst). According to [19], the hypothesis that the system contains a neutron star cannot be completely ruled out.

Known X-ray novae with black-hole components exhibit excesses over a power-law spectrum in hard X-rays and rapid X-ray variations during outbursts, which are not observed for CI Cam. Thus, it is unlikely that the compact component in the CI Cam is a black hole. The presence of a normal OB star in the system is also ruled out in [19], since the quiescent X-ray flux from CI Cam is higher than expected by two orders of magnitude.

The main conclusions of our study are the following.

(1) We have detected a 1100-day variability cycle in photometric data for CI Cam, as well as in the fluxes of some low-excitation emission lines. The cycle could result from orbital motion in a widely separated system with a giant and the action of the reflection effect at its surface.

(2) Our V-band photometry confirms the $11\overset{d}{.}7$ period found by Miroshnichenko [5] before the 1998 outburst. Model computations show that this period can be identified with the rotational period for the relativistic radio jets. Modeling the radio map, we estimated the inclination of the jet rotational axis to the line-of-sight angle, $i = 35°-40°$, between the rotational axis and the jet ejection direction, $\theta = 7°-10°$, and intrinsic velocity of the jet, $0.23-0.26\ c$.

(3) We have discovered a connection between the behavior of different emission lines and their formation regions, due to stratification in the envelope. We observed rapid variability in the fluxes of helium and some iron emission lines, probably due to variations in the X-ray flux in quiescence. The outburst of the [N II] $\lambda5755$ Å forbidden line was delayed $50-250$ days relative to the peak of the outburst in the optical, X-ray, and radio.

(4) Our analysis of the amplitudes of the outburst in different spectral lines indicates a relationship between the amplitude of line-flux variations and the line-excitation potential.

ACKNOWLEDGMENTS

REFERENCES

1. H. J. G. L. M. Lamers, F.-J. Zickgraf, D. de Winter, *et al.*, Astron. Astrophys. **340**, 117 (1998).
2. P. W. Merrill, M. L. Humasson, and C. G. Burwell, Astrophys. J. **76**, 156 (1932).
3. P. W. Merrill and C. G. Burwell, Astrophys. J. **78**, 97 (1933).
4. R. A. Downes, Publ. Astron. Soc. Pac. **96**, 807 (1984).
5. A. S. Miroshnichenko, Astron. Astrophys. Trans. **6**, 251 (1995).
6. Yu. K. Bergner, A. S. Miroshnichenko, R. V. Yudin, *et al.*, Astron. Astrophys., Suppl. Ser. **112**, 221 (1995).
7. A. S. Miroshnichenko, Odessa Astron. Publ. **7**, 76 (1994).
8. Ya. N. Chkhikvadze, Astrofizika **6**, 65 (1970).
9. D. Smith, R. Remillard, J. Swank, *et al.*, IAU Circ., No. 6855 (1998).
10. T. Belloni, S. Dieters, M. E. van den Ancker, *et al.*, Astrophys. J. **527**, 345 (1999).
11. Y. Ueda, M. Ishida, H. Inoue, *et al.*, Astrophys. J. Lett. **508**, L167 (1998).
12. E. L. Robinson, W. F. Welch, M. T. Adams, and M. E. Cornell, IAU Circ., No. 6862 (1998).
13. E. A. Barsukova, S. N. Fabrika, S. A. Pustilnik, and A. V. Ugryumov, Bull. Spec. Astrophys. Obs. **45**, 145 (1998).
14. J. S. Clark, I. A. Steele, R. P. Fender, and M. J. Coe, Astron. Astrophys. **348**, 888 (1999).
15. E. A. Barsukova and S. N. Fabrika, *Variable Stars—The Key to Understanding the Structure and Evolution of the Galaxy* [in Russian], Ed. by N. N. Samus' and A. V. Mironov (Cygnus, Nizhni Arkhyz, 2000), p. 154.
16. J. S. Clark, A. S. Miroshnichenko, V. M. Larionov, *et al.*, Astron. Astrophys. **356**, 50 (2000).
17. R. M. Hjellming and A. J. Mioduszewski, Sky Telesc. **96** (2), 22 (1998).
18. R. M. Hjellming and A. J. Mioduszewski, IAU Circ., No. 6872 (1998).
19. M. Orlandini, A. N. Parmar, F. Frontera, *et al.*, Astron. Astrophys. **356**, 163 (2000).
20. A. N. Parmar, T. Belloni, M. Orlandini, *et al.*, Astron. Astrophys. **360**, L31 (2000).
21. V. G. Kornilov, I. M. Volkov, A. I. Zakharov, *et al.*, *Catalogue of WBVR Values for Bright Stars of the North Sky* (Mosk. Gos. Univ., Moscow, 1991), Tr. Gos. Astron. Inst., Mosk. Gos. Univ. **63**.
22. M. R. Garsia, P. Berlind, E. Barton, and J. E. McClintock, IAU Circ., No. 6865 (1998).
23. R. I. Hynes, P. Roche, C. A. Haswell, *et al.*, IAU Circ., No. 6871 (1998).
24. T. J. Deeming, Astrophys. Space Sci. **36**, 173 (1975).
25. T. Kato and M. Uemura, Inf. Bull. Var. Stars, No. 5081 (2001).
26. E. L. Chentsov, V. G. Klochkova, and N. S. Tavolganskaya, Bull. Spec. Astrophys. Obs. **48**, 21 (1999).
27. A. R. Striganov and N. S. Sventitskiĭ, *Tables of Spectral Lines of Neutral and Ionized Atoms* (Atomizdat, Moscow, 1966; Plenum, New York, 1968).
28. S. Heung, L. H. Aller, W. A. Feibelman, *et al.*, Mon. Not. R. Astron. Soc. **318**, 77 (2000).
29. A. B. Meinel, A. F. Aveni, and M. W. Stockton, *Catalog of Emission Lines in Astrophysical Objects* (Univ. of Arizona, Tucson, 1969, 2nd ed.).
30. I. Iben, Astrophys. J. **259**, 244 (1982).

Translated by N. Samus'

A Study of Class II Methanol Maser Condensations in the Star-Forming Region W48

I. V. Val'tts and S. Yu. Lyubchenko

Astro Space Center, Lebedev Physical Institute, Russian Academy of Sciences, Profsoyuznaya ul. 84/32, Moscow, 117810 Russia
Received April 12, 2001

Abstract—The methanol-line spectra in two maser condensations at velocities ~ 41 and ~ 45 km/s in the star-forming region W48 have been studied. The intensity of the $2_0 - 3_{-1}E$ (12.2 GHz) line is anticorrelated with that of the $5_1 - 6_0A^+$ (6.7 GHz) line: the intensity of the $5_1 - 6_0A^+$ (6.7 GHz) line is greater at ~ 41 km/s than at ~ 45 km/s, while the opposite is true of the $2_0 - 3_{-1}E$ (12 GHz) line. The remaining class II methanol lines in this source demonstrate the same behavior as the $2_0 - 3_{-1}E$ (12 GHz) line. This contradicts current concepts about the maser line intensities in various methanol transitions: according to model calculations, the intensities of all class II lines should vary in phase. This effect is confirmed for a large homogeneous sample of 67 sources. Possible explanations of the observed effect are proposed; one suggests the possible role of "transpumping" of the methanol-level populations in the maser condensations. The relationships between the variations of the $2_0 - 3_{-1}E$ (12 GHz) and $5_1 - 6_0A^+$ (6.7 GHz) line intensities, which are present for all 67 sources considered, may indicate that the condensations are at different distances from the pumping source. The presence of condensations at various distances from the pumping source in all 67 sources can be understood if they are ice planets revolving in different orbits around massive stars or protostars. © *2002 MAIK "Nauka/Interperiodica".*

1. INTRODUCTION

Stars form in dense molecular clouds. Young objects at the prestellar stage of their evolution are usually embedded so deeply in a dense gas-dust medium that their presence in a star-forming region can be inferred only indirectly. Protostars influence the state of the parent molecular cloud surrounding them. The cloud is heated and ionized, expands, and decays into separate fragments. Naturally, the molecular-cloud density is nonuniform, and dense and tenuous fragments evolve differently. The spectrum of protostar masses is also diverse: from low-mass T Tau stars ($0.1 - 3M_\odot$) to giants containing tens of solar masses. The evolution of the surrounding medium depends most strongly on the protostar mass. The spectrum of protostar masses, density spectrum for molecular cloud inhomogeneities, and timescale for cloud–protostar dynamical interactions determine the observed morphology of a star-forming region. By-products of evolution are usually visible in star-forming regions: dark globules, Herbig–Haro objects, cool clumps of dust (in the far infrared), hot-dust cocoons (in the near infrared), ultracompact H II regions (in the radio continuum), and powerful outflows of molecular material in the form of bipolar jets and dense molecular cores that radiate strong nonequilibrium (maser) emission of various

molecules (OH, H_2O, CH_3OH), as well as thermal emission in the lines of more complex molecules. These objects have received the greatest attention in studies of the evolution of star-forming regions. The plausibility of an evolutionary scenario for a star-forming region depends strongly on the completeness and uniformity of data on the physical state of the matter in these peculiar objects and also on how precisely we can estimate their locations in the cloud; i.e., on their mutual relationships and connection with the protostar. In this paper, we report the results of multifrequency studies of the active star-forming region W48 in lines of methanol—the most informative molecule in the interstellar medium.

2. DESCRIPTION OF THE W48 REGION

The idea that there is a connection between very young stars and dense molecular clouds is now well grounded. At the same time, no stellar associations or other optical objects have been found in the star-forming region W48, although a cluster of H II regions is present (the distance to W48 is 3.1 kpc [1]). The most compact of these is G35.20−1.74. The 5-GHz VLA map of W48 presented in [2] is dominated by the compact core of the H II region G35.20−1.74, offset by 15″ relative to the infrared source IRS1, and an extended component, which
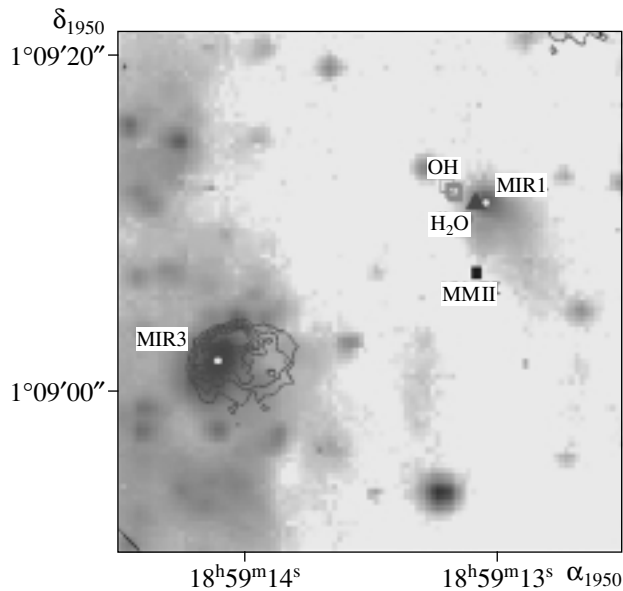
Fig. 1. Map of W48 from [6]: NIR emission in the K band (2.2 μm, gray scale), the H II region at 6 cm (contours), OH masers (open squares show the positions of maser features), the H_2O maser at the peak of the nonstellar extended NIR source (HC1 , filled triangle), the sources MIR1 and MIR3 (open circles), and the methanol maser (MMII, filled square, coordinates taken from [7]).

encompasses the other infrared source, IRS2. There are two H_2O masers (HC1 and HC2) In the region of G35.20−1.74 [3]. The maser HC1 is located 20″ to the northwest of an ultracompact H II region, and the HC2 lies 40″ further in the same direction. There is an OH maser with a very close projected distance from HC1 (not exceeding 3000 AU)[4]. In addition to the IRAS wavelengths (20−100 μm), the W48 region has been studied in the submillimeter at 850 μm [5], as well as in the near infrared (NIR) and mid-infrared (MIR) at 1−2 and 11.2 μm, respectively [6]. The 850-μm continuum peak lies between the radio continuum peak and the OH−H_2O maser (HC1). Six sources have been detected at 11.2 μm; the brightest (MIR3) coincides with an ultracompact H II region, while the source with the greatest mid-infrared excess (MIR1) is associated with the OH−H_2O maser (HC1). Figure 1 presents the map of W48 from Persi et al. [6], showing the NIR emission in the K band (2.2 μm), the H II region (VLA, 6 cm), and the OH−H_2O maser (HC1) at the peak of the nonstellar extended NIR source. We have also plotted the position of the methanol maser (taken from [7]) and marked the positions of the sources MIR1 and MIR3 according to [6]. In [6], the two masers and extended NIR source are interpreted as a very young protostellar object at the accretion phase of its evolution, embedded in a hot dust envelope. The coincidence of this object with the masers indicates that the maser emission appears

at a very early stage of the protostellar evolution, when there is not yet any radio continuum. UCH II appears to be an older object, and the stars and diffuse H II region are older still. Persi et al. [6] believe that all these objects evolve completely independently, although they are located within the same molecular complex.

3. STUDY OF W48 IN THE METHANOL LINES

3.1. Observations and Results

Numerous methanol maser lines have been detected in W48, all belonging to class II; in other words, emission is observed only between levels of the $K = -1$, $K = 0$ ladders for A-methanol and the $K = 0$, $K = -1$ ladders for E-methanol. Methanol-line emission was first detected in this source (toward G35.20−1.74) in the $2_0 - 3_{-1}E$ transition at 12 GHz by Norris et al. [8]. The observations were obtained on the 64-m Parkes radio telescope with a 2′ beam and 0.1 km/s resolution. A 6.7 GHz maser in the $5_1 - 6_0A^+$ transition was detected by Menten [9] in a survey carried out on the 43-m Green Bank radio telescope with a 5′ beam and resolutions of 0.44 and 0.055 km/s. Masers in the $3_1 - 4_0A^+$ transition at 107 GHz were detected using the 20-m Onsala radio telescope with a 35″ beam and 0.7 km/s resolution [10]. Observations on the 12-m Kitt Peak radio telescope with a 35″ beam and 0.37 km/s resolution revealed a series of maser lines at 157 GHz, in the $J_0 - J_{-1}E$ transitions [11]. Thermal emission was detected at 133 GHz, in the $5_{-2} - 6_{-1}E$ transition [12]. The lines at 229, 230, 165, and 108 GHz have not been detected [13]. Searches for class I maser lines at 44 GHz [14], 36 GHz [15], and 95 GHz [16] have yielded no positive results.

3.2. Comparative Analysis of Methanol Maser Lines in W48

Figure 2 shows the spectra of the methanol maser lines, as well as spectra of the OH and H_2O lines [17, 18]; line parameters derived from Gaussian approximations of the line profiles are listed in Table 1 (for the 6.7- and 12-GHz lines, the peak fluxes of the brightest feature are given). For comparison, the bottom graph of Fig. 2 shows the thermal CS line observed using the Onsala telescope [19]. We can see that the total velocity interval in which the maser lines are observed does not exceed the width of the CS line; i.e., all the maser lines form in the same molecular cloud. Figure 3 presents level diagrams for A- and E-methanol. The arrows denote transitions in which maser emission has been detected in W48.

Maser emission in class II A-methanol transitions has been observed at 6.7 GHz, 107 GHz, and (on a thermal pedestal) 157 GHz, in the $2_1 - 3_0$ line. The 6.7-GHz maser is very powerful (the peak flux of the brightest feature is 556 Jy), ranking eighth in intensity among 88 sources studied in [9].

A series of eight E-methanol lines is observed at 157 GHz, some of them maser lines [11]. The spectra of all these series were published in [11]; Figure 2 shows one line of this series, $5_0 - 5_{-1}E$, as an example. Such masers are rare and have been detected in only three other sources among 94 star-forming regions studied—W3(OH), Cep A, and G345.01+1.79 [11, 12].

Let us consider some important features of the methanol maser emission in W48. Two groups of maser features are observed in velocity intervals near 41 km/s and 45 km/s; the $5_{-2} - 6_{-1}E$ (133 GHz) thermal line displays only one feature at about 43 km/s. The line-intensity distribution at $\sim$41 km/s is well described by existing model calculations (see, for example, [21−23]), according to which a decreasing intensity of the $5_1 - 6_0A^+$ (6.7 GHz) line should be accompanied by a decrease in the intensities of other class II lines, such as $3_1 - 4_0A^+$ (107 GHz), $2_1 - 3_0A^+$ (157 GHz), and $2_0 - 3_{-1}E$ (12 GHz). At the same time, as the intensity of the $5_1 - 6_0A^+$ (6.7 GHz) feature at $\sim$45 km/s decreases (compared to the feature of this same line at $\sim$41 km/s), the intensities of all 45-km/s maser features in the $2_1 - 3_0A^+$ (157 GHz), $J_0 - J_{-1}$ (157 GHz), $2_0 - 3_{-1}E$ (12 GHz), and, probably, $3_1 - 4_0A^+$ (107 GHz) lines grow compared to the intensities of the $\sim$41-km/s features of these lines. This is especially obvious for A-methanol, since the observed lines belong to completely analogous transitions (Fig. 3).

VLBI observations of the methanol maser [24] have shown good positional coincidence between the 6.7-GHz condensations and 12-GHz condensations at the same velocities. The groups of condensations at $\sim$41 km/s and $\sim$45 km/s are clearly visible on the VLBI map, and the centers of the groups are spatially separated by $\sim$500 AU [24, Fig. 6]. The pumping mechanism for class II masers requires a source of infrared emission. If we suppose that these groups have a common (external) source of pumping, such as the ultracompact H II region G35.20−1.74, the pumping conditions in these groups will be the same. If the physical conditions in the first group of condensations ($\sim$41 km/s) differ from those in the second group ($\sim$45 km/s), but are approximately the same for individual condensations within each group, their differences should not influence the line intensity
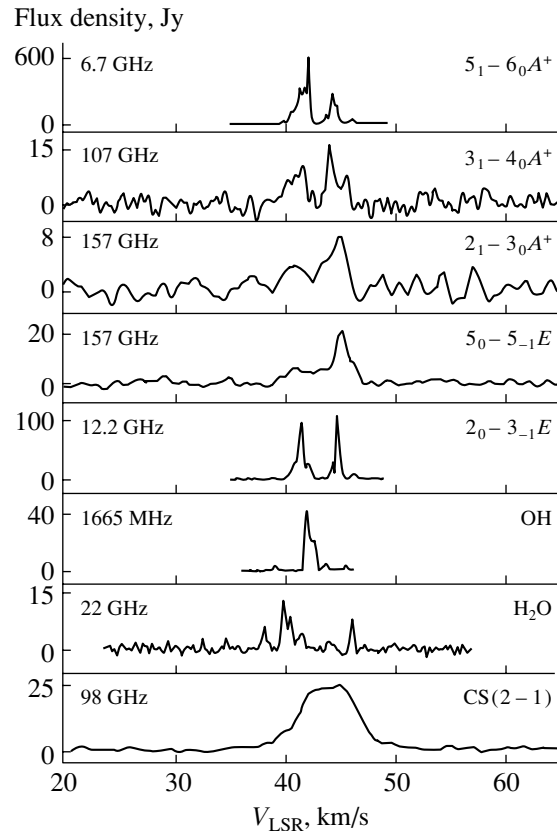

Fig. 2. Spectra of the maser lines in W48 and structure of the thermal CS line profile. See the description of the spectra in the text.

ratios of each group in the opposite sense, in accordance with current concepts about the formation of level populations. In other words, if the physical conditions in one group of condensations are such that the $5_1 - 6_0A^+$ (6.7 GHz) line is brighter than this line in the second group, the $2_0 - 3_{-1}E$ (12.2 GHz) line in the second group cannot be brighter than the corresponding line in the first group. If the physical conditions inside the condensations differ, which is quite possible given the fairly large distances between the condensations within each group (of the order of 100 AU, according to the map of [24]), the intensity ratios of the $5_1 - 6_0A^+$ (6.7 GHz) and $2_0 - 3_{-1}E$ (12.2 GHz) lines in the spectrum can be arbitrary, even if there is a common source of pumping, as if they were completely different, physically unrelated sources. In this case, the behavior of the spectrum of W48 noted above has a random character.

Therefore, to investigate the effect detected, we must use averaged, statistically significant data. As noted above, 157-GHz maser emission is a rare phenomenon; therefore, the effect can be studied statistically only using the intensity ratios for the most common lines—$5_1 - 6_0A^+$ (6.7 GHz) and $2_0 - 3_{-1}E$

Table 1. Two features of the maser and quasi-maser lines in various methanol transitions in W48

Transition (frequency, GHz)	First feature $V \sim 41$ km/s			Second feature $V \sim 45$ km/s			Reference
	V, km/s	ΔV, km/s	S_ν, Jy	V, km/s	ΔV, km/s	S_ν, Jy	
$5_1 - 6_0 A^+$ (6.7)	42.3	−	560	44.6	−	260	[7]
$2_0 - 3_{-1} E$ (12.2)	42.3	−	22	44.6	−	109	[7]
$3_1 - 4_0 A^+$ (107)	41.1	1.7	9.2	44.3	2	8.2	[20]
$2_1 - 3_0 A^+$ (157)	41.2	4.2	3.2	44.8	1.7	7.4	[11]
$1_0 - 1_{-1} E$ (157)	42.1	3.4	7.4	45.7	2.1	2.5	[11]
$2_0 - 2_{-1} E$ (157)	42.1	3.4	5.8	45.7	2.1	6.9	[11]
$3_0 - 3_{-1} E$ (157)	42.1	3.4	4.5	45.7	2.1	4.6	[11]
$4_0 - 4_{-1} E$ (157)	41.7	3.8	6.8	45.5	2.5	16.0	[11]
$5_0 - 5_{-1} E$ (157)	41.7	3.1	5.8	45.1	1.7	19.5	[11]
$6_0 - 6_{-1} E$ (157)	41.3	2.6	8.4	45.1	2.0	18.1	[11]
$7_0 - 7_{-1} E$ (157)	41.8	3.7	5.4	45.2	1.4	16.4	[11]
$8_0 - 8_{-1} E$ (157)	42.3	5.3	5.1	45.4	1.7	12.0	[11]

(12 GHz)—in sources whose spectra have at least two features in each of these lines located at different velocities. The most complete and homogeneous data on the $5_1 - 6_0 A^+$ (6.7 GHz) and $2_0 - 3_{-1} E$ (12 GHz) lines (for 131 sources) are presented in [7]. For 67 of these sources, data for pairs of features in the 6.7- and 12-GHz lines are listed in [7]; Table 2 lists the source names, velocities of the features, and fluxes at these frequencies.

3.3. Spectra of Sources with Two Features in the $5_1 - 6_0 A^+$ (6.7 GHz) and $2_0 - 3_{-1} E$ (12 GHz) Lines

For convenience, we will call two corresponding lines for the $5_1 - 6_0 A^+$ (6.7 GHz) and $2_0 - 3_{-1} E$ (12 GHz) transitions "pairs." The peculiarity in the intensity ratios for features in the $5_1 - 6_0 A^+$ (6.7 GHz) and $2_0 - 3_{-1} E$ (12 GHz) lines noted in the spectrum of W48 is present in the spectra of all sources with pairs of line features listed in Table 2. Figures 4a and 4b show the average flux densities for the corresponding $5_1 - 6_0 A^+$ (6.7 GHz) and $2_0 - 3_{-1} E$ (12 GHz) lines for 67 sources, with the flux densities for pairs for which the $5_1 - 6_0 A^+$ (6.7 GHz) feature is stronger and those for which this feature is weaker plotted separately. The average flux density in the $5_1 - 6_0 A^+$ (6.7 GHz) line for the pairs with a stronger $5_1 - 6_0 A^+$ (6.7 GHz) feature is twice that for the pairs with a weaker $5_1 - 6_0 A^+$ (6.7 GHz) feature; in contrast, the average flux density in the $2_0 - 3_{-1} E$ (12 GHz) line for pairs with a stronger

$5_1 - 6_0 A^+$ (6.7 GHz) feature is half that for pairs with a weaker $5_1 - 6_0 A^+$ (6.7 GHz) line. For pairs with a stronger $5_1 - 6_0 A^+$ (6.7 GHz) feature, the ratio of the average intensities of the $5_1 - 6_0 A^+$ (6.7 GHz) and $2_0 - 3_{-1} E$ (12 GHz) lines is 8.2, while this ratio is 2.6 for pairs with a weaker $5_1 - 6_0 A^+$ (6.7 GHz) feature. A description of Fig. 4c is given below.

Figure 5a presents the distribution of the differences in the velocities of the stronger and weaker features of the $5_1 - 6_0 A^+$ (6.7 GHz) line in the spectra of the 67 sources. This distribution shows that the velocity difference does not exceed the widths of typical thermal lines in molecular clouds, and is close to the width of the maser lines. Figure 5b shows the distribution of the magnitude of the velocity difference for the stronger and weaker features in the $5_1 - 6_0 A^+$ (6.7 GHz) line. The average velocity difference magnitude is 2.3 km/s. In other words, in all 67 sources, the $5_1 - 6_0 A^+$ (6.7 GHz) lines form within a single molecular cloud, probably in distinct, but spatially nearby, condensations. Thus, we expect that VLBI maps of these sources will probably be similar to the map obtained in [24] for W48.

Figure 6 shows the distributions of the ratios of the flux densities in the $5_1 - 6_0 A^+$ (6.7 GHz) and $2_0 - 3_{-1} E$ (12 GHz) lines in pairs with a stronger $5_1 - 6_0 A^+$ (6.7 GHz) line (Fig. 6a) and those with a weaker $5_1 - 6_0 A^+$ (6.7 GHz) line (Fig. 6b) on logarithmic scales. Figure 6c is discussed below. We can see from Figs. 6a and 6b that the ratios for pairs with a weaker $5_1 - 6_0 A^+$ (6.7 GHz) line are distributed in a narrower interval and correspond to approximately
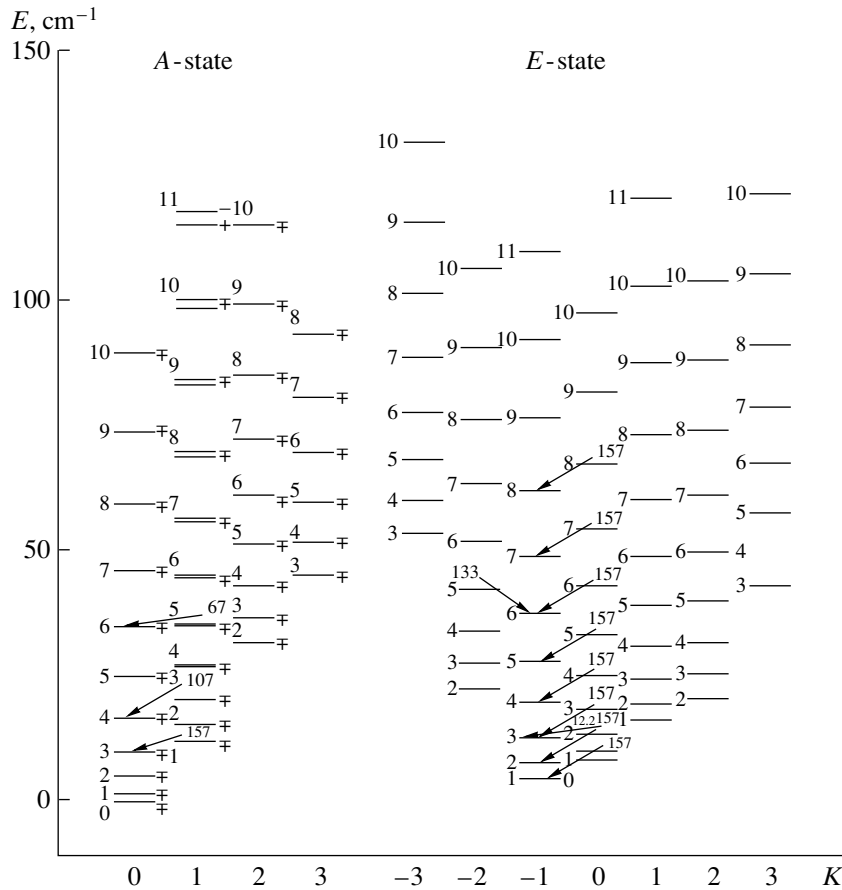
Fig. 3. Rotational-level diagram of the methanol molecule. The level labels show values of the rotational quantum number J. The horizontal axis indicates the quantum number K, corresponding to the projection of the rotational quantum number onto the molecular axis; the vertical axis indicates the level energy. The arrows show the transitions detected in W48, with the transition frequency in GHz given at the top of each arrow.

equal flux densities in the $5_1 - 6_0 A^+$ (6.7 GHz) and $2_0 - 3_{-1}E$ (12 GHz) lines; if $R = \frac{(S_{6.7}/S_{12.2})_{\text{strong}}}{(S_{6.7}/S_{12.2})_{\text{weak}}}$, then $\bar{R} = 40$ with dispersion $\sigma = 106$.

Figure 7 presents the relationships between the flux densities in the $5_1 - 6_0 A^+$ (6.7 GHz) and $2_0 - 3_{-1}E$ (12 GHz) lines for pairs with a stronger (Fig. 7a) and weaker (Fig. 7b) $5_1 - 6_0 A^+$ (6.7 GHz) line. Among the 67 sources, there are nine (Table 2) for which paper [7] lists only upper limits for the flux density in the $2_0 - 3_{-1}E$ (12 GHz) line in pairs with a stronger $5_1 - 6_0 A^+$ (6.7 GHz) line. In these cases, we have adopted the upper limits as the actual flux-density values and included these sources in the distributions in Figs. 4–7 in order to preserve the statistics of pairs with a weaker $5_1 - 6_0 A^+$ (6.7 GHz) line, in which the corresponding flux densities for the $2_0 - 3_{-1}E$ (12 GHz) lines have been measured. Note that, if we had values of the actual $2_0 - 3_{-1}E$ (12 GHz) flux densities for these nine sources rather than upper limits, these values would be lower than

the upper limits, strengthening the statistical conclusions derived from our analysis of the data in these figures.

Table 3 lists the parameters for our approximations of the data in Figs. 7a and 7b (not on logarithmic scales) by straight lines $y = Ax + B$ and the associated correlation coefficients. The thin line in Fig. 7a has been copied from Fig. 7b; the set of points in Fig. 7a is obviously bounded by this line from below. The thin line in Fig. 7b has been copied from Fig. 7a; nearly all points in Fig. 7b lie below this line. The boundedness of the sets of points in Figs. 7a and 7b appears to reflect a difference in the pumping mechanisms in the condensations emitting stronger and weaker $5_1 - 6_0 A^+$ (6.7 GHz) lines.

3.4. Spectra of Sources with a Single Feature in the $5_1 - 6_0 A^+$ (6.7 GHz) and $2_0 - 3_{-1}E$ (12 GHz) Lines

We now have a dependence between the intensities of the $5_1 - 6_0 A^+$ (6.7 GHz) and $2_0 - 3_{-1}E$

Table 2. Parameters of the methanol maser lines $5_1 - 6_0 A^+$ (6.7 GHz) and $2_0 - 3_{-1}E$ (12.2 GHz) with two features [7]

Source	Radial velocity (LSR), km/s	Flux density in the $5_1-6_0A^+$ (6.7 GHz) line, Jy	Flux density in the $2_0 - 3_{-1}E$ line (12.2 GHz) line, Jy
$213.71 - 12.60$	$+10.9$	90	4.2
	$+11.8$	337	0.5
$305.20 + 0.02$	-32.4	30	10.3
	-33.1	52	7
$305.20 + 0.21$	-45.0	15	2.3
	-44.0	50	1.9
$305.21 + 0.21$	-37.1	31	5.1
	-38.3	480	0.2
$308.92 + 0.12$	-53.3	14	10
	-54.8	54	1
$316.38 - 0.38$	-1.1	12	1.8
	-0.6	38	1.6
$316.81 - 0.06$	-46.8	4	1.2
	-45.7	12	0.5
$322.16 + 0.64$	-63.4	160	17
	-63.0	211	15.5
$323.74 - 0.26$	-50.8	2550	500
	-51.1	2860	250
$327.12 + 0.51$	-89.6	25	5
	-87.2	90	< 0.4
$327.29 - 0.58$	-48.1	1	0.9
	-48.5	2.6	0.75
$327.40 + 0.44$	-82.9	83	55
	-82.6	93	30
$328.25 - 0.53$	-37.0	220	3.3
	-37.4	430	1
$328.81 + 0.63$	-46.4	170	25
	-43.9	380	1
$329.03 - 0.20$	-39.7	28	7.2
	-42.0	30	< 0.2
$329.18 - 0.31$	-58.2	7.5	1.7
	-55.8	13	0.3
$329.41 - 0.46$	-65.6	0.4	0.6
	-66.8	156	< 0.3
$331.28 - 0.19$	-78.9	64	145
	-78.2	207	50
$331.56 - 0.12$	-104.1	17	6
	-103.6	47	1.6
$335.55 - 0.31$	-114.7	3.6	5
	-116.4	23	0.9

Table 2. (Contd.)

Source	Radial velocity (LSR), km/s	Flux density in the $5_1 - 6_0 A^+$ (6.7 GHz) line, Jy	Flux density in the $2_0 - 3_{-1} E$ (12.2 GHz) line, Jy
335.79 + 0.17	−46.2	110	126
	−48.5	167	14
336.36 − 0.14	−74.7	4.5	2.3
	−73.6	21	1.6
336.86 + 0.01	−75.6	4.5	0.6
	−76.1	34	0.3
338.46 − 0.25	− 52.1	70	8.5
	− 50.6	83	< 0.3
339.62 − 0.12	− 33.4	35	18.4
	− 36.1	83	0.3
340.79 − 0.10	− 105.2	132	43
	− 106.7	242	2
341.22 − 0.21	− 37.3	54	5.1
	− 37.8	167	5
343.93 + 0.12	+13.7	6.1	3.9
	+14.4	11	0.5
345.01 + 1.79	− 21.8	338	310
	− 17.9	508	2
347.86 + 0.02	− 36.4	1.9	0.9
	− 29.3	7.2	0.5
347.90 + 0.05	− 27.2	4	2
	− 27.6	5.3	1.6
348.55 − 0.98	− 10.0	41	5.6
	− 12.9	74	< 0.4
348.72 − 1.04	− 7.4	85	11
	− 7.8	90	6
349.07 − 0.02	+11.7	1.4	0.75
	+6.9	1.9	< 0.4
351.42 + 0.64	− 11.2	2250	1210
	− 10.4	3300	1100
353.41 − 0.36	− 22.3	29	19.5
	− 19.9	90	4.2
354.61 + 0.47	− 16.5	40	28
	− 23.1	216	12
359.61 − 0.24	+22.7	16	13.5
	+19.9	48	2
0.55 − 0.85	+18.4	9	3.9
	+13.8	68	3.6
8.68 − 0.37	+42.2	14	14
	+43.0	148	2.8

Table 2. (Contd.)

Source	Radial velocity (LSR), km/s	Flux density in the $5_1 - 6_0 A^+$ (6.7 GHz) line, Jy	Flux density in the $2_0 - 3_{-1} E$ (12.2 GHz) line, Jy
$10.45 - 0.02$	$+71.9$	19	7
	$+73.3$	25	6.4
$10.62 - 0.38$	$+5.8$	2	1.2
	$+4.7$	3.6	0.5
$11.94 - 0.62$	$+39.8$	26	6.8
	$+32.1$	47	5.2
$12.03 - 0.03$	$+108.7$	46	13.5
	$+107.7$	82	0.8
$12.68 - 0.18$	$+57.0$	195	16.5
	$+52.2$	544	0.5
$19.48 + 0.15$	$+20.8$	3.2	2.9
	$+21.2$	19.3	1.6
$19.61 - 0.14$	$+50.6$	4.3	2.8
	$+56.6$	18	0.3
$20.23 + 0.07$	$+73.2$	19	2.7
	$+71.8$	100	0.9
$22.43 - 0.16$	$+37.8$	14	5
	$+29.3$	20	0.8
$23.01 - 0.41$	$+74.9$	280	28
	$+75.3$	405	8
$23.44 - 0.18$	$+103.8$	38	17
	$+103.0$	77	0.5
$28.83 - 0.25$	$+82.3$	1.2	3.1
	$+83.4$	73	1.7
$29.86 - 0.05$	$+100.3$	35	13
	$+101.3$	67	3.5
$29.95 - 0.02$	$+96.8$	75	53
	$+96.0$	206	39
$30.20 - 0.17$	$+110.2$	15.5	10
	$+108.5$	18.7	6.7
$30.22 - 0.18$	$+112.8$	9.8	2.8
	$+113.6$	11.7	1.2
$30.76 - 0.05$	$+91.7$	14	1.5
	$+92.0$	68	0.9
$30.79 + 0.20$	$+87.8$	19	11.5
	$+85.9$	23	3.2
$30.82 - 0.05$	$+108.3$	6	0.8
	$+101.3$	18	0.1
$31.41 + 0.31$	$+95.6$	10.5	2.1
	$+103.5$	11	< 0.1

Table 2. (Contd.)

Source	Radial velocity (LSR), km/s	Flux density in the $5_1 - 6_0 A^+$ (6.7 GHz) line, Jy	Flux density in the $2_0 - 3_{-1} E$ (12.2 GHz) line, Jy
32.74 − 0.08	+30.5	14	10.5
	+38.5	47	7.5
33.09 − 0.07	+104.4	12	0.4
	+95.6	30	< 0.1
34.24 + 0.13	+61.2	5.1	0.9
	+55.4	20	0.4
35.20 − 0.74	+30.6	12	31
	+28.5	125	29
35.20 − 1.74	+44.6	260	109
	+42.3	560	22
43.17 + 0.01	+21.9	3	1
	+20.2	12.8	< 0.4
59.78 + 0.06	+27.1	13	15.8
	+25.0	42	1.7

Table 3. $y = Ax + B$ approximation for the dependence between $S_\nu(6.7\ \text{GHz})$ and $S_\nu(12.2\ \text{GHz})$

No.	Set class	Approximation parameter A	Approximation parameter B	Correlation coefficient r
1	Pairs with a stronger $5_1 - 6_0 A^+$ (6.7 GHz) line (Fig. 7a)	3.3 ± 0.3	126.0 ± 6.3	$r = 0.85$
2	Pairs with a weaker $5_1 - 6_0 A^+$ (6.7 GHz) line (Fig. 7b)	2.2 ± 0.2	19.2 ± 6.8	$r = 0.87$
3	Sources with single $5_1 - 6_0 A^+$ (6.7 GHz) lines (Fig. 8a)	2.2 ± 0.1	48.6 ± 4.5	$r = 0.92$
4	Pairs with weaker $5_1 - 6_0 A^+$ (6.7 GHz) lines and all sources with single $5_1 - 6_0 A^+$ (6.7 GHz) lines (Fig. 8b)	2.2 ± 0.1	33.6 ± 4.2	$r = 0.89$
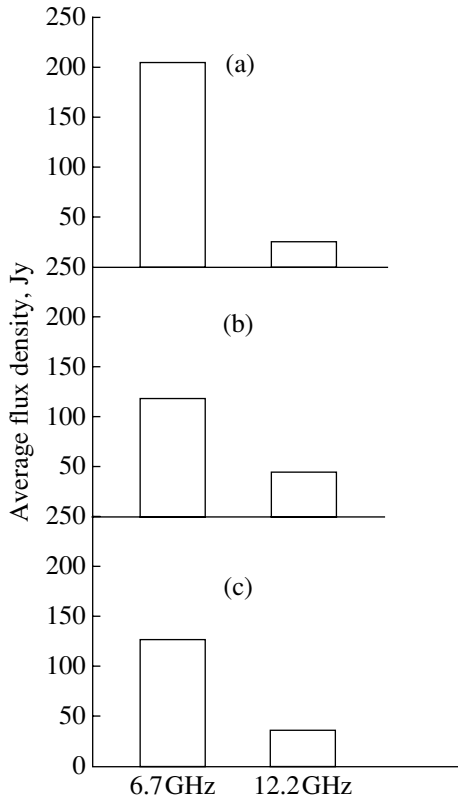
Fig. 4. Distribution of average flux densities of features in the $5_1 - 6_0 A^+$ (6.7 GHz) and $2_0 - 3_{-1} E$ (12 GHz) lines for 67 sources: (a) pairs with a stronger feature in the $5_1 - 6_0 A^+$ (6.7 GHz) line; (b) pairs with a weaker feature in the $5_1 - 6_0 A^+$ (6.7 GHz) line; (c) same, but for sources with single features.

(12 GHz) lines and can attempt to classify the remaining 64 sources, represented in [7] by a single $2_0 - 3_{-1} E$ (12 GHz) line and its $5_1 - 6_0 A^+$ (6.7 GHz) counterpart. If a single feature of the $5_1 - 6_0 A^+$ (6.7 GHz) line dominates in the spectrum, it is of course strongest, but this does not tell us anything about whether this feature belongs to the subsets of stronger or weaker $5_1 - 6_0 A^+$ (6.7 GHz) lines we have distinguished. To determine this, we compare their parameters with those obtained for the line pairs. Figure 4c shows the distribution of average flux densities in the $5_1 - 6_0 A^+$ (6.7 GHz) and $2_0 - 3_{-1} E$ (12 GHz) lines for 62 sources with single features. The ratio of the average flux densities in these lines is 3.6. We have not included two sources in this distribution: G24.33+0.14, for which $S_{12.2} > S_{6.7}$, and G9.62+0.20. This latter object certainly belongs to the group of sources with a stronger $5_1 - 6_0 A^+$ (6.7 GHz) line, since the flux density in the $5_1 - 6_0 A^+$ (6.7 GHz) line exceeds that in the $2_0 - 3_{-1} E$ (12 GHz) line by a factor of 28, and the $5_1 - 6_0 A^+$ (6.7 GHz) line itself is very bright, $S_{6.7} = 5090$ Jy

(this is the brightest 6.7-GHz maser [7]). Including this line increases the average 6.7-GHz flux by 62%, while including the counterpart $2_0 - 3_{-1} E$ (12 GHz) line ($S_{12.2} = 128$ Jy) increases the average 12.2-GHz flux by only 6%.

Figure 6c presents a histogram of the ratios of the flux densities in the $5_1 - 6_0 A^+$ (6.7 GHz) and $2_0 - 3_{-1} E$ (12 GHz) lines for 62 sources with single $5_1 - 6_0 A^+$ (6.7 GHz) lines [7], and Figure 8a shows the flux density in the $5_1 - 6_0 A^+$ (6.7 GHz) line as a function of the flux density in the $2_0 - 3_{-1} E$ (12 GHz) line for these 62 sources. The approximation parameters and correlation coefficients corresponding to the thick straight line are listed in Table 3.

An analysis of Figs. 4c, 6c, and 8a shows that there are definitely both "stronger" and "weaker" $5_1 - 6_0 A^+$ (6.7 GHz) lines in the sources with single $5_1 - 6_0 A^+$ (6.7 GHz) lines. They have average parameters intermediate between the values obtained for the stronger and weaker features of the $5_1 - 6_0 A^+$ (6.7 GHz) line and their counterparts in the $2_0 - 3_{-1} E$ (12 GHz) line.

The thin line in Fig. 8a shows the linear approximation from Fig. 7b for the weak features (No. 2 in Table 3), and the thin dashed line is the linear approximation from Fig. 7a for strong features (No. 1 in Table 3). Twenty single-line sources located below the thick line can be classified as sources with a weak $5_1 - 6_0 A^+$ (6.7 GHz) line. Precisely these 20 sources are among the 50 sources in the histogram in Fig. 6c for which the ratios of the flux densities in the $5_1 - 6_0 A^+$ (6.7 GHz) and $2_0 - 3_{-1} E$ (12 GHz) lines lie between one and ten. Ten sources above the thin dashed line in Fig. 8a can be classified as strong. At the same time, there are four sources below this line with very large (> 20) ratios of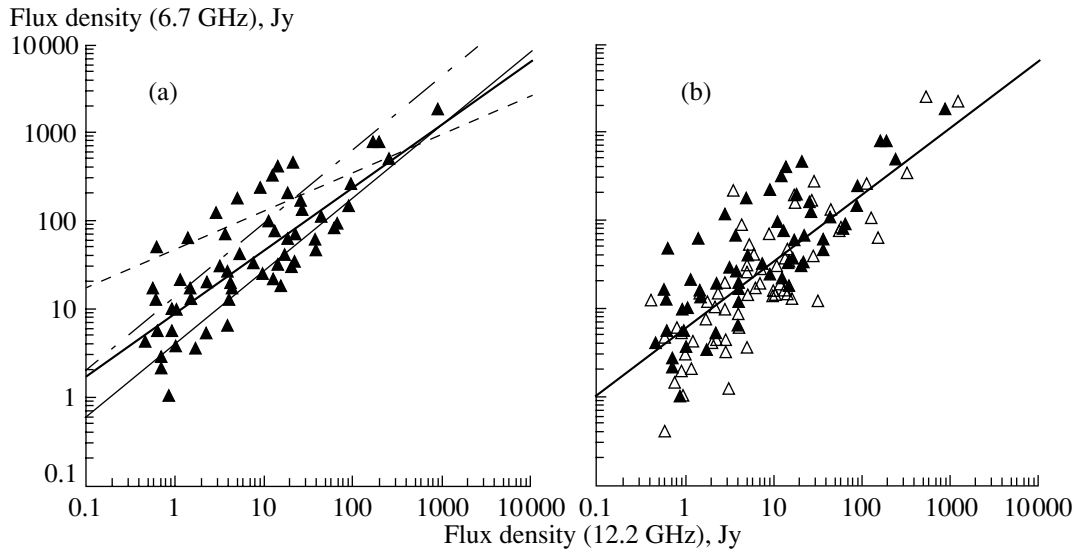 the flux densities in the $5_1 - 6_0 A^+$ (6.7 GHz) and $2_0 - 3_{-1} E$ (12 GHz) lines that can also be classified as strong. Taking these sources into account, we shifted the approximating straight line for weak $5_1 - 6_0 A^+$ (6.7 GHz) and $2_0 - 3_{-1} E$ (12 GHz) pairs from Fig. 7b upward (dot–dashed line). According to this shift, three sources that fell in the interval between the dot–dashed line (weak features) and thin dashed line (strong features) may be weak. Indeed, their ratios of the flux densities in the $5_1 - 6_0 A^+$ (6.7 GHz) and $2_0 - 3_{-1} E$ (12 GHz) lines are about five.

Figure 8b presents sources with weak features in the $5_1 - 6_0 A^+$ (6.7 GHz) line and all sources with single lines (approximation parameters are listed in Table 3). We can see that all the sources with single lines fit the dependence in Fig. 8a well; i.e., it is likely that the single-line sources include primarily sources whose characteristics are closer to those of sources with weak $5_1 - 6_0 A^+$ (6.7 GHz) lines.
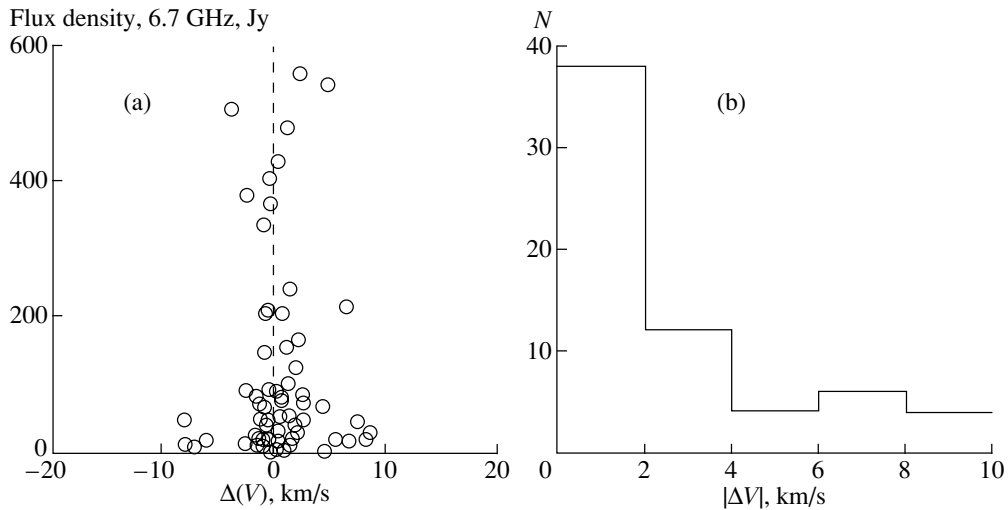
Fig. 5. (a) Distribution of the difference in velocities of the stronger and weaker features in the $5_1 - 6_0A^+$ (6.7 GHz) line in the spectra of 67 sources. (b) Distribution of the magnitude of the velocity difference for the stronger and weaker features in the $5_1 - 6_0A^+$ (6.7 GHz) line in the spectra of 67 sources.

The list of 27 weak and 14 strong sources we have classified in the sample of 64 single-line objects [7] is given in Table 4.

4. INTERPRETATION OF THE OBSERVED RELATIVE ENHANCEMENT OF THE $2_0 - 3_{-1}E$ (12 GHz) LINE

Thus, we have confirmed relative strengthening of the $2_0 - 3_{-1}E$ (12 GHz) line for a large, statistically reliable sample, accompanied by a relative weakening of the brightest class II $5_1 - 6_0A^+$ (6.7 GHz) maser line.

We can give the following explanation for this effect.

First, it must be explained by a specialized source model. Existing models for class II maser sources do not predict the observed ratio of the $5_1 - 6_0A^+$ (6.7 GHz) and $2_0 - 3_{-1}E$ (12 GHz) line intensities: for any intensity of the $5_1 - 6_0A^+$ (6.7 GHz) line, the intensity of the $2_0 - 3_{-1}E$ (12 GHz) line increases and decreases only simultaneously (in phase) with the increase or decrease in the $5_1 - 6_0A^+$ (6.7 GHz) line intensity.

However, according to unpublished data of V.I. Slysh (private communication), there exist models in which the optimal conditions for maximum intensities of the $5_1 - 6_0A^+$ (6.7 GHz) and $2_0 - 3_{-1}E$ (12 GHz) lines are different. We run into a contradiction if we try to explain the observed effect using these models: the set of $5_1 - 6_0A^+$ (6.7 GHz) line intensities are for maser condensations belonging to a separate molecular cloud, so the $5_1 - 6_0A^+$ (6.7 GHz) and $2_0 - 3_{-1}E$ (12 GHz) line intensity

ratios should have a random character no matter how they are modeled. We can imagine a situation in which we could model the observed peculiarity in the $5_1 - 6_0A^+$ (6.7 GHz) and $2_0 - 3_{-1}E$ (12 GHz)
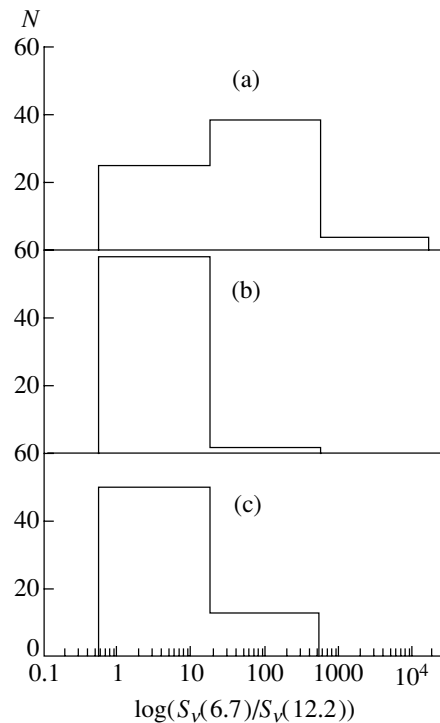
Fig. 6. Distributions of the ratios of the flux densities in the $5_1 - 6_0A^+$ (6.7 GHz) and $2_0 - 3_{-1}E$ (12 GHz) lines for 67 sources: (a) pairs with a stronger $5_1 - 6_0A^+$ (6.7 GHz) line; (b) pairs with a weaker $5_1 - 6_0A^+$ (6.7 GHz) line; (c) sources with single features.

Table 4. 27 weak and 14 strong (boldface) single lines from [7], selected with the dependences for the line pairs

Source	Flux density in the $5_1 - 6_0 A^+$ (6.7 GHz) line, Jy	Flux density in the $2_0 - 3_{-1} E$ (12.2 GHz) line, Jy	Ratio $S_\nu(6.7)/S_\nu(12.2)$
196.45 − 1.68	61	1.35	45
284.35 − 0.42	2.1	0.7	3
305.37 + 0.19	1	0.85	1
309.92 + 0.48	780	156	5
318.95 − 0.20	780	180	4
323.46 − 0.08	22	12.2	2
328.24 − 0.55	400	13	31
329.03 − 0.21	200	17.5	11
333.16 − 0.10	6.3	3.8	2
336.43 − 0.26	46	36	1
336.83 + 0.02	16	1.4	11
337.61 − 0.06	21	12	2
337.71 − 0.05	145	84	2
337.92 − 0.46	47	0.55	85
338.08 + 0.01	18	14.7	1
338.93 − 0.06	12	3.8	3
339.88 − 1.26	1820	850	2
340.05 − 0.24	42	16	3
344.23 − 0.57	118	2.7	43
344.42 + 0.05	16	0.55	29
345.00 − 0.22	448	20	22
345.01 + 1.80	31	14	2
345.50 + 0.35	174	4.7	37
347.58 + 0.21	2.7	0.7	4
348.70 − 1.04	60	34.5	2
351.77 − 0.54	225	8.5	26
9.62 + 0.20	5090	180	28
12.89 + 0.49	93	62	1
12.91 − 0.26	317	11.5	28
15.03 − 0.68	39	17	2
16.59 − 0.05	21	1.1	19
19.61 − 0.12	3.6	1	4
24.33 + 0.14	10.8	20	1
27.36-0.16	29	20	1
28.15 + 0.00	34	21	2
30.78 + 0.23	24	9	3
31.28 + 0.06	81	59	1
33.13 − 0.09	12.4	0.6	21
43.17 − 0.00	3.4	1.7	2
45.47 + 0.05	5.3	2.2	2
49.49 − 0.37	33	21	2

Flux density (6.7 GHz), Jy
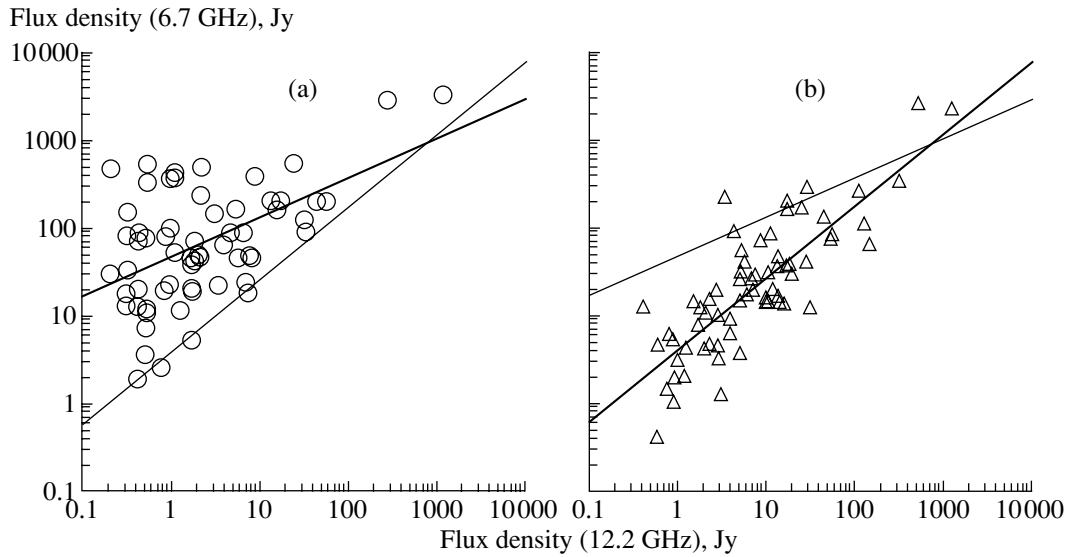
Fig. 7. Dependence between the flux densities (on a logarithmic scale) in the $5_1 - 6_0 A^+$ (6.7 GHz) and $2_0 - 3_{-1} E$ (12 GHz) lines: (a) pairs with a stronger $5_1 - 6_0 A^+$ (6.7 GHz) line (thick line: approximation No. 1 in Table 3; thin line: approximation No. 2); (b) pairs with a weaker $5_1 - 6_0 A^+$ (6.7 GHz) line (thick line: approximation No. 2 in Table 3; thin line: approximation No. 1).

Flux density (6.7 GHz), Jy

Fig. 8. Dependence between the flux densities (on a logarithmic scale) in the $5_1 - 6_0 A^+$ (6.7 GHz) and $2_0 - 3_{-1} E$ (12 GHz) lines: (a) 64 sources represented in [7] by a single feature in the $5_1 - 6_0 A^+$ (6.7 GHz) line (thick line: approximation No. 3 in Table 3; thin line: approximation No. 2; dashed line: approximation No. 1); (b) same sources with a single feature in this line together with the sources of Fig. 7b with weak features in this line (thick line: approximation No. 4).

line intensity ratios in a single molecular cloud with two maser condensations, but it is hardly possible to model the same type of intensity ratios in pairs of $5_1 - 6_0 A^+$ (6.7 GHz) and $2_0 - 3_{-1} E$ (12 GHz) lines for 67 molecular clouds. The different physical conditions in the maser condensations should yield a spectrum of intensity ratios and smear out the effect

observed in a single source if we consider a large sample of objects.

The concept of "strong" or "weak" line features we use in this paper has a relative character. Such strong or weak lines should be observed in the spectra of separate molecular clouds in different numbers that are unpredictable beforehand, and in any pattern, for example, two, three, or more strong lines in one

spectrum, only weak lines in another spectrum, etc. In this case, the $5_1 - 6_0 A^+$ (6.7 GHz) and $2_0 - 3_{-1} E$ (12 GHz) line-intensity ratio should be arbitrary and only sometimes take the form we see in the spectra of W48 and the other 66 sources. At the same time, the effect we observe is qualitative: in each of the 67 sources, we see one strong and one weak feature of the $5_1 - 6_0 A^+$ (6.7 GHz) line, and always with the same consequence for the $2_0 - 3_{-1} E$ (12 GHz) line intensity.

Another possible explanation for this effect is the action of some factor in the individual maser condensations.

Since we are dealing with different sources, the effect in question cannot be connected with the pumping source (which is the same for both strong and weak $5_1 - 6_0 A^+$ (6.7 GHz) lines within a molecular cloud), physical conditions in the maser condensations (as shown in the arguments above), or the orientation of the masers relative to the observer, since all these factors vary from source to source, and the effect should be smoothed if we consider a large sample of sources.

It is possible that, in some condensations, some special factor acts, which forms the methanol level populations in such a way that the $5_1 - 6_0 A^+$ transition (6.7 GHz) captures all the population resources of other levels responsible for the formation of remaining class II maser lines in the condensation. This factor must act in addition to the pumping and operate only inside the condensation itself. Under the action of this factor, the $5_1 - 6_0 A^+$ (6.7 GHz) line is strengthened while other transitions are weakened. If this factor does not operate, external pumping will strengthen all class II transitions in a fairly proportional manner. We suggest that this factor can operate only under certain specific conditions, which play the role of a threshold effect for the maser pumping (in contrast to the physical conditions, which should change continuously from one condensation to another).

We will call this additional enhancement of the $5_1 - 6_0 A^+$ (6.7 GHz) line maser transpumping. We can see in Figs. 7a and 7b that the behavior of the line intensity ratios does indeed have a threshold character [an absence of strong sources below the approximation line for weak sources (Fig. 7a) and an absence of weak sources above the approximation line for strong sources (Fig. 7b)], in support of the concept of transpumping.

Thus, maser sources in which both pumping and transpumping operate can be considered methanol masers of subclass IIa, and sources in which pumping alone operates, methanol masers of subclass IIb.

Taking into account the 64 sources with single lines (Figs. 8a, 8b), we conclude that the majority of class II masers belong to subclass IIb, which display normal pumping, whereas the transpumping phenomenon is encountered less frequently.

5. DISCUSSION

Let us discuss again the following points. We observe the same pattern in 67 sources without exception. There is a strong feature in the $5_1 - 6_0 A^+$ (6.7 GHz) line and its counterpart in the $2_0 - 3_{-1} E$ (12 GHz) line; if there is a weak feature in the $5_1 - 6_0 A^+$ (6.7 GHz) line, its counterpart in the $2_0 - 3_{-1} E$ (12 GHz) line is stronger than the $2_0 - 3_{-1} E$ (12 GHz) line corresponding to the stronger $5_1 - 6_0 A^+$ (6.7 GHz) line.

Thus, two facts are established:

(1) the relative strengthening of the $2_0 - 3_{-1} E$ (12 GHz) line in a pair with a weaker $5_1 - 6_0 A^+$ (6.7 GHz) line,

(2) the systematic presence of this phenomenon in a large sample of sources. The relative strengthening of the $2_0 - 3_{-1} E$ (12 GHz) line can essentially be explained in a specialized source model or by invoking some specific factor; however, explaining the systematic recurrence of the observed effect is much more difficult.

The more important point is probably not that the $2_0 - 3_{-1} E$ (12 GHz) line is relatively enhanced, but that there is a common pattern for its intensity variations relative to the $5_1 - 6_0 A^+$ (6.7 GHz) line intensity in many sources.

This similarity in the variations of the ratio of the $5_1 - 6_0 A^+$ (6.7 GHz) and $2_0 - 3_{-1} E$ (12 GHz) lines may indicate that these transitions are subject to different pumping conditions, which are affected by outside influences, rather than signify changes in the internal physical conditions in the condensations (which can vary chaotically from one condensation to another) or a specific, transpumping-like factor that affects the level populations.

When interpreting the relative strengthening of the $2_0 - 3_{-1} E$ (12 GHz) line, we assumed (as is appropriate for class II methanol masers) that a common, external source of pumping operates in each molecular cloud and is identical for all maser condensations.

A change in the external pumping conditions could indicate, for example, that the condensations are not equidistant from the pumping source. Thus, if the condensations within one molecular cloud have a common, external pumping source, we can derive information about the distance of a condensation from the pumping source, tracing a very subtle effect.

In other words, the weaker $5_1 - 6_0 A^+$ (6.7 GHz) line is weaker because it forms in a condensation that is more distant from the pumping source, if we suppose that the external pumping source acts more strongly on the first condensation, giving rise to more intense emission in the $5_1 - 6_0 A^+$ (6.7 GHz) line in this condensation. The existence of such a situation in 67 sources could imply that one condensation is always closer to the pumping source than the other.

This is possible if these condensations are orbiting, for example, if they are ice planets revolving around young massive stars or protostars [25]. In this case, changes of the pumping conditions will be discrete, since each condensation is in its distinct own orbit.

One possible objection to this is that, if we observed changes in the intensities of the $5_1 - 6_0 A^+$ (6.7 GHz) and $2_0 - 3_{-1} E$ (12 GHz) lines consistent with the predictions of current models [namely, as the $5_1 - 6_0 A^+$ (6.7 GHz) line weakens, the $2_0 - 3_{-1} E$ (12 GHz) line also weakens], we could also attribute changes in the pumping conditions to the arrangement of the condensations in orbits at various distances from the pumping source. However, in this case, we would not observe stepwise behavior in the line-intensity-ratio variations and would not distinguish changes in the pumping conditions from changes of the physical conditions in the condensations.

The planetary model can easily explain the fact that, in all the spectra, there is always a stronger and a weaker feature of the maser radiating in the $5_1 - 6_0 A^+$ (6.7 GHz) line, with a tendency for discrete changes of the line intensity ratio from one condensation to another. However, in a planetary model for W48, the ultracompact H II region G35.20−1.74 is located too far from the maser condensations to be considered a source of pumping for material in planetary atmospheres. According to the considerations of [25], ice planets should be located at the edges of H II regions; therefore, the most probable pumping source for such planets in W48 is the object MIR1.

Thus, we confirm for a large sample of sources the plausibility of the hypothesis [25] that studies of maser emission can be used as a method for detecting distant planets.

If this hypothesis is correct, the table of Caswell *et al.* [7] represents a list of at least 67 distant planetary systems.

6. CONCLUSIONS

(1) We have studied the methanol-line spectrum in two maser condensations at velocities $\sim$41 and $\sim$45 km/s in the star-forming region W48.

(2) The intensity of the $2_0 - 3_{-1} E$ (12 GHz) line is anticorrelated with the intensity of the $5_1 - 6_0 A^+$ (6.7 GHz) line: the intensity of the $5_1 - 6_0 A^+$ (6.7 GHz) line is greater at $\sim$41 km/s than at $\sim$45 km/s, whereas the opposite is true of $2_0 - 3_{-1} E$ (12 GHz) line.

(3) All remaining class II maser lines in this source demonstrate the same behavior as the $2_0 - 3_{-1} E$ (12 GHz) line.

(4) This contradicts current concepts about maser line intensities in various methanol transitions; model calculations indicate that the intensities of all class II lines should vary in phase.

(5) This effect is confirmed for a large homogeneous sample of 67 sources.

(6) We suggest possible explanations for the observed behavior, including the concept of trans-pumping of the methanol level populations in the maser condensations.

(7) The pattern for the $2_0 - 3_{-1} E$ (12 GHz) line intensity variations relative to intensity variations for the $5_1 - 6_0 A^+$ (6.7 GHz) line is the same in all 67 sources studied, and may indicate that the weaker condensation is located further from the pumping source.

(8) This suggests that, in all 67 sources, there is a condensation that is less distant from the pumping source and another that is more distant; this may be true because the individual condensations are ice planets revolving in different orbits around massive stars or protostars.

ACKNOWLEDGMENTS

REFERENCES

1. E. Churchwell, C. M. Wamsley, and R. Cesaroni, Astron. Astrophys., Suppl. Ser. **83**, 119 (1990).
2. C. E. Woodward, H. L. Helfer, and J. L. Pipher, Astron. Astrophys. **147**, 84 (1985).
3. P. Hofner and E. Churchwell, Astron. Astrophys., Suppl. Ser. **120**, 283 (1996).
4. J. R. Forster and J. L. Caswell, Astron. Astrophys. **213**, 339 (1989).

5. T. Jenness, P. F. Scott, and R. Padman, Mon. Not. R. Astron. Soc. **276**, 1024 (1995).

6. P. Persi, M. Felli, P. O. Lagage, *et al.*, Astron. Astrophys. **327**, 299 (1997).

7. J. L. Caswell, R. A. Vaile, S. P. Ellingsen, and R. P. Norris, Mon. Not. R. Astron. Soc. **274**, 1126 (1995).

8. R. P. Norris, J. L. Caswell, F. F. Gardner, and K. J. Wellington, Astrophys. J. Lett. **321**, L159 (1987).

9. K. M. Menten, Astrophys. J. Lett. **380**, L75 (1991).

10. I. E. Val'tts, A. M. Dzura, S. V. Kalenskiĭ, *et al.*, Astron. Astrophys. **294**, 825 (1995).

11. V. I. Slysh, S. V. Kalenskiĭ, and I. E. Val'tts, Astrophys. J. **442**, 668 (1995).

12. V. I. Slysh, S. V. Kalenskiĭ, I. E. Val'tts, *et al.*, Astrophys. J., Suppl. Ser. **123**, 515 (1995).

13. V. I. Slysh, S. V. Kalenskiĭ, and I. E. Val'tts, Astron. Zh. **79**, 54 (2002) [Astron. Rep. **46**, 49 (2002)].

14. R. Bachiller, K. M. Menten, J. Gomez-Gonzalez, and A. Barcia, Astron. Astrophys., Suppl. Ser. **240**, 116 (1990).

15. A. D. Haschick and W. A. Baan, Astrophys. J. **339**, 949 (1989).

16. I. E. Val'tts, A. M. Dzyura, S. V. Kalenskiĭ, *et al.*, Astron. Zh. **72**, 22 (1995) [Astron. Rep. **39**, 18 (1995)].

17. J. L. Caswell and R. F. Haynes, Aust. J. Phys. **417**, 36 (1983).

18. V. Migenes, S. Horiuchi, V. I. Slysh, *et al.*, Astrophys. J., Suppl. Ser. **123**, 487 (1999).

19. G. M. Larionov, I. E. Val'tts, A. Winnberg, *et al.*, Astron. Astrophys., Suppl. Ser. **139**, 257 (1999).

20. I. E. Val'tts, S. P. Ellingsen, V. I. Slysh, *et al.*, Mon. Not. R. Astron. Soc. **310**, 1077 (1999).

21. A. M. Sobolev and S. Deguchi, Astron. Astrophys. **291**, 569 (1994).

22. A. M. Sobolev, D. M. Cragg, and P. D. Godfrey, Mon. Not. R. Astron. Soc. **288**, L39 (1997).

23. A. M. Sobolev, D. M. Cragg, and P. D. Godfrey, Astron. Astrophys. **394**, 211 (1997).

24. V. Minier, R. S. Booth, and J. E. Conway, Astron. Astrophys. **362**, 1093 (2000).

25. V. I. Slysh, I. E. Val'tts, S. V. Kalenskiĭ, and G. M. Larionov, Astron. Zh. **76**, 751 (1999) [Astron. Rep. **43**, 657 (1999)].

Translated by G. Rudnitskiĭ

Polarization of Individual Pulses of Radio Pulsars at the Low Frequencies 40, 60, and 103 MHz

S. A. Suleimanova and V. D. Pugachev

Pushchino Radio Astronomy Observatory, Lebedev Physical Institute, Russian Academy of Sciences,
Leninskiĭ pr. 53, Moscow, 117924 Russia
Received July 20, 2001

Abstract—Measurements of the linear polarization of individual pulses at 40, 60, and 103 MHz are presented for ten pulsars. The degree and position angle of a linear polarization were measured with a temporal resolution of 1–7 ms, and the longitudinal distributions of these parameters were constructed for each pulsar at one or more of these frequencies. These are the first such measurements for pulsars B0031 − 07, B0320 + 39, B0628 − 28, and B2217 + 47. Apart from B0628 − 28, all the pulsars are characterized by the simultaneous presence of orthogonal polarization modes in at least one component of the integral profile. The secondary polarization mode increases at frequencies ≤ 100 MHz for pulsars whose integrated pulses contain pairs of conal components (B0031 − 07, B0329 + 54, B0834 + 06, B1133 + 16, B2020 + 28). This is manifested both as an expansion of the longitudinal range where the secondary polarization mode is observed and an increase in its contribution to the emission at a given longitude. New data confirming the dependence of the linear polarization of individual pulses on the intensity and mode of the pulsar emission have been obtained. © 2002 MAIK "Nauka/Interperiodica".

1. INTRODUCTION

There are two main features distinguishing pulsars from other astronomical sources: the periodic character of their radio emission and its strong linear polarization. Polarization measurements very rapidly occupied an important place in studies of the emission mechanism and magnetic-field configuration of these objects. Such measurements have been conducted primarily for integrated (averaged) pulses, obtained by summing hundreds or thousands of individual pulses accumulated with the period of the pulsar's rotation. The vast majority of polarization measurements have been carried out at frequencies above 400 MHz; this is due to the fact that the largest fully steerable radio telescopes operate mainly at decimeter wavelengths, where long accumulation of the pulsar signal makes it possible to acquire high signal-to-noise ratios even for pulsars with low radio fluxes. Such decimeter-wavelength measurements have shown that the most typical degrees of linear polarization for the integrated pulses are 20–40% [1], in some cases reaching 100%. The degrees of linear polarization for most pulsars are an order of magnitude greater than their degrees of circular polarization. The degree of linear polarization in integrated pulses decreases with increasing frequency, with the depolarization index varying over a wide range from −0.13 to −1.35 [2, 3]. For approximately one-third of the 30 pulsars in the list of [3], this index

changes abruptly at the so-called critical frequency [2]. The behavior of the degree and angle of the linear polarization as functions of longitude along the integrated pulse can be very complex, with their values experiencing rapid (and, usually, simultaneous) changes.

The behavior of the polarization of integrated pulses described above must be explained by the properties of individual pulses. The first polarization measurements of individual pulses were conducted for several of the most powerful pulsars at 610 MHz [4] and 2295 MHz [5] in 1969, soon after the discovery of these pulsars. At approximately the same time, the DKR-1000 radio telescope at the Radio Astronomy Station of the Lebedev Physical Institute in Pushchino was used to carry out polarization measurements of pulsars at very low frequencies. Observations of B1133 + 16 at 63 MHz in 1970 revealed rapid (pulse to pulse), discrete changes in the position angle by 90° [6]. The first compilation of polarization measurements for individual pulses for a relatively large set of 12 pulsars at frequencies between 110 and 450 MHz was published in 1975 [7]. These data showed that pulse-to-pulse position-angle jumps by 90° occurred at a fixed longitude between neighboring components of the individual pulses (i.e., subpulses) and at the fronts of the subpulses themselves. These results demonstrated that the presence of two components with orthogonal polarization position angles is very typical for pulsar

emission. According to the terminology introduced in [8], these components are called orthogonal polarization modes. Theoretically, in the "rotating-vector" model of [9], the polarization position angle should rotate monotonically with longitude along a pulse, with the rate of rotation depending on the orientation of the rotational axis and the magnetic-dipole axis relative to the line of sight. In fact, this is observed only rarely, when the intensity of one mode is considerably greater than the other in the entire emission window. In general, the behavior of the position angle along a pulse for most pulsars is governed by the statistics of the distributions of the two orthogonal polarization modes, with their weight being proportional to their intensity. The more intense polarization mode is usually called the primary mode, and the other, the secondary mode. When the energies of the two modes are equal at some pulse phase, there is a local minimum in the degree of linear polarization, with the position angle experiencing random jumps by 90° [10]. For this reason, integrated position-angle profiles are usually not suitable for precise estimation of the rate of rotation of the position angle with longitude, or ultimately for studies of the magnetic-field geometry in the pulsar emission region.

Measurements for individual pulses make it possible to resolve the two polarization modes in the position-angle distribution and reveal the character of variations in the intensity, angle, and degree of polarization of each mode as functions of longitude. Another necessary piece of information for understanding the pulsar emission mechanism is the frequency dependence of the polarization parameters of individual pulses over a fairly broad frequency range.

The most complete information about the polarization properties of individual pulses has been accumulated at frequencies around 400 MHz. The results of observations of 18 pulsars using the Arecibo telescope at 430 MHz were first presented in the form of longitude distributions of the polarization degree and angle in [11]. This type of presentation, involving hundreds of measurements, has proven to be very illustrative. Results for 11 pulsars at 1404 MHz [12] and four pulsars at 800 MHz [13] were presented in the same form. Observations at 400 MHz (9 pulsars), 1400 MHz (4 pulsars), 285 MHz (2 pulsars), and 147 MHz (1 pulsar) were presented in review [7] in another form: the polarizations of individual pulses were described using the degree of linear polarization averaged over longitude. (We shall use both of these approaches in our low-frequency analysis.) There have been a number of other studies dealing with the properties of individual pulses of specific pulsars: B0823 + 26, B0834 + 06, and B2303 + 30 at 430 MHz [14]; B2020 + 28 at 430 MHz [8]; B0823 +

26 at 1404 MHz [15]; and B0329 + 54 at 408 MHz [16] and 1700 MHz [17].

As is apparent from the above summary of previous publications, information on the polarization of individual pulses at frequencies below 400 MHz (and, especially, below 100 MHz) was almost absent before the early 1990s. By saying "almost" absent, we have in mind the fact that the first results of low-frequency polarization measurements of individual pulses were published soon after the discovery of several pulsars. These were carried out at the Radio Astronomy Station of the Lebedev Physical Institute for five pulsars known at that time—B0329 + 54, B0628 − 28, B0943 + 10, B1133 + 16, and B2217 + 47—using a 12-channel receiver. These observations were conducted at 63−105 MHz using the East−West arm of the DKR-1000 radio telescope with horizontal polarization. The detection of Faraday modulation of the pulsar-signal amplitude at the output of the multichannel receiver made it possible to estimate the degree of linear polarization for the strongest pulses, as well as the average magnetic field in the interstellar medium in the direction of the pulsar. A typical example of the earliest data on polarization measurements below 100 MHz is presented in [18]. The next important step in studies of the polarization of individual pulses at the Lebedev Physical Institute was regular pulsar observations using the DKR-1000 antenna combined with a supplementary "polarization antenna" with vertical polarization, beginning in 1972. All four polarization parameters were measured at 86 MHz. A series of such observations of the three pulsars B0834 + 06, B0950 + 08, and B1133 + 16 [19] showed that the linear polarization of their individual pulses increased with decreasing observing frequency.

A significant drawback of these meter-wavelength measurements was their low time resolution, since they were characterized by a time constant of about 10 ms and a bandwidth of 70 kHz. Essentially, each individual pulse or resolved component (subpulse) was represented by a single reading at its intensity maximum.

A polarization survey carried out starting in the early 1990s using the Large Phased Array (LPA) and the DKR-1000 radio telescope of the Lebedev Physical Institute and new multichannel receivers with narrow bandwidths and small time constants made it possible to obtain results whose accuracy, time resolution, and form of representation were comparable with those for data available at higher frequencies. The present paper describes the results of this survey, carried out for a fairly representative set of ten pulsars at 103, 60, and 40 MHz. Several pulsars in our list have also been studied at higher frequencies, enabling us to trace the evolution of the polarization properties

Observational parameters of individual pulses

Pulsar B	Period P, s	Frequency, MHz	DM, pc/cm^3	Channel band-width, kHz	Delay in the band, ms	Reso lution, ms	TC, ms	RM, rad/m^2	P_F, MHz	Receiver bandwidth, MHz
$0031-07$	0.9429	103.13	10.89	20	1.7	5.184	3	9.8	1.84	1.28
		60.75		20	8.1	5.184	3		0.37	1.28
$0320+39$	3.0321	103.13	25.8	20	3.8	5.184	3	67.0	0.31	1.28
$0329+54$	0.7145	102.75	26.776	20	4.1	1.024	1	-63.7	0.31	0.64
$0628-28$	1.2444	103.13	34.36	20	5.3	8.704	3	46.19	0.40	1.28
		60.93		5	6.4	10.112	3		0.09	0.16
		39.99		5	21.8	8.704	3		0.025	0.16
$0834+06$	1.2737	112.68	12.858	20	1.5	0.922	1	23.6	1.02	2.56
		60.75		20	9.6	5.12	3		0.16	0.64
		39.89		1.25	2.0	3.072	3		0.045	0.12
$0943+10$	1.0977	103.13	15.35	20	2.4	6.912	3	15.0	1.20	1.28
		40.40		5	9.7	6.912	3		0.075	0.16
$1133+16$	1.1879	59.73	4.8471	20	3.6	6.912	3	3.9	0.70	1.28
		39.98		20	12.2	6.912	3		0.21	0.64
$2016+28$	0.5579	102.75	14.176	20	2.2	2.304	1	-34.6	0.57	0.64
$2020+28$	0.3434	102.75	24.62	20	3.8	1.28	1	-74.7	0.27	0.32
$2217+47$	0.5384	103.13	43.54	20	6.7	4.864	3	-35.3	0.52	0.64

of individual pulses as functions of frequency from decimeter to meter wavelengths.

2. METHOD OF POLARIZATION MEASUREMENTS

The pulsar polarization measurements described here were obtained primarily in 1990−1995. The observations were conducted at the Pushchino Radio Astronomy Observatory of the Lebedev Physical Institute using the LPA (103 MHz) and DKR-1000 (60 and 40 MHz) radio telescopes. The degree and angle of the linear polarization of individual pulses were determined based on measurements of the amplitude and initial phase of the Faraday modulation of the intensity at the output of the multichannel radiometer. The method used is described in [20, 21]. Several different radiometers with total frequency bandwidths 128×20 kHz, 32×5 kHz, and 128×1.25 kHz were used for the pulsar observations. Measurements were carried out for each temporal count exceeding the 5σ intensity threshold, where σ is the rms scatter of the noise beyond the pulse. The maximum rms error for a single reading of the degree of linear polarization (DLP) is $\pm10-15\%$, while that for a single reading of the position angle (PA) is about $\pm15°$, depending on

the depth of the spectrum modulation. Increasing the number of modulation periods within the radiometer bandwidth also increases the reliability of the measurements. The shape of the integrated pulse for each pulsar was obtained by summing the signals within the total received bandwidth, compensating for the dispersion frequency delay relative to the first (highest frequency) radiometer channel.

The observation parameters for each pulsar are presented in the table: the pulse period, frequency of the first channel, dispersion measure (DM), bandwidth for each channel, total dispersion delay over a single channel, time resolution, receiver time constant, rotation measure of the interstellar medium in the direction of pulsar (RM), Faraday period P_F for the given RM and frequency, and total received bandwidth.

Note that this measurement method imposes certain limitations on the number of pulsars that can be studied. The selection criterion were not only based on a high intensity of individual pulses but also on the pulsar having a suitable rotation measure. The lower bound on the RM was specified by the requirement that the period P_F be sufficiently short to fit within the total bandwidth of the multichannel radiometer at
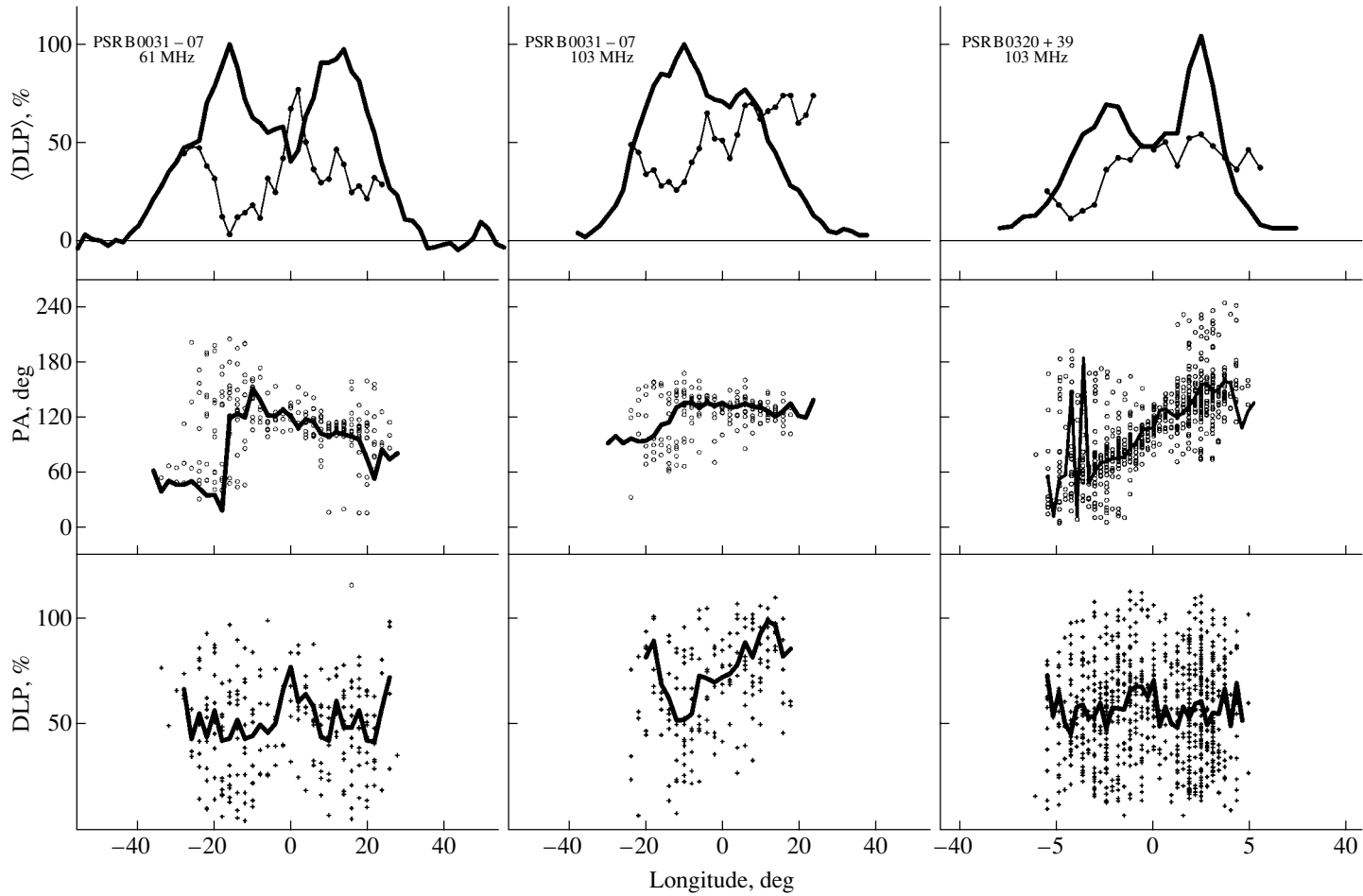
Fig. 1. Longitudinal distribution of the position angles and degrees of linear polarization of individual pulses for B0031 − 07 (at 61 and 103 MHz) and B0320 + 39 (at 103 MHz); 360° corresponds to the pulsar period. The integrated profile of the degree of linear polarization ⟨DLP⟩ (curve with dots) is shown in the top panels together with the integrated profile of the pulse intensity. The integrated PA profile is shown in the middle panels together with the distribution of the position angles for individual pulses. Finally, a curve describing the mean DLP values for individual pulses is presented in the bottom panels.

least once. On the other hand, the upper bound was determined by the requirement that this period be sufficiently long to involve several channels.

3. DESCRIPTION AND DISCUSSION OF OBSERVATIONAL RESULTS

We present our results for ten pulsars at one or more frequencies in 21 distributions of the degree and position angle of the linear polarization in pulse longitude (phase); 360° corresponds to the pulsar period (Figs. 1−9). The integrated characteristics of the pulsars are also presented. The integrated profiles of the degree of linear polarization ($\langle$DLP$\rangle$, %) are shown together with the integrated profiles of the pulse intensity in the top panels. The integrated PA profile is shown in the middle panels, together with the distribution of the PAs of individual pulses. Finally, the mean DLP values of individual pulses are shown in the bottom panels. We emphasize here the difference between the curve of the mean DLP values and the integrated DLP profile. The integrated profiles of the DLP and PA are the result of analyzing a single integrated pulse, derived by summing hundreds of individual pulses. The integrated pulse often possesses lower polarization, due to fluctuations of the PA from pulse to pulse. The degree of depolarization depends on the relationship between the energies of the orthogonal polarization modes at a given longitude. On the other hand, the mean DLP curve results from averaging the entire array of DLP values for individual pulses at a given longitude, taken with equal weights. Therefore, this quantity does not depend on the intensity and pulse-to-pulse PA fluctuations at a given longitude. Physically, it is this quantity that characterizes the instantaneous degree of linear polarization of the emission.

We comment on the distributions for each pulsar below.

__0031 − 07__ (Fig. 1). The single-component profile of the pulsar intensity at frequencies ≥ 400 MHz is rapidly transformed into a two-component profile as the frequency decreases. At 60 MHz, it has two well-resolved components with approximately equal amplitudes but different polarization properties. We can clearly see two orthogonal modes in the PA distribution for the first component, resulting in a broad minimum of the DLP in the integrated profile at the corresponding longitudes; the lowest polarizations were 5% at 61 MHz and 15% at 103 MHz. The presence of 90° jumps in the PA and a low DLP (about 5%) for the integrated pulse at 410 and 1665 MHz [7, 22] lead us to identify this pulse with the first component of the integrated profile at 103 and 60 MHz. The second component initially possesses a high DLP (at 103 MHz), which decreases with frequency. The
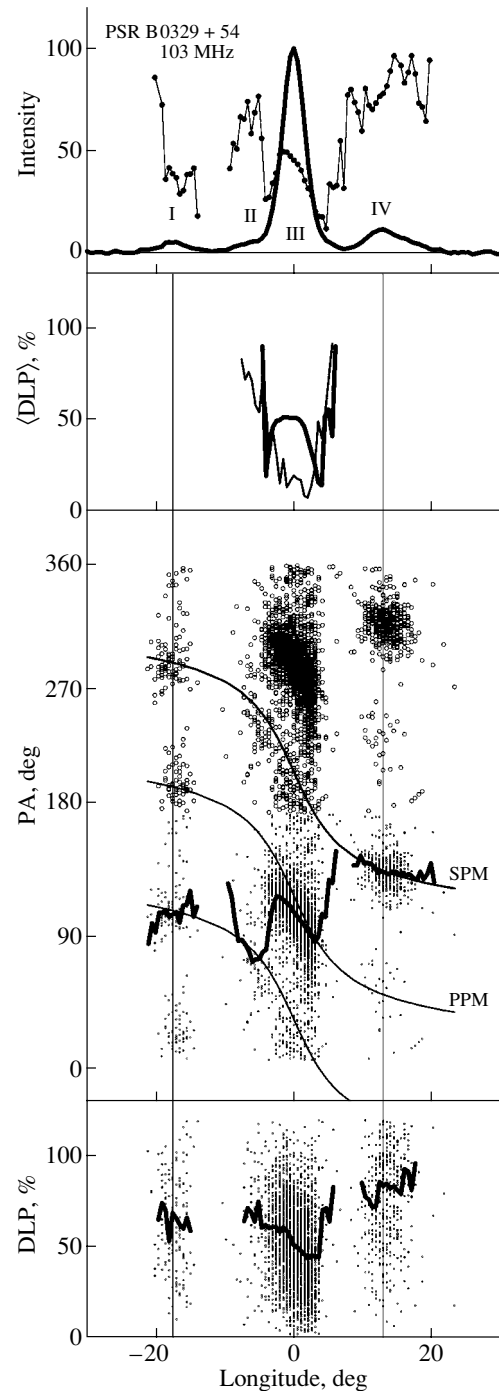
Fig. 2. Same as Fig. 1 for pulsar B0329 + 54 (at 103 MHz). The angles in the PA distribution for individual pulses are plotted twice, shifted by 180°. The three thin curves describe the expected behavior of the angles in the rotating-vector model [9, 16] for the two orthogonal polarization modes. The vertical lines show the positions of the two "conal" components. The integrated DLP profiles obtained after averaging individual pulses with amplitudes above 50σ (strong pulses, thick curve) and below 10σ (weak pulses, thin curve) are shown in the second panel from the top. PPM and SPM refer to the primary and secondary polarization modes, respectively.

depolarization is associated with a more important role for the secondary polarization mode (SPM) in the emission of the second component, resulting in a monotonic decrease in the DLP from 60% around the saddle to 30% in the trailing wing of the pulse.

It is known that subpulses of this pulsar drift toward earlier longitudes with one of three discrete rates [23]. The polarization measurements for the individual subpulses showed one or two PA jumps in each of them. Two-thirds of the jumps occur at the leading fronts, and are usually observed in subpulses whose intensity exceeds the average level. The weaker pulses are preferably associated fully with either the SPM (in the first component) or the primary polarization mode (PPM). The average polarization of subpulses without any PA jumps is 80% at all longitudes.

At 60 MHz, the PA jumps occur within subpulses with equal probability at their leading and trailing fronts. The appearance of PA jumps in the trailing wings of subpulses at 60 MHz results in depolarization of the trailing wing of the second component, which is not observed at 103 MHz.

0320 + 39 (Fig. 1). This pulsar is very interesting, because it belongs to a small group of pulsars with an anomalous direction for the longitude drift of their subpulses, from the leading to the trailing front of the emission window [24]. At 103 MHz, the drift of each subpulse is very regular and can be traced over 20 periods of the pulsar. The shape of the PA distribution shows that the bulk of the pulsar emission corresponds to one polarization mode. In the course of the subpulse drift, the PAs of the individual pulses form a continuous band from $30°$ to $150°$, which corresponds to a rotation rate of $12°$/deg. (From here on, we shall give the rotation per degree of longitude.) The SPM increases from the center to the edges of the integrated pulse; its influence is most substantial for the first component. The average polarization at the centers of individual subpulses is $60 \pm 3\%$ with an rms spread of 24% with $n = 104$, and does not exhibit any longitude dependence. Nevertheless, the DLPs of the integrated pulse are considerably different for the two components. The DLP appreciably decreases in the first part of the first component, to 16% on average; the minimum DLP is 5% at longitude $-3.5°$. Further, the DLP increases to 50% near the central longitude and retains this value in the second component. Our analysis shows that the SPM is observed at the longitude of the first component not only at the fronts but also at the centers of the subpulses (as in B0031 − 07). As a result, the two orthogonal polarization modes have equal intensities at the leading front and center of the first component. Moreover, the PA of the integrated pulse experiences a $90°$ jump here, implying that the SPM becomes dominant. The

PA jumps in individual subpulses along the same drift band can appear at both fronts of the subpulses with equal probability and are followed by depolarization at the corresponding longitudes. As a result, the DLP experiences longitude variations of $20−80\%$ in a typical pulse containing one to three subpulses. About half the total number of subpulses in the track display PA jumps (as for B0031 − 07).

There are no polarization measurements for this pulsar at high frequencies.

0329 + 54 (Fig. 2). Due to the high intensity of the radio emission in individual pulses and their complex shape and strong polarization, this pulsar is one of the most interesting for detailed studies throughout the radio band. The basic components of the integrated pulse are the central (core) and side (conal) components I and IV. One series of observations at 103 MHz includes 520 pulses, with the amplitudes of 70% of them usually exceeding the threshold. The signal-to-noise ratio for the strongest pulses often exceeds 50.

To more clearly illustrate the longitude distribution, the interval of PAs covering $180°$ is presented twice, shifted by $180°$. The three curves superposed on this distribution correspond to the two orthogonal polarization modes and describe the expected behavior of the PAs according to the rotating-vector model [9].

The parameters $\alpha = 51°$ (the angle between the rotational and magnetic-dipole axes) and $\beta = -4°$ (the minimum angle between the line of sight and the dipole axis) were obtained at 408 MHz [16]. For these values of α and β, this model describes the PA distribution at 103 MHz well. The presence of modes with orthogonal polarizations in the 103-MHz emission of B0329 + 54 can clearly be seen in the PA distribution: the values in each component form two groups separated by approximately $90°$. The intensity ratio for the two polarization modes can be estimated from the integrated polarization profile $\langle \text{DLP} \rangle$. The largest DLP values are observed in the second and fourth components, whereas the lowest values are observed in the first component and at the trailing front of the central component.

We especially emphasize that the intensity of the PPM in component IV is very weak, leading to the high DLP values of both the subpulses and the integrated pulse at this longitude. Comparison with data for 408 and 1700 MHz [16, 17] indicates a successive increase in the contribution of the SPM with decreasing frequency in the side components, especially in the fourth component. While at high frequencies the SPM is present only at the outward-directed edges of these components, at 103 MHz it completely determines the resulting angles in the integrated PA profiles for these components.
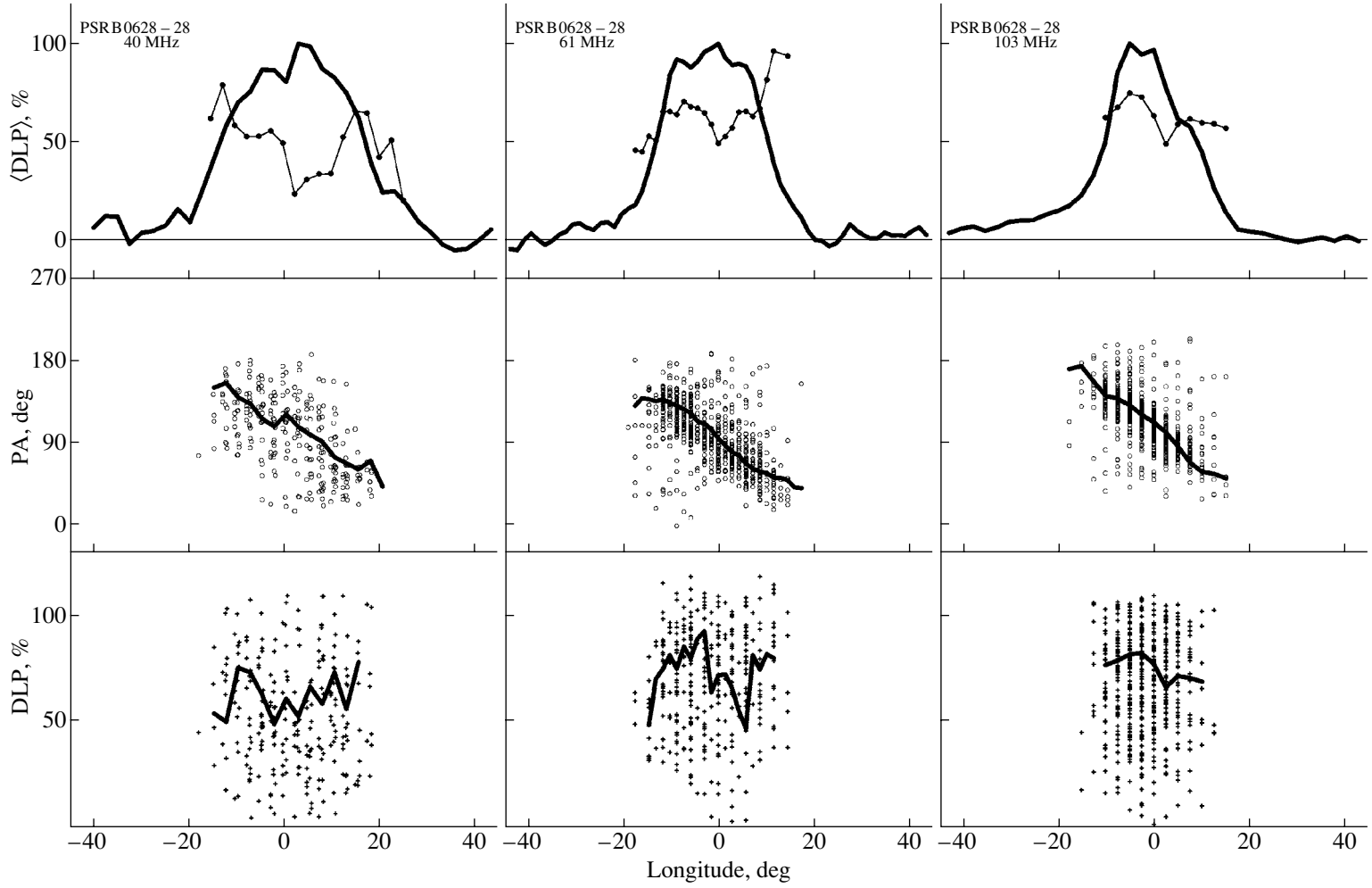
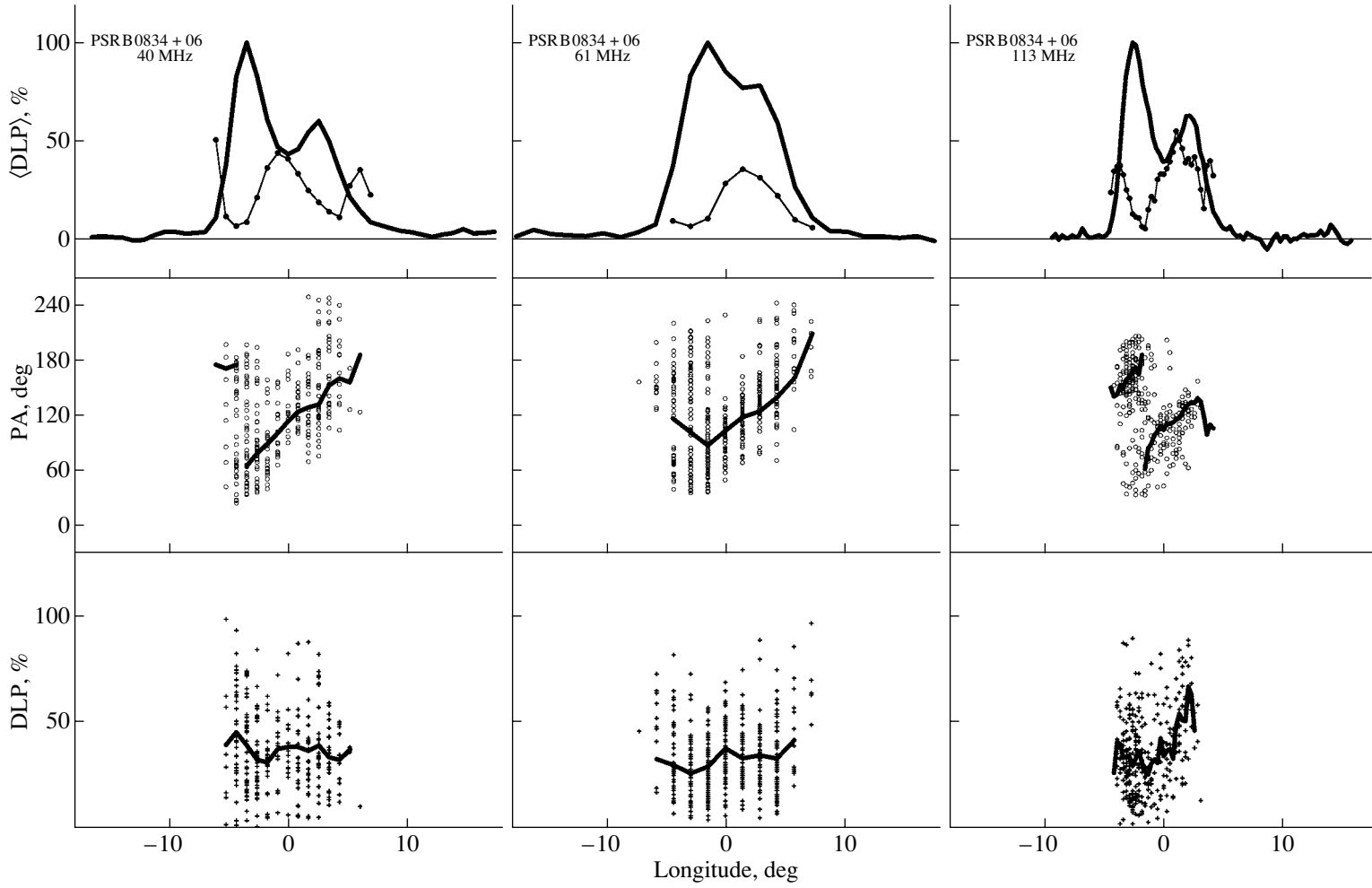**Fig. 3.** Same as Fig. 1 for pulsar B0628 − 28 (at 40, 61, 103 MHz).

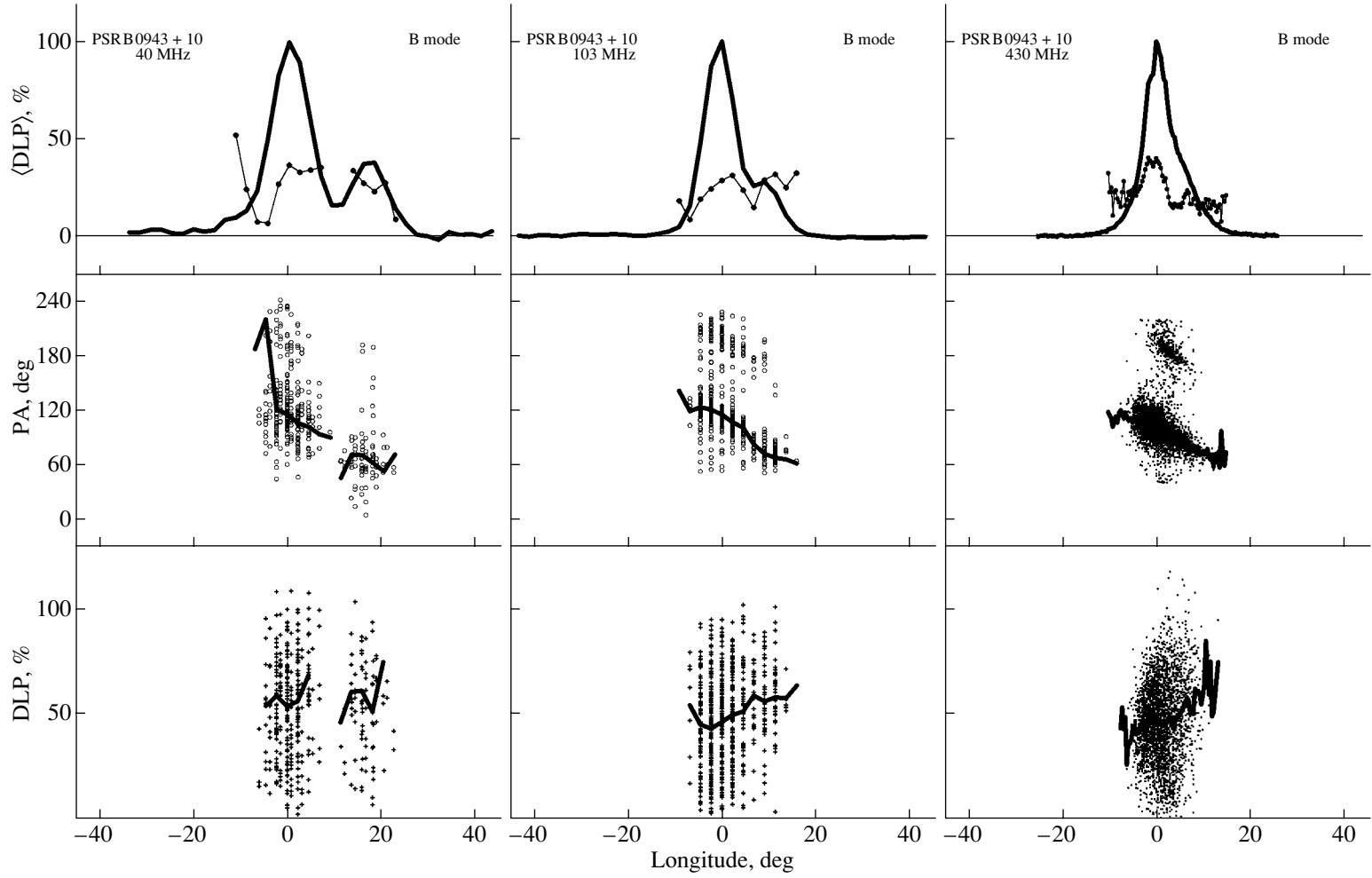**Fig. 4.** Same as Fig. 1 for pulsar B0834 + 06 (at 40, 61, 113 MHz).

Fig. 5. Same as Fig. 1 for pulsar B0943 + 10 in B mode (at 40, 103, 430 MHz).
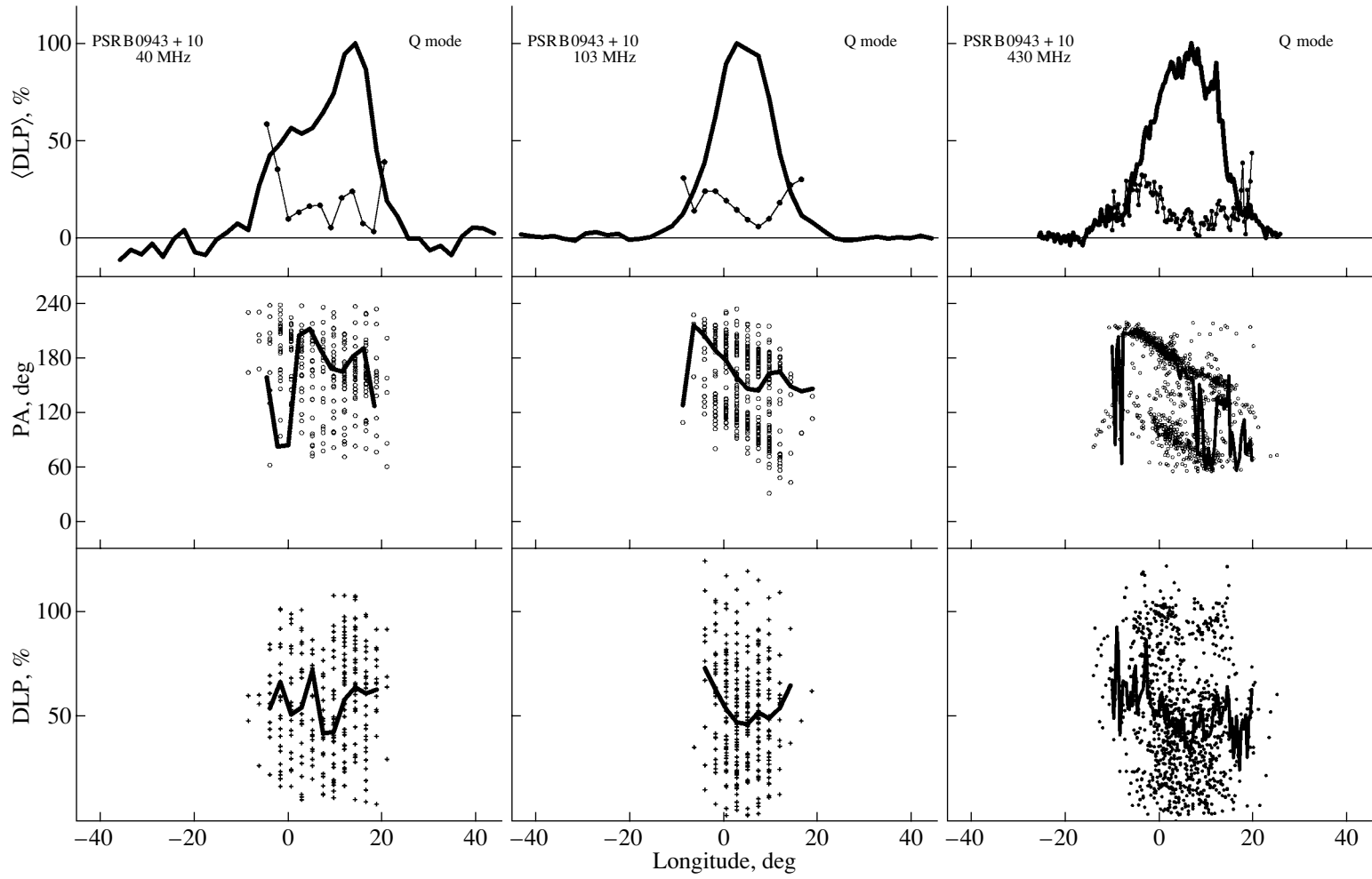
SULEIMANOVA, PUGACHEV

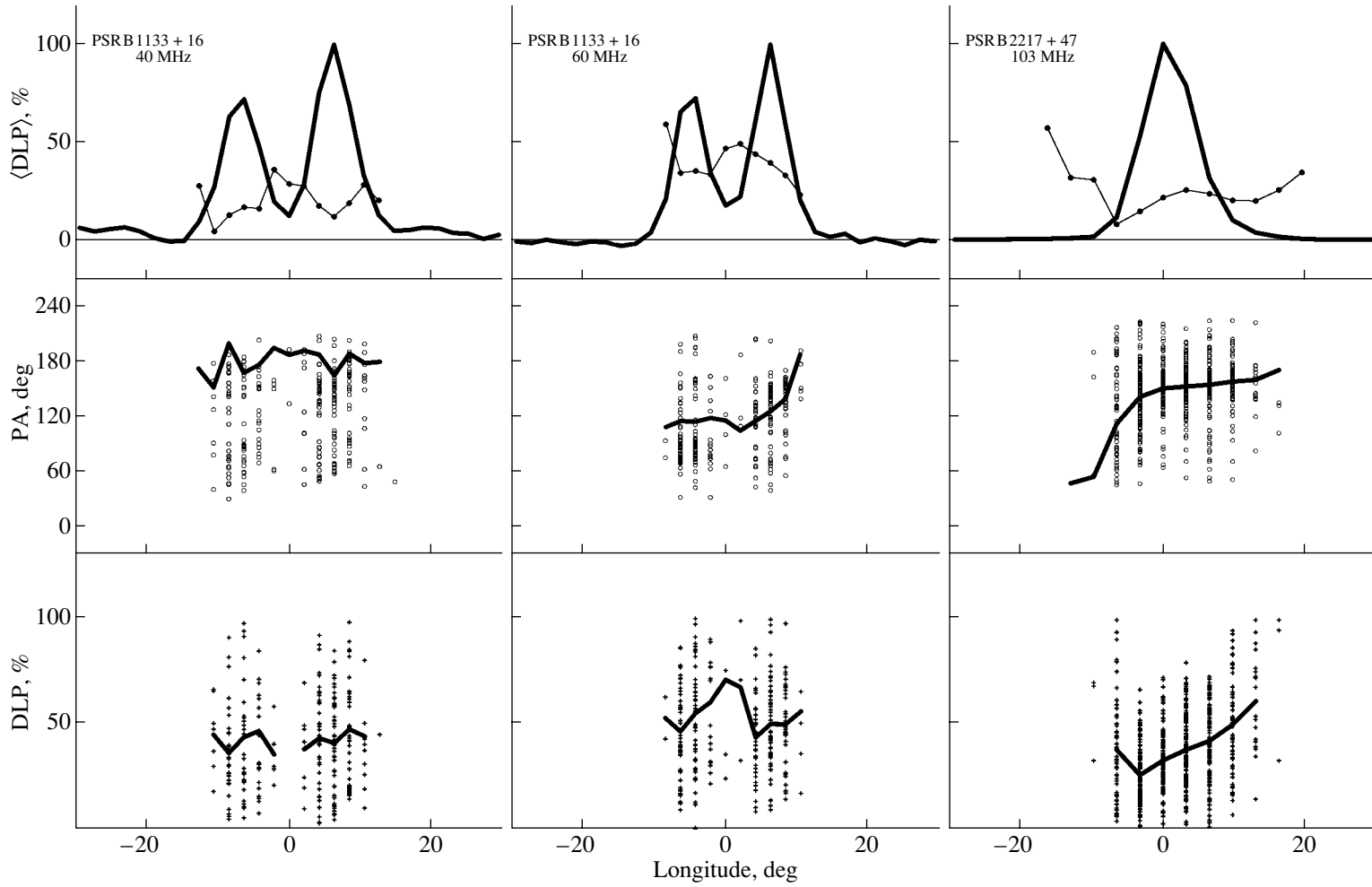**Fig. 6.** Same as Fig. 1 for pulsar B0943 + 10 in Q mode (at 40, 103, 430 MHz).

Fig. 7. Same as Fig. 1 for pulsars B1133 + 16 (at 40, 60 MHz) and B2217 + 28 (at 103 MHz).

We identified the polarization modes at different frequencies using the central part of the main component, where the PPM dominates at all radio frequencies, as well as the shape of the integrated PA profile at these frequencies. In general, the SPM dominates at 103 MHz in three of the four components. The transition of the dominance from one mode to the other is followed by a PA jump at the longitudes between the main component and neighboring components II and IV. Minima in the integrated DLP profile are observed at the same longitudes, $+4°$ and $-4°$ (Fig. 2).

To verify the hypothesis that there is a connection between the relative intensity of the emission and its polarization mode, we determined the polarization characteristics of the pulses corresponding to the central components in two groups, with high and low intensities. The integrated DLP profiles obtained by averaging individual pulses with amplitudes above 50σ (strong pulses) and below 10σ (weak pulses) are shown in Fig. 2 (second panel from the top) by the thick and thin curves, respectively. The PAs for the summed strong pulses are determined by the PPM. This mode dominates in the central parts of the strong pulses, so there is no depolarization of the integrated signal after an accumulation of individual pulses.

On the other hand, the longitude behavior of the PA for the summed weak pulses is determined by the SPM. The appreciable depolarization of the central component in the second group indicates that the weak pulses, as usual, correspond entirely to one of the two polarization modes, similar to the pulses of B0031 − 07. Because of the 90° PA fluctuations from pulse to pulse, the integrated pulse at a given longitude will be depolarized.

0628 − 28 (Fig. 3). An important characteristic property of this pulsar at 60 and 103 MHz is a high DLP for individual pulses throughout the emission window, often approaching 100%. The integrated profile cannot be resolved into separate components at the observed radio frequencies. The PA distributions at 60 and 103 MHz indicate an absence of the SPM in most of the emission window. This explains the high DLP of the integrated profile (whose value, $67 \pm 7\%$ [20, 21] almost coincides with the mean DLP of the individual pulses, 75%) and also the absence of jumps in the PA profile for the integrated pulse. On average, the DLP of individual pulses at 40 MHz was 25% less than at 103 MHz. This difference is probably the result of insufficient temporal resolution due to the considerable temporal dispersion for this pulsar. (The total dispersion delay at 40 MHz in a 5 kHz band is 22 ms, or 6.4°.) Since the rate of longitude variation of the PA is 4.1°/deg, averaging over the bandwidth of one channel can result in additional depolarization of the pulses. There are no measurements for individual

pulses at high frequencies; nevertheless, the continuously high DLP of integrated pulses (about 65%) up to 1000 MHz [2, 3] indicates an absence of the SPM in the pulsar emission over a broad frequency range.

0834 + 06 (Fig. 4). The characteristic shape of the PA and DLP distributions for the first component in the integrated profile of this pulsar are almost constant at all three frequencies—40, 60, and 113 MHz. The depolarization of the integrated pulse to 3% can be explained by the presence of the SPM mode in this longitude range. The polarization of the pulses at the longitude of the second component depends on frequency; the DLP at 113 MHz is rather high (about 50% or more) for both integrated and individual pulses. As the frequency decreases, the second minimum in the integrated DLP profile, observed in the trailing wing of the second component (at 113 MHz), extends to cover the central parts of this component as well. The DLP at the center of the second component at 40 and 60 MHz was half that at 113 MHz. The presence of the second minimum in the integrated DLP profile indicates that the contribution of the SPM to the pulsar emission increases with decreasing frequency. The rate of rotation of the PA along the integrated pulse is $11.5° \pm 1°$/deg of longitude. With regard to the measurements themselves, we note that this pulsar was observed at 40 MHz using a 128-channel radiometer with the extremely narrow channel bandwidth of 1.28 kHz, making it possible to minimize pulse broadening in the channel bandwidth. The LPA observations were carried out in 2001, after transition to the new operating frequency of 113 MHz.

0943 + 10 (Fig. 5, B-mode; Fig. 6, Q mode). Observations at the Pushchino Radio Astronomy Observatory at 62 and 102 MHz in 1980 demonstrated that the mean pulse of B0943 + 10 displays two substantially different shapes, or modes: a more intense two-component profile (B-mode) is replaced by a less intense one-component profile (Q-mode) approximately once each 30 min [25]. Observations of this pulsar at 430 MHz were initiated by S.A. Suleimanova and carried out in collaboration with Prof. Joanna Rankin (USA) in October 1992, at the Arecibo Observatory (Puerto Rico); these results are presented in detail in [26]. The distributions for this pulsar at 430 MHz and the low frequencies 40 and 103 MHz show that the two polarization modes possess different longitude distributions for the two modes of the mean profile. In the B-mode, the PPM dominates and covers the entire window, while the SPM is present only in the main component and the saddle region between the components. On the other hand, in the Q-mode, both polarization modes are observed over a wider longitude range, and the
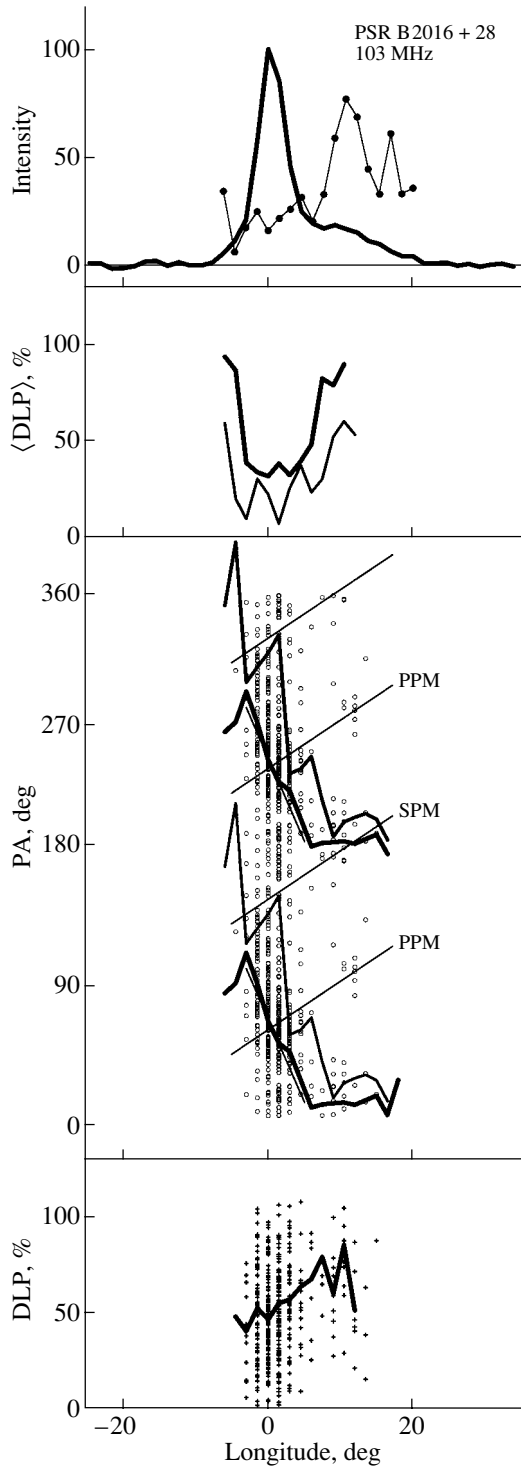
Fig. 8. Same as Fig. 2 for pulsar B2016 + 28 (at 103 MHz). The integrated DLP profiles after averaging individual pulses with amplitudes above 12σ (strong pulses, thick curve) and below 7σ (weak pulses, thin curve) are presented in the second panel from the top. The behavior of PAs with rotation rates of $-14°/\text{deg}$ and $3.5°/\text{deg}$ are schematically shown by the thin straight lines.
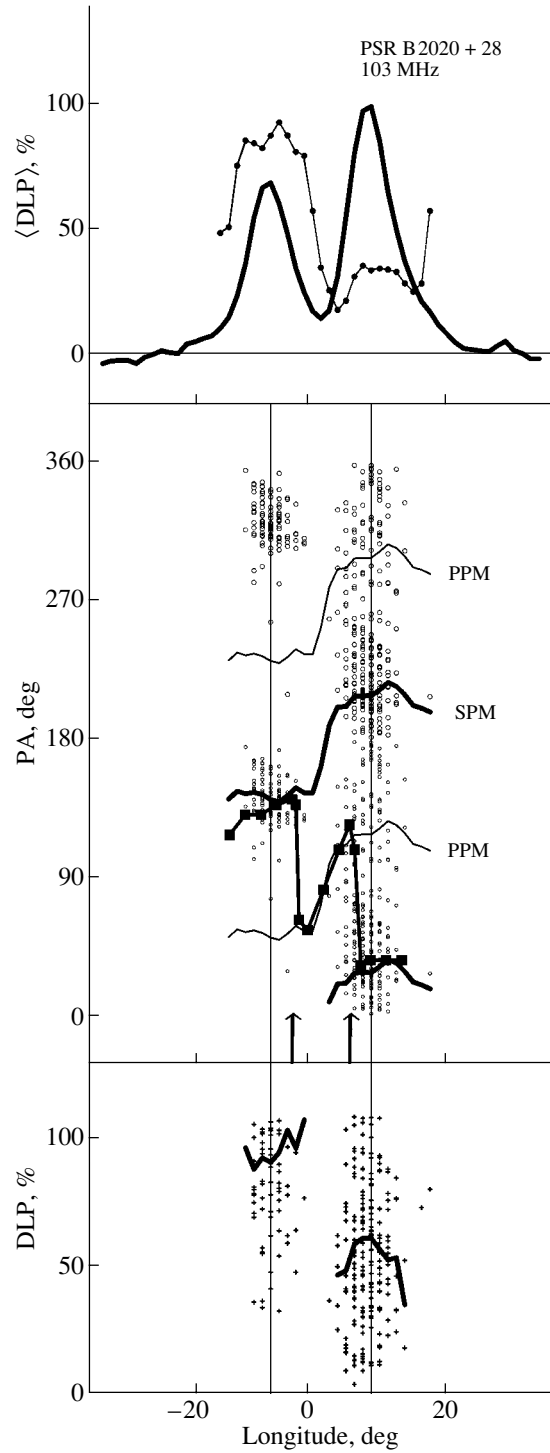
Fig. 9. Same as Fig. 1 for pulsar B2020 + 28 (at 103 MHz). The integrated PAs for individual pulses are plotted twice, shifted by 180°. PA profiles for 103 MHz (thick curve) and 1404 MHz [12] (curve with dark squares) are shown. The expected longitude behavior of the PA for the PPM at 103 MHz (thin curve) was obtained by shifting the observed profile by ±90°. The vertical lines denote the positions of the components at 103 and 1404 MHz.

SPM dominates in the pulsar emission. The ratios of the frequencies of occurrence of these modes are $N(\text{PPM}) : N(\text{SPM}) = 0.8 : 0.2$ in the B-mode and $0.4 : 0.6$ in the Q-mode. Therefore, a redistribution of energy between the two orthogonal polarization modes in the emission window occurs simultaneously with the change in the shape of the integrated pulse. The similarity of the distributions at 40, 103, and 430 MHz for each shape of the mean pulse suggests that the switching between the two discrete polarization states has a broad-band character.

The individual pulses of B0943 + 10 at 103 MHz contain one to four subpulses independent of the emission mode, but some differences are present in their polarizations.

B-mode. There is a jump of the PA by approximately 90° 5−10 ms from the subpulse center, followed by a short-term decrease in the DLP. A statistical analysis showed that 75% of the subpulses have one or two PA jumps, with jumps at the leading front occurring twice as often as at the trailing front and several times more often than at the center. The most typical value of the DLP of a subpulse at the longitude of a jump is 25%, with the DLP at other longitudes being about 70%. (This is also responsible for appreciable depolarization of the leading front of the integrated pulse.) The behavior of the PA along a pulse composed of several subpulses has a sawtooth character, due to the different senses of the jumps at the leading and trailing fronts of the subpulses. This is true because the central, most intense, parts of the subpulses correspond to the PPM mode, while the fronts correspond to the SPM.

Q-mode. The linear polarization in the subpulse center is about 70%, as in the B-mode. On the other hand, the typical DLP of the mean pulse in Q-mode is a factor of 2 smaller than that in the B-mode, due to the approximately equal probability of the presence of both polarization modes in the pulsar emission (Fig. 6). Moreover, 60% of PA jumps in the Q-mode occur between subpulses rather than inside them (while only 20% of jumps in the B-mode display this behavior). As a result, the intensities of the two orthogonal polarization modes are approximately equal and the polarization of the integrated pulses is small.

1133 + 16 (Fig. 7). The distributions for this pulsar were derived from simultaneous observations on February 27, 1991, at 40 and 60 MHz. The presence of two orthogonal polarization modes on this day is manifest especially clearly at 40 MHz, for each of the two pulse components. Comparison with observations of individual pulses at 410 MHz [7], 430 MHz [11], and 1404 MHz [12] demonstrates that the contribution of the SPM increases with decreasing frequency. This follows, first, from the fact that the

SPM is essentially absent at the longitude of the second component at 1404 MHz, in contrast to 40 and 60 MHz. Second, at low frequencies, the intensity of the orthogonal mode at the longitude of the first component becomes comparable with the intensity of the PPM. As a result, we detected a monotonic increase of the PA by approximately 90° in the transition from the first to the second component of the integrated pulse (which is observed at all higher frequencies and is completely determined by the PPM) in only half our observing sessions. In other cases, the PA in the first component was determined partially or completely by the SPM, as was the case on February 27, 1991, at 60 and 40 MHz (Fig. 7). Note that, at 410 MHz [7], only a quarter of the pulses are polarized with the orthogonal angles at the longitude of the first component.

2016 + 28 (Fig. 8). The integrated profile of the pulse intensity preserves its Π-shaped form over the broad range 10 500−200 MHz but rapidly becomes an extremely asymmetric two-component profile at 103 MHz [27]. Our 103 MHz observations show that, due to the absence of a preferred longitude for its subpulses, the second component resembles an extended trailing front of the main component.

The subpulse drift toward early longitudes, first discovered in 1969 [28], is expressed less clearly in B2016 + 28 than, for example, in B0031 − 07. The individual pulses include one of two subpulses. Because of the low intensity of the second component, the drift band at 103 MHz can be traced only at the longitudes of the first (or main) component over six to eight pulsar periods. After processing 400 pulses in each observing session, we could reliably distinguish no more than ten drift bands containing subpulses whose intensities were sufficient for polarization measurements. Essentially, the 103 MHz emission of B2016 + 28 represents a sequence of low-intensity pulses, with more powerful pulses at the longitude of the main component. (The amplitudes of 75% of the pulses are below the 7σ level, while about 10% of the strong pulses have amplitudes above 12σ).

We can distinguish two characteristic intervals with different rates of longitude variations in the integrated PA profile, shown by the thick curve in Fig. 8. These intervals are marked by the thin straight lines with inclinations of −14°/deg (at the longitude of the main component) and +3.5°/deg. (To more clearly represent the longitude distribution, a PA interval encompassing 180° is presented twice, shifted by 180°.) The line with a positive slope corresponds to the PA variations in weak pulses at longitudes covering both components. This is the rate of rotation of the PA in the integrated pulse at the high frequencies 410 MHz

[22], 430 MHz [11], and 1404 MHz [12]. It is reasonable to suppose that the rate of PA rotation with a longitude of $+3.5°/$deg is determined by geometric factors, in agreement with the rotating-vector model [9].

The presence of the two types of PA behavior provided a reason for studying the dependence of the polarization of pulses on their intensity in more detail. We have analyzed this dependence of the pulse polarization properties for two groups—weak pulses, with amplitudes $\leq 7\sigma$ and strong pulses with amplitudes $\geq 12\sigma$—based on data obtained over five observing sessions. Although the DLP of subpulses does not depend on their intensity, being equal, on average, to 60%, after summing the pulses, the DLP near the center of the integrated pulse at longitude $+1.5°$ was always lower for the first group (5–40%) than for the second group (45–70%). This difference was due less to the numbers of pulses contributing to the mean values for the each group than to the fact that 90° PA jumps between subpulses were more frequent for the weaker pulses. The PA variations in the second group were observed primarily within a subpulse, with the centers of strong subpulses almost always corresponding to the PPM. (A similar dependence of polarization state on pulse intensity was discussed above for B0031 − 07 and B0943 + 10.) We can clearly identify three minima in the integrated profile ⟨DLP⟩ for 311 pulses with amplitudes below 7σ, at longitudes $-3°$, $+1.5°$, and $+6°$ (thin curve in the second panel from the top in Fig. 8). After summing weak pulses, we can see the jump-like changes in the integrated PA profile at these longitudes, due to the presence of two polarization modes. The SPM determines the PA near the center of the main component and in the entire second component, while the PPM determines the PA at the fronts of the main component. The PA at the center and edges of the main component for the sum of the 30 strongest pulses ($\geq 12\sigma$) is opposite to that observed for the sum of weaker pulses. The observed rapid rotation of the PA through 120° is monotonic and is not followed by depolarization of the pulse; the DLP of the integrated pulse within the main component does not decrease below 35% (see thick curve in the second panel of Fig. 8).

2020 + 28 (Fig. 9). The mean pulse of this pulsar possesses a classical two-component shape but demonstrates an evident polarization asymmetry in the properties of its components. The DLP of the mean pulse ⟨DLP⟩ at 103 MHz drops sharply from 90% in the first component to 40% in the second component. There are also substantial differences in the DLP and PA distributions of individual pulses. The measured PAs for individual pulses are presented

in Fig. 9 twice, shifted by 180°. The PA profile for the mean pulse at 103 MHz is shown by the thick curve in this figure. A comparison of the PA distributions at low and high frequencies shows that, in general, the integrated PA profile at 103 MHz corresponds to the SPM (as defined at high frequencies). We will discuss this in more detail below. The expected longitude behavior of the PA for the PPM is shown in Fig. 9 by the thin curve shifted from the observed profile by $\pm 90°$.

Our conclusion that the contribution of the SPM to the emission of B2020 + 28 increases at low frequencies follows from a comparison of our own data and higher-frequency data. A detailed analysis of the mean and individual pulses at 430 MHz [8] showed that the SPM contributed 99% of the intensity of the first component. In contrast, only the PPM is present beginning from the second half of the trailing front of the first component and continuing in the saddle region. Both these modes can be seen in the second component, but 78% of the received emission is from the PPM. There are 90° PA jumps and an appreciable decrease in the DLP at longitudes of the mean pulse where one dominant mode of the pulsar emission is replaced by the other. At 430 MHz, this occurs in the region of the trailing front of the first component and both fronts of the second component. The same distributions for 1404 MHz [12] and 800 MHz [13] preserve the basic features described above for 430 MHz. To more clearly illustrate the PA profile for the mean pulse at 1404 MHz, it is shown in Fig. 9 by the thin curve with dark squares, with the positions of the component centers at this frequency indicated. The DLP of individual pulses at 103 MHz is slightly higher than at 430 MHz and higher frequencies, but the ratio of the DLPs of the two components remains almost the same: 90%/50% (at 103 MHz) and 80%/35% (at 430 MHz). On the other hand, the variations in the behavior of the PA are of considerably more interest, namely: (a) the rotation of the PA in the integrated profile at 103 MHz through approximately 75° at longitudes between the components is smooth, without any jumps, and follows the behavior of the PA at high frequencies for an individual polarization mode; (b) since the SPM dominates in the first component at all the above frequencies, the identification of the integrated PA profile at 103 MHz with this mode is beyond question. This means that the SPM at this frequency dominates in both components and in the saddle region of the second component. Another argument in favor of this suggestion is the absence of a minimum in the ⟨DLP⟩ profile for the mean pulse at 103 MHz (Fig. 9) at the trailing front of the first component, which is present at all higher frequencies due to the equal probabilities of manifestation of the two polarization modes.

The distribution of the PAs in individual pulses at 103 MHz confirms the absence of the PPM in the second half of the first component.

In our opinion, the change in the intensity ratio for the two polarization modes, increasing the contribution of the SPM at lower frequencies, occurs successively, starting from 1400 MHz. For example, a comparison of data at 1400 and 430 MHz [12] shows that, at the lower frequency, (a) the SPM is observed over a broader range in the first component so that the boundary for the transition to the PPM is shifted toward later longitudes, and (b) the SPM in the second component also becomes stronger and covers both the trailing front (as at 1400 MHz) and its center.

In the PA distribution at 103 MHz, the PPM is present only in the second component but is also substantially weaker than the SPM. Note that the same sort of successive increase in the contribution of the SPM at 103 MHz compared to 410 and 1700 MHz was observed for the conal components in the mean pulse of B0329 + 54. Moreover, the region where the SPM dominates for this pulsar also moves successively from the periphery to the center of the emission window with decreasing frequency [29].

2217 + 47 (Fig. 7). The 103 MHz emission of this pulsar represents a sequence of solitary subpulses, which display a small scatter around the central longitude. The polarization of B2217 + 47 at 103 MHz is characterized by the presence of the significant PA fluctuations from pulse to pulse. The PA along a subpulse varies stochastically within $\pm 30°$ about the mean value for each longitude. In addition, the PAs in about half the individual pulses experience abrupt changes by approximately 90° at longitudes between $-2°$ and $-6°$. The minimum DLPs are observed at these same longitudes. A second minimum in the DLP can be seen in some pulses at longitude $+6°$, associated with the rapid variation of the PA at the trailing front of the subpulses. For the strongest subpulses, fairly small PA variations through $\pm 15°$ are observed only within $\pm 2°$ of the subpulse center. At large distances from the center, the PA varies rapidly at a rate of approximately 10°/deg of longitude.

The integrated pulse is characterized by weak variations of the PA along the pulse, apart from the leading front. A rapid change in the PA is followed by a decrease in the DLP of the integrated pulse from 28% at its center to 8% at longitude $-6°$.

Although the PAs in B2217 + 47 do not clearly separate into two groups, the rapid change in the PA at the leading front of the integrated pulse implies the presence of two polarization modes. Due to the high intensity and polarization of most of the individual pulses, the scatter in the PA values cannot be attributed to instrumental errors. In our opinion, the large random component in the PA distribution represents the specific nature of the emission mechanism for this pulsar.

4. MAIN RESULTS OF A COMPARATIVE ANALYSIS FOR THE LOW- AND HIGH-FREQUENCY DATA

Longitude distributions of polarization parameters have been published for 20 pulsars [11−16], primarily for frequencies around 430 MHz. We have supplemented this list with data for four new pulsars— B0031 − 07, B0320 + 39, B0628 − 28, and B2217 + 47—which were not previously studied in detail at high frequencies. The results of our measurements of individual pulses for B0329 + 54 (at 103 MHz) and B0943 + 10 (at 103 and 430 MHz) are described in separate papers [29, 26]. The current paper presents measurements for ten pulsars at one or more frequencies (Figs. 1−9) in the form of 21 plots of the longitude distributions of the degree and position angle of the linear polarization. The following conclusions can be drawn from our analysis of these distributions and comparisons with higher frequency data.

(A) The presence of two orthogonal polarization modes in the emission is a universal property of pulsars, both at 40, 60, 103 MHz and at higher frequencies.

Comments. The increase in the DLP of integrated pulses from decimeter to meter wavelengths [20] could imply an absence of one of the orthogonal modes of the pulsar emission or substantial attenuation of one mode at frequencies ≤ 100 MHz. However, our measurements suggest that this is not the case (except for component IV in B0329 + 54).

(B) An increase in the contribution of the secondary polarization mode with decreasing frequency was observed in five of seven pulsars (B0031 − 07, B0329 + 54, B0834 + 06, B1133 + 16, and B2020 + 28) for which measurements at several frequencies were available. This is manifest as an extension of the longitude region where the SPM is observed, as well as an increase in its contribution to the emission at a given longitude. As a result, the planes of polarization in the integrated pulses at low frequencies for B0329 + 54 (conal components I and IV), B1133 + 16 (I), and B2020 + 28 (I, II) are completely determined by the SPM. There are no examples of a decrease in the intensity of the SPM toward lower radio frequencies.

Comments. Searches for a frequency dependence of the intensity ratio for the two orthogonal polarization modes were carried out earlier at high frequencies. For example, based on a comparison of the PA

distributions at 1404 and 430 MHz for eight pulsars with periods P > 0.3 s [12], it was concluded that the longitude range where the two orthogonal polarization modes are simultaneously present did not change with decreasing frequency in half the cases (including B0834 + 06 and B2020 + 28 from our list), while it increased with decreasing frequency in the other half of cases (including B1133 + 16 and B2016 + 28). Our measurements are in agreement with this conclusion. A new result of the low-frequency measurements is that the contribution of the SPM to the pulsar emission continues to increase at frequencies below 400 MHz. This is clearly seen in B0834 + 06 and B2020 + 28, which moved from the first to the second group at frequencies ≤ 113 MHz. The variation in the intensity ratio for the two orthogonal polarization modes implies differences in the frequency dependencies of their emission efficiencies. According to the theory of Cheng and Ruderman [30], this property is possessed by two waves with orthogonal polarizations—an ordinary (O-mode) and extraordinary (E-mode) wave. The O-mode is associated with longitudinal acceleration of charged particles due to the relative motion of the charges during their bunching. On the other hand, the E-mode is associated with the transverse acceleration of the bunches during their motion outwards from the stellar surface, along curved magnetic field lines. The E-mode dominates at the edges of pulses, whereas the O-mode dominates in their central regions. In addition, on a given magnetic-field line, the frequency of the O-mode, associated with bunching radiation, decreases with increasing distance from the stellar surface as $\omega_b \sim r^{-3/2}$, while the frequency of the E-mode, associated with curvature radiation, decreases with increasing distance as $\omega_c \sim r^{-1/2}$ (i.e., appreciably more slowly). The power emitted by a bunch at a given distance r is redistributed between the wave modes in proportion to their frequencies [30]. Therefore, curvature radiation begins to dominate in the outer regions of the pulsar magnetosphere. The model proposed in [30] can explain the increasing contribution of the SPM at low frequencies if the SPM is identified with the E-mode, i.e., with the curvature radiation. It is interesting that this both decreases the DLP at longitudes of the integrated pulse where the intensities of the SPM and PPM become comparable and increases the DLP when the SPM becomes the dominant mode for this component. The first case takes place in B0031 − 07 (II), B0834 + 06 (II), and B1133 + 16 (I), whereas the second case occurs in B0329 + 54 (IV).

The measurements at frequencies ≤ 100 MHz impose a constraint on alternative mechanisms for the pulsar emission (see, for example, [31]): they must explain the relative increase in the contribution of the SPM at low frequencies. Since this effect was detected in our study for five pulsars with two-component profiles or pairs of components (B0329 + 54), it corresponds primarily to the conal components of the emission region.

(C) The degree of linear polarization displays considerable longitude variations. It is substantially higher in components where one of the polarization modes dominates, while the second is weak or absent: for example, in B0031 − 07 (II, 103), B0329 + 54 (IV), B0628 − 28, and B2020 + 28 (I). Lower polarizations of subpulses are observed in components in which both polarization modes are present (i.e., two groups of PAs differing by 90° are clearly seen in the PA distribution), such as B0031 − 07 (I, 103), B0329 + 54 (III), and B2020 + 28 (II).

Comment. Such a correlation can also be seen for most pulsars at high frequencies, and was interpreted in [12] as confirmation of the suggestion that, at any given time, the pulsar emission represents an incoherent superposition of two components (modes) with orthogonal polarizations [30]. Fluctuations of the relative intensities of these components determine which of the two corresponding position angles will be observed. If the intensities are roughly equal, the polarization angles separate into two groups with equal probabilities, so that the received emission is depolarized.

(D) In general, the linear polarizations of individual pulses increase at low frequencies, but at a smaller rate than for the integrated pulses. Since the polarization properties of neighboring components of a mean pulse differ considerably in some cases, we analyzed the frequency dependence of the DLPs of individual pulses for each component separately, as for a separate emission region. (For example, in B0329 + 54, the linear polarizations of individual pulses between 103 and 430 MHz are constant for component I, increase by 20% for component II, and increase by 40% for component IV.) In about half the cases, the DLP increases at low frequencies, in accordance with the power-law exponent $n \cong -0.3$. There are no appreciable changes within 40−430(1400) MHz in the other half of the cases.

(E) The polarization properties of subpulses drifting in the normal (B0031 − 07) and anomalous (B0320 + 39) directions were analyzed. The observed properties of subpulses do not display substantial variations with changing drift rate and direction. This independence of the drift direction supports the idea that this direction is determined by geometric factors rather than by the emission mechanism [24].

(F) The polarization properties of the subpulses for several pulsars depend on their intensity. For example, the centers of strong subpulses for B0031 − 07, B0329 + 54, B0943 + 10, and B2016 + 28 at longitudes where two polarization modes are present

correspond to the dominant mode, while the fronts of subpulses correspond to alternative mode. When the intensity of the pulses decreases, the transition between the polarization modes usually occurs between neighboring subpulses rather than at the fronts.

Comment. The transition from one polarization mode to the other from the pulse (subpulse) center to its edges is in agreement with the model of Cheng and Ruderman [30], which was applied to explain PA jumps at the edges of subpulses at high frequencies [7]. Our measurements suggest that this phenomenon has a broad-band character.

(G) In the "mode-switching" pulsar B0943+10, the redistribution of energy between the orthogonal modes in the entire emission window occurs simultaneously with changes in the shape of mean pulse and also possesses a broad-band character. This effect is described in more detail in [26].

5. ACKNOWLEDGMENTS

REFERENCES

1. A. G. Lyne, F. G. Smith, and D. A. Graham, Mon. Not. R. Astron. Soc. **153**, 337 (1971).
2. R. N. Manchester, J. H. Taylor, and G. R. Huguenin, Astrophys. J. Lett. **179**, L7 (1973).
3. D. Morris, D. A. Graham, and W. Sieber, Astron. Astrophys. **100**, 107 (1981).
4. R. R. Clark and F. G. Smith, Nature **221**, 724 (1969).
5. R. D. Ekers and A. T. Moffet, Astrophys. J. Lett. **158**, L1 (1969).
6. Yu. P. Shitov, Astron. Zh. **49**, 470 (1972) [Sov. Astron. **16**, 383 (1972)].
7. R. N. Manchester, J. H. Taylor, and C. R. Huguenin, Astrophys. J. **196**, 83 (1975).
8. J. M. Cordes, J. M. Rankin, and D. C. Backer, Astrophys. J. **223**, 961 (1978).
9. V. Radhakrishnan and D. J. Cook, Astrophys. Lett. **3**, 225 (1969).
10. M. M. McKinon and D. R. Stinebring, Astron. Soc. Pac. Conf. Ser. **105**, 483 (1996).
11. D. C. Backer and J. M. Rankin, Astrophys. J., Suppl. Ser. **42**, 143 (1980).
12. D. R. Stinebring, J. M. Cordes, J. M. Rankin, *et al.*, Astrophys. J., Suppl. Ser. **55**, 247 (1984).
13. D. R. Stinebring, J. M. Cordes, J. M. Rankin, *et al.*, Astrophys. J., Suppl. Ser. **55**, 279 (1984).
14. J. M. Rankin, D. B. Campbell, and D. C. Backer, Astrophys. J. **188**, 609 (1974).
15. J. A. Gil, J. K. Snakowski, and D. R. Stinebring, Astron. Astrophys. **242**, 119 (1991).
16. J. A. Gil and A. G. Lyne, Mon. Not. R. Astron. Soc. **276**, L55 (1995).
17. N. Bartel, D. Morris, W. Sieber, and T. H. Hankins, Astrophys. J. **258**, 776 (1982).
18. V. V. Vitkevich and Yu. P. Shitov, Nature **226**, 1235 (1970).
19. Yu. I. Alekseev and S. A. Suleĭmanova, Astron. Zh. **54**, 323 (1977) [Sov. Astron. **21**, 180 (1977)].
20. S. A. Suleĭmanova, Yu. V. Volodin, and Yu. P. Shitov, Astron. Zh. **65**, 349 (1988) [Sov. Astron. **32**, 177 (1988)].
21. S. A. Suleĭmanova, Tr. Fiz. Inst. Akad. Nauk SSSR **199**, 42 (1989); S. A. Suleymanova, in *Proceedings of the Lebedev Physics Institute* (Nova Science, Commack, 1989), Vol. 196, p. 55.
22. R. N. Manchester, Astrophys. J., Suppl. Ser. **23**, 283 (1971).
23. G. R. Huguenin, J. H. Taylor, and T. M. Troland, Astrophys. J. **162**, 727 (1970).
24. V. A. Izvekova, A. D. Kuz'min, and Yu. P. Shitov, Astron. Zh. **59**, 536 (1982) [Sov. Astron. **26**, 324 (1982)].
25. S. A. Suleĭmanova and V. A. Izvekova, Astron. Zh. **61**, 53 (1984) [Sov. Astron. **28**, 32 (1984)].
26. S. A. Suleymanova, V. A. Izvekova, J. M. Rankin, and N. Rathnashree, J. Astrophys. Astron. **19**, 1 (1998).
27. A. D. Kuzmin, V. A. Izvekova, Yu. P. Shitov, *et al.*, Astron. Astrophys., Suppl. Ser. **127**, 355 (1998).
28. F. D. Drake and H. D. Craft, Nature **220**, 231 (1968).
29. S. A. Suleĭmanova and V. D. Pugachev, Astron. Zh. **76**, 287 (1998) [Astron. Rep. **42**, 252 (1998)].
30. A. F. Cheng and M. A. Ruderman, Astrophys. J. **229**, 348 (1979).
31. I. F. Malov, V. M. Malofeev, G. Z. Machabeli, and G. I. Melikidze, Astron. Zh. **74**, 303 (1997) [Astron. Rep. **41**, 262 (1997)].

Translated by Yu. Dumin

Origin of Prolonged X-Ray Flares on Active Late-Type Stars

I. M. Livshits and M. A. Livshits

Institute of Terrestrial Magnetism, Ionosphere, and Radio Wave Propagation, Russian Academy of Sciences,
Troitsk, Moscow oblast, 142190 Russia
Received June 8, 2001

Abstract—Soft X-ray data for prolonged flares in subgiants in RS CVn binary systems and some other active late-type stars (AB Dor, Algol) are analyzed. During these nonstationary events, a large amount of hot plasma with temperatures exceeding 10^8 K exists for many hours. Numerical simulations of gas-dynamical processes in the X-ray source—giant loops—can yield reliable estimates of the plasma parameters and flare-source size. This confirms that such phenomena exist while considerable energy is supplied to the top part of a giant loop or system of loops. Refined estimates of the flare energy (up to 10^{37} erg) and scales contradict the widely accepted idea that prolonged X-ray flares are associated with the evolution of local magnetic fields. The energy of the current component of the large-scale magnetic field arising during the ejection of magnetic field by plasma jets or stellar wind is estimated. Two cases are considered: a global stellar field and fields connecting regions with oppositely directed unipolar magnetic fields. The inferred energy of the current component of the magnetic field associated with distortion of the initial MHD configuration is close to the total flare energy, suggesting that large-scale magnetic fields play an important role in prolonged flares. The flare process encompasses some portion of a streamer belt and may propagate along the entire magnetic equator of the star during the most powerful prolonged events. © 2002 MAIK "Nauka/Interperiodica".

1. INTRODUCTION. SOLAR−STELLAR ANALOGIES

Phenomena similar to solar activity develop on late-type stars that rotate and possess a surface convective zone. Impulsive flares in the optical continuum are observed fairly frequently on some red dwarfs. In recent years, stellar flares have been observed in soft X-rays, and both impulsive and prolonged nonstationary events lasting from several hours to 1−2 days have been detected. Flares with durations exceeding 3 h occur very seldom on dwarfs, whereas such events are observed fairly frequently on luminous, active late-type stars—in particular, some late-type subgiants in RS CVn systems, for which the energy of such flares exceeds the total energy of analogous phenomena on the Sun by four to five orders of magnitude.

In recent studies, it has usually been assumed that prolonged X-ray flares arise during the transformation of magnetic-field energy in the radiating volume to other kinds of energy, such as radiation, kinetic and thermal plasma energy, and energy of accelerated particles. A relationship similar to that usually applied to impulsive flares is used to estimate the energies of prolonged flares. The flare energy is taken to be the change in the energy of the local magnetic field in the region of primary energy release, which is at heights of less than 10 000 km in the case of impulsive solar flares.

The total energies of prolonged flares are estimated using the relationship

$$E_{\text{tot}} = (B^2 - B_0^2)\frac{V_{\text{loop}}}{8\pi}, \qquad (1)$$

where B and B_0 are the field intensities in the loop before and after the flare process and the volume V_{loop} is taken to be the loop volume. In (1), B_0 is determined from the condition that the magnetic and plasma pressures in the loop be equal at the flare maximum. This formula has been applied to the analysis of data for prolonged flares in a number of studies (see, for example, [1]). An exception is [2], in which the volume of the soft X-ray source in a flare is assumed to be comparable to the volume of the star and a different expression is used to estimate the energy. The intensities B for various prolonged flares estimated using (1) reach several kilogauss, which is completely implausible for fields in the coronae of the stars considered. This inconsistency stimulated our current study.

Below, we will use experience gained from analyses of X-ray data for solar flares. As a rule, impulsive flares develop at low heights, near the boundary between the chromospheric and coronal gas, in regions immediately adjacent to sunspots. The development of impulsive flares is connected in many respects with the acceleration of large numbers of electrons and with subsequent secondary processes, in particular,

the evaporation of hot plasma to the coronal part of the loop.

Frequently, a sufficiently powerful pulse will stimulate further development of the flare process. This is manifest as a brightening of many bright points along the line separating opposite polarities of the radial component of the magnetic field,[1] beginning from the site of the flare (frequently an "inlet" in the sunspot penumbra or even umbra) and sometimes extending to the boundaries of the active region. These bright points probably represent the feet of very low loops. The process moves upward over a few seconds, and a system of soft X-ray loops that gradual fill with hot plasma is ignited. An arcade of loops above a neutral line of the longitudinal magnetic field can radiate X-rays for up to an hour, with its feet being the brightest in both X-ray and optical lines during most of this time. In observations of the solar disk, these feet are visible as two ribbons, so such events are called two-ribbon flares. In addition to the feet, the region near the top is also bright in X-rays, visible as a cusp near the limb. In a large flare, there can be dozens of coronal loops (sometimes as many as several hundred), with the energy release being prolonged and strongly variable near the top of each. The "burning" of the loop arcade, which in most cases does not rise above 70 000 km, represents the basic process that we will call an active-region or X-ray flare.

One of the greatest achievements in solar-flare research was the detection and study of X-ray sources located near the tops of loops (or systems of loops). Observational evidence for magnetic reconnection as the primary source of energy release in prolonged flares [3, 4] was probably first obtained for the flare of February 21, 1992. An important unsolved problem is the role of coronal mass ejections (CMEs) in powerful, nonstationary processes. CMEs frequently begin near a flare maximum, with an eruption and rising of hot loops and divergence of the flare ribbons. Sometimes, eruptions of filaments (prominences)— i.e., cold plasma—can be observed instead of CMEs. The relationship between the onset of a two-ribbon flare and these eruptions has given rise to the name "eruptive flare" for these phenomena.

In connection with powerful stellar flares, we should point out two probable aspects of CMEs in the development of solar phenomena. First, a large-scale eruption can result in open magnetic configurations, at least at sufficiently great heights. This promotes the formation of a singular point of the magnetic field, probably at a height of about $0.1\,R_\odot$ from the surface in the case of large active regions. This

creates the conditions necessary for reconnection (primary energy release). Further, the process must be supported over a time comparable to an hour.

The most powerful solar flares possess complex spatial and temporal structures. In many cases, a CME initiates another stage of a two-ribbon flare— ignition of the system in another part of the active region or activity complex; a well known example is the second flare observed on Bastille Day, July 14, 2000 [5]. This prolongs the overall duration of the event, sometimes by an appreciable factor, extending the process beyond the active region (to regions of weak magnetic fields) and facilitating the development of systems of giant arches (so-called dynamic flares in the terminology of Svestka *et al.* [6] and sigmoid-shape flares [7, 8]). In such phenomena, arches can rise to heights exceeding 100 000 km, and a system of giant arches can exist and be observable in both X-rays and H_α emission for up to a day.

Second, in the early 1980s, Sturrock [9] and Kopp and Pneuman [10] put forward the idea of posteruptive energy release. This suggests that a CME results in an open magnetic configuration and the appearance of additional currents in the corona. The system's recovery to the initial magnetic configuration may be accompanied by the formation of a vertical current sheet, with a possible subsequent reconnection of magnetic lines in this sheet.

Modern observations show that this idea is realized on the Sun during the recovery or formation of streamers [11] and also in processes leading to global restructuring of the corona [12]. Unfortunately, on the Sun, numerous CMEs are observed that are not accompanied by posteruptive energy release (i.e., significant X-ray flux); moreover, the X-ray radiation is weak in purely "coronal" solar flares, when this process is activated. Slow, high flares are most closely associated with CMEs, suggesting that the prolonged energy release is posteruptive in this case. In rare cases, these long-decay flares, which display a very prolonged decrease in their soft X-ray radiation, are adjacent to eruptions of systems of giant coronal loops, resulting in a global restructuring of the solar corona (see, for example, [12]). These phenomena occur outside the activity zone, at high latitudes, so formally they should not be considered flares.

However, a situation in which the large-scale magnetic field on the Sun is not sufficiently developed to provide the necessary efficiency of the associated posteruptive energy release is quite plausible. The situation may be different on active, late-type stars, especially those more luminous than the Sun. Therefore, the attractive model of Kopp and Pneuman [10] cannot be completely rejected when analyzing events on these stars.

---

[1]It is usual to call this the neutral line of the longitudinal magnetic field $H_{\parallel}$.

The first explanation for prolonged emission from a nonstationary event in very soft X-rays (65–190 Å) on the red dwarf AU Mic was proposed by Cully *et al.* [13], who suggested that emission from a CME was detected in this event, which last more than half a day. In contrast, we proposed in [14] that such prolonged processes were associated with posteruptive energy release. We emphasize that the temperature in the source of very soft X-rays during the prolonged event on AU Mic was about an order of magnitude lower than at the maximum of the powerful prolonged stellar flares analyzed in the current paper.

In even a preliminary analysis of observations of prolonged stellar flares, the power and spectrum of their X-ray radiation suggest that dense loops with sizes comparable to the stellar radius may be the source of the emission. Therefore, when estimating the physical conditions in the radiating loops, it is useful to consider the energy balance in these loops. Based on studies of similar phenomena on the Sun [11, 15], we will consider the gas-dynamical stage of the process, when the magnetic field no longer appreciably affects the process, except for confining the plasma in the loop and maintaining the anisotropy of the heat transfer. This is consistent with the fact that the ratio of the gas and magnetic pressures, $\beta = 8\pi p/B^2$, begins to exceed unity at the large heights in the stellar coronae considered.

A large series of studies of variations of physical parameters during flares has been carried out on the basis of the one-dimensional Palermo–Harvard code for modeling gas-dynamical processes (see [16, 17] and references in [17]). This code was initially developed for short flares and has recently been applied to prolonged phenomena. The key point in this approach is taking into account the supply of material from the chromosphere to the coronal loop; for this reason, the calculations can successfully describe X-ray observations of flares lasting hundreds of seconds (see Fig. 4 in [17]).

However, in events lasting from many hours to several days, processes in the transition region between the chromospheric and coronal plasma no longer dominate, and the evolution of giant coronal loops becomes important. Accordingly, for prolonged events, we have computed the gas-dynamical processes in an already-formed coronal loop containing a fixed mass. The main aim of our simulations was to consider the energy balance in the loop and elucidate the major factors leading to such a slow decrease in the temperature during the process. We were also very interested in the relationship between the scale of the events and their power.

Below, we briefly discuss the main X-ray observations and a preliminary analysis of these observations,

present the results of our simulations, and consider the question of the energy source for prolonged stellar flares.

2. X-RAY DATA ON PROLONGED STELLAR FLARES

Over the last ten years, observations of powerful flares on active late-type stars have been obtained by instruments on the Ginga, EUVE, ASCA, and BeppoSAX spacecraft. These observations were carried out in soft X-rays and the extreme ultraviolet. Most of these flares were on subgiants in RS CVn binary systems [18–20]; they include somewhat shorter events, for example, on the young, late-type G star AB Dor [1], as well as prolonged processes on Algol—a B8 IV–V + G–K IV binary [21]. Some prolonged soft X-ray and EUV flares were detected for the red dwarfs AU Mic and EV Lac. Some observational data and the results of an analysis of the soft X-ray radiation from prolonged stellar flares are listed in the table.

The table shows that the plasma temperature at the maximum of many long-duration flares exceeds 100 MK and that the high temperatures and emission measures persist for many hours. Prolonged flares on the subgiant UX Ari occur fairly frequently for RS CVn stars. In particular, on August 29, 1994, ASCA observed the growth phase and maximum of a flare with maximum temperature $T_{\max} = 220$ MK and emission measure EM $= 3 \times 10^{54}$ cm^{-3} [2]. On November 9, 20, and 22, 1995, three flares with durations for the X-ray decay phase of 5.2, 23.0, and
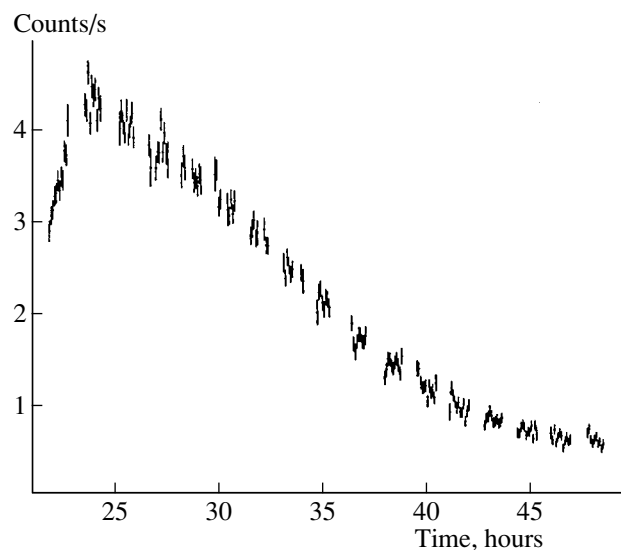
Fig. 1. A sample recording of the X-ray emission from a prolonged stellar flare. This flare on UX Ari was observed on August 28–30, 1997, on BeppoSAX in the 1.8–10.5-keV range by Pallavicini and Tagliaferri [19].

Data on prolonged X-ray flares

Date	Star	T, 10^6 K	EM, 10^{54} cm^{-3}	t, h	E_X, erg	Spacecraft	Reference
July 24–25, 1987	UX Ari	>100	10	>12	10^{37}	Ginga	[22]
August 28–30, 1997	UX Ari	111.5	5.13	30	5×10^{36}	BeppoSAX	[19]
November 9, 1997	AB Dor	110	5.5	5	4×10^{35}	BeppoSAX	[1]
November 29, 1997	AB Dor	110	3.7	4	7×10^{35}	BeppoSAX	[1]
August 30, 1997	Algol	$\approx$100	10	50	1.4×10^{37}	BeppoSAX	[21]
June 23–25, 1991	HR 5110	110	0.7	70	$>4 \times 10^{36}$	ROSAT	[20]

31.5 h were observed during long-term monitoring with EUVE [18]. Note that the interval from November 19–25, 1995, can be considered a single, prolonged nonstationary event on this star.

Hard emission with $h\nu > 20$ keV was recorded from one of the most powerful flares on UX Ari on August 29, 1997 [19], giving rise to appreciable interest in the processes occurring on this star. BeppoSAX recorded $T = 111.5$ MK and EM $= 5.13 \times 10^{54}$ cm^{-3} for this hard X-ray flare, which lasted longer than a day, on August 28–30, 1997 (Fig. 1), during the time of the maximum observed soft X-ray flux. Note that the total energy of this flare was comparable to that observed for this star by Ginga [22] in a flare that lasted about a day. Pallavicini and Taglioferri [19] believe that the total energy of the flare of August 28–30, 1997, exceeded 6×10^{36} erg.

3. RESULTS OF NUMERICAL SIMULATIONS OF THE EVOLUTION OF GIANT FLARE LOOPS

Let us briefly consider the general problem of modeling prolonged X-ray flares on the Sun and active late-type stars. It is known that the soft X-ray emission from impulsive events on the Sun and stars is connected with the free radiation of a hot coronal cloud (loop) formed during the flare. Following Pallavicini et al. [23], we introduce the time scale for the decline in the count rate or luminosity of the X-ray radiation by a factor of e, $\tau_d = d \ln I/dt$. In impulsive flares, τ_d is determined by the plasma radiative time scale in the source, $\tau_{\text{rad}} = 3kT/nL(T)$, where, as usual, $L(T)$ is the volume radiative-loss function; the radiative losses are usually taken to be $n_e^2 L(T)$ for a unit volume. For prolonged flares, τ_d exceeds τ_{rad} by

a factor of 3–30, distinguishing these events from impulsive phenomena and requiring additional plasma heating in the source of the soft X-ray radiation.

To estimate the energy required for the flare process and the plasma parameters in the source, we will consider, as in [5], a simple one-dimensional model for the behavior of a fixed amount of plasma in a loop with a constant cross section. For simplicity, we will take the loop axis to be semicirclular (Fig. 2). As the gas in the top part of the loop is heated, the loop can either expand or contract.

We analyzed the energy balance in a single giant loop by solving a set of one-dimensional gas-dynamical equations taking into account the height variations of the gravity, heat conduction, and radiative losses:

$$\frac{\partial v}{\partial t} = -\frac{\partial p}{\partial s} - g, \qquad (2)$$
$$\frac{\partial z}{\partial s} = \frac{1}{nm_{\text{p}}},$$
$$\frac{\partial \varepsilon}{\partial t} = -p\frac{\partial v}{\partial s} - \frac{\partial W}{\partial s} - Q_{\text{rad}} + H.$$

Here, the Lagrangian coordinate s and Euler coordinate z (along the loop) are measured from the base of the corona of the quiescent star, the Lagrangian coordinate $s(z) = \int_{z_0}^{z} n(z')m_{\text{p}}dz'$, $n = n_e = n_{\text{p}}$ is the density of completely ionized hydrogen plasma, m_{p} is the proton mass, the thermodynamic equations of state for such plasma are $p = 2nkT$ and $\varepsilon = 3kT/m_{\text{p}}$, g is the gravitational acceleration, $W = -\kappa m_{\text{p}}n\frac{\partial T}{\partial s}$ is the heat flux, $\kappa = 10^{-6}T^{5/2}$ is the heat conductivity, $Q_{\text{rad}} = (1/m_{\text{p}})nL(T)$ are the radiative losses, and H is the heating of the plasma per unit mass.
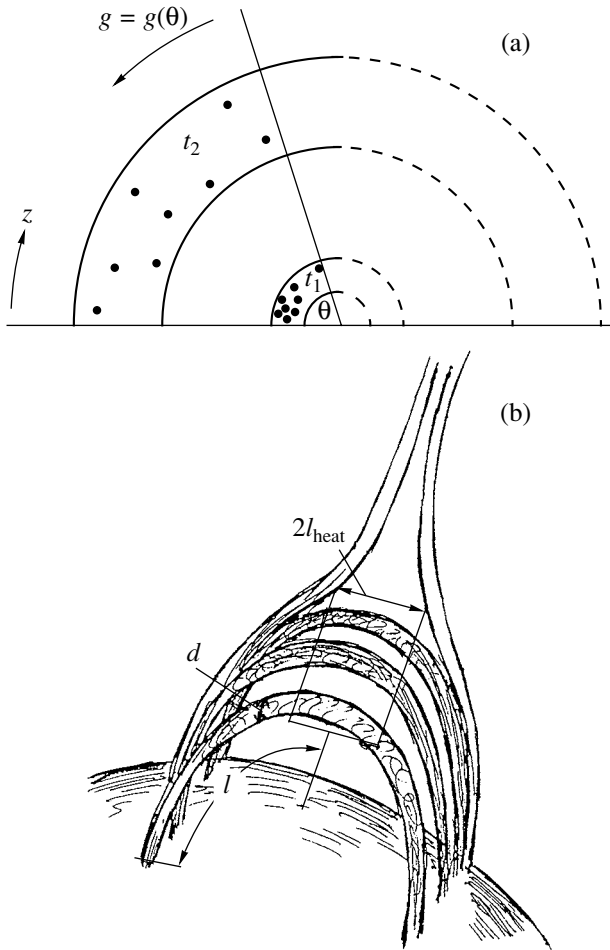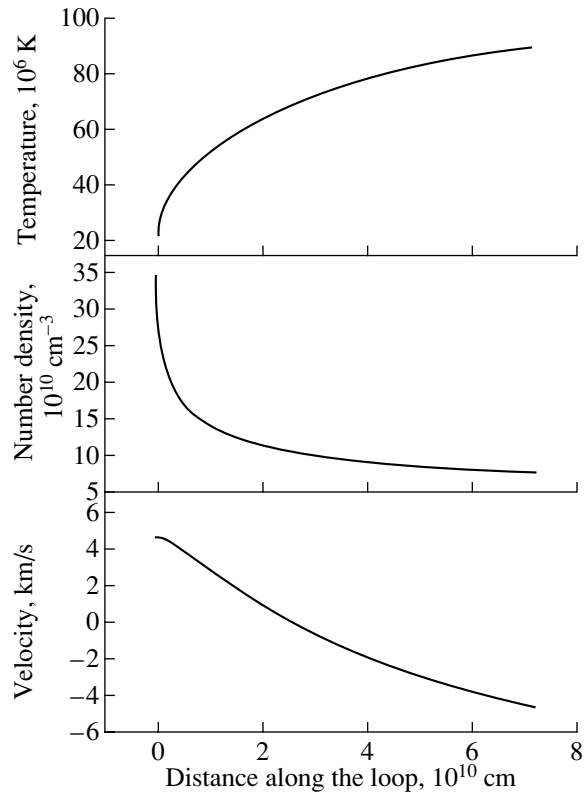
Fig. 2. (a) Schematic presentation of a loop for two times. The gravity depends on the position angle, i.e., the height in the corona. (b) Schematic of a system of loops; d is the loop diameter, $2l$ its length, and $2l_{\text{heat}}$ the total size of the heated region (in Section 4, the extent of the entire system along the neutral line of the magnetic field is designated ζ).

Fig. 3. Variation of physical parameters along the loop 5 h after the onset of the flare on UX Ari. The distance along the loop is measured from one of its feet. Positive velocities correspond to plasma motion away from the photosphere (i.e., the loop is contracting).

The gas mass is specified by the density at the feet of a loop with constant temperature. The boundary conditions are constancy of the pressure at the loop extremes and, for the energy part of the system, constancy of the temperature from below and of the thermal flux from above (specifically, we have accepted $dT/dl = 0$). These initial conditions correspond to an isothermal hydrostatic loop with some density at its feet, temperature ($T > 10^6$ K), and loop (half-)length. Thus, the choice of the mass of heated gas is also determined.

The development of the process essentially depends on the heating. As earlier, we assumed that plasma heating takes place near the loop top and is distributed in time and in space (over the mass

Lagrangian coordinate):

$$H = H_0 \cdot \exp\left\{-\left(\frac{s}{s_1}\right)^2\right\} \cdot \exp\left\{-\left(\frac{t - t_1}{t_2}\right)^2\right\}, \tag{3}$$

where H_0 is the amplitude in erg g^{-1} s^{-1}, t_1 is the time to achieve the maximum, and t_2 is the width of the temporal profile.

In order for the process considered to be possible—i.e., for the bottom part of the loop to not cool before the arrival of the heat perturbation—we introduced a small constant contribution to the heating function, numerically equal to the radiative energy losses of the corona outside the flare. This stationary heating did not exceed 10% of H_0 for the flares simulated here. Note that the effect of this heating is also manifest in the final stage of the event, at the end of the main heating.

Our modification of the earlier code [15], developed for solar flares, makes it possible to perform computations for various values of the gravitational acceleration and other characteristic parameters. In particular, the radiative-loss function was extended
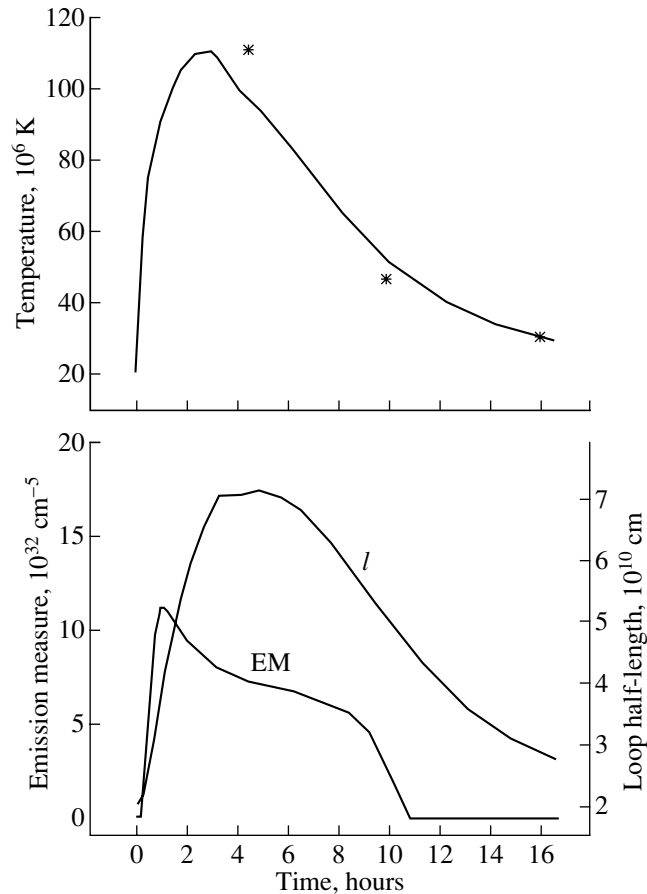
Fig. 4. Results of modeling the flare on UX Ari: time dependences for the temperature at the loop top, emission measure, and loop half-length. The observed temperatures from [19] are shown with asterisks.

compared to the treatment in [15] to temperatures $T > 20$ MK, in accordance with the calculations of [24]: $L(T) = 10^{-24.73} T^{0.25}$ cm^3 s^{-1}.

We note here two points.

(1) We use the boundary condition at the loop feet, allowing the loop to expand in both directions. To model flares in active regions on the Sun (the hot phases of solar flares), the best condition at the loop feet is $v = 0$, which implicitly takes into account some input of plasma from the chromosphere to the coronal part of the loop. This formulation of the problem is closer to [17], which leads to better consistency of the solutions.

(2) Generally speaking, the code is intended primarily for simulations of the decay phase. Computations for the entire flare lead to difficulties due to the asymmetry of the growth and decay phases in the soft X-ray light curve observed in the overwhelming majority of cases. The evolution of a giant coronal loop with smooth, slowly varying heating characteristically shows similar durations for loop expansion and contraction phases, accompanied by radiative growth and decay. When modeling the observed

growth phase for the X-ray radiation, which lasts only 0.5−1 h in the events analyzed, large plasma velocities in the loop result. After the loop expansion is replaced by contraction, the downward plasma motions lead to the formation of shocks near the loop feet, making further computations impossible. To model the next, very prolonged, decay phase of processes developing in the densest loops, we must either dampen these motions artificially or make computations for the growth and decay phases separately when modeling powerful events. The final results of these two artificial approaches do not differ strongly.

We carried out simulations for initial densities at the feet of an isothermal loop from 2×10^{10} to 5×10^{11} cm^{-3}, sizes for the loop half-length $l = (0.5-5) \times 10^{10}$ cm, and heat fluxes varying over broad limits. We considered processes whose total energy did not exceed 10^{37} erg. We obtained temperatures at the loop top in the range $(10-200)$ MK. The gravititational acceleration could take on values $10^2-4 \times 10^4$ cm s^{-2}.

When modeling processes for a particular star, there was some set of parameters for which a small

change of one or more of them led to a change in the character of the process and a transition from weak to strong expansion of the loop. These two classes of solutions existed in virtually all the examples we analyzed. In the computations for powerful processes in dense loops, these two classes of solutions also differed in that the temperature at the event maximum was either below or above 100 MK.

We carried out simulations for three late-type stars, which, together with the Sun, cover the main types of active objects on which prolonged X-ray flares have been observed. The first was the K0 subgiant in the UX Ari binary system, where analogous activity is very strongly pronounced. The gravitational acceleration for this star is rather small: we adopted $g_* = 8.8 \times 10^2$ cm/s^2. The second star, AB Dor, is the well-known young K1 dwarf, with an age of only 20–30 millions of years; as in [1], we adopted the stellar radius $R_* = R_\odot$, mass 0.76 $M_\odot$, and, accordingly, $g_* = 2.14 \times 10^4$ cm/s^2. As an example of prolonged X-ray superflares, which are observed in Algol and RS CVn systems, we have considered a giant flare on HR 5110≡BH CVn (F2IV+K2IV) [20], assuming the mass ratio for this system to be $M_2/M_1 = 0.54$ and the gravitational acceleration on the secondary K subgiant to be $g = 4 \times 10^3$ cm/s^2.

We paid special attention to the simulations for UX Ari. Figures 3 and 4 show the results of the computations for this star with $H_0 = 4.5 \times 10^{13}$ erg/(g s), $t_1 = 0.5$ h, and $t_2 = 5$ h. This strong heating can supply the observed temperature in an X-ray flare. The initial density at the feet of the isothermal loop with $T_0 = 20$ MK was $n_0 = 4 \times 10^{11}$ cm^{-3}, and the loop half-length was $l = 2 \times 10^{10}$ cm.

Figure 3 shows a typical distribution of physical parameters along the loop for the onset of the decay of an X-ray flare (5 h after the beginning of the flare process). The temperature profile reflects the fact that heat conduction is the main process for heat transfer. The density decreases with height, but exceeds 7×10^{10} cm^{-3}, even at very large heights. The velocities of the loop expansion or contraction (i.e., of the plasma motions near the loop feet) are several km/s, which is typical of our simulations. Note that the loop size has increased over the initial size by a factor of 3.5.

Figure 4 shows the distribution of temperature at the loop top, the emission measure of the hot gas with $T > 50$ MK, and the loop half-length during the flare. Three observed temperatures referred to the centers of the exposures are also given. We can see that in the flare decay phase the process considered can cool the X-ray source over a half day. The emission measures of the plasma with temperature $T > 50$ MK are given here for one half of the loop, EM$_l$

(maximum 10^{33} cm^{-5}); we obtain the value EM$_V = 5 \times 10^{54}$ cm^{-3} for the entire system of loops by multiplying the calculated values of EM$_l$ by the "effective" area 5×10^{21} cm^2 (see below). Thus, the existence of a hot source over about half a day can be explained.

The asymmetry of the $T(t)$ dependence in Fig. 4 is due to the assumed time behavior for the main heating, and the temperature decrement is almost completely determined by the value of t_2. At the latest stage of the flare, heating from the surrounding corona becomes important, affecting the shape of the $T(t)$ curve.

Note that the temperature behavior outstrips the variations in the loop length. The time for the maximum loop expansion virtually coincides with the time when the highest temperature is achieved, but the temperature then falls, with any appreciable contraction occurring only after some delay. In this giant flare, the sharp contraction of the loop after the peak of the nonstationary event (sometimes observed on the Sun—the so-called "shrinkage" effect [4]) is almost invisible. In this case, the absence of this feature is due to very intense heating under low-gravity conditions.

Powerful but shorter flares can also be successfully analyzed using these simulations. In particular, Figure 5 shows similar results for a typical X-ray flare on AB Dor. The initial conditions in the loop were similar to those used previously—$T_0 = 20$ MK and $n_0 = 4 \times 10^{11}$ cm^{-3}—but the initial loop half-length was somewhat smaller, $l = 1.5 \times 10^{10}$ cm. The main difference from the previous case is the heating-function parameters at the loop top ($H_0 = 1.5 \times 10^{13}$ erg/(g s), $t_1 = 6.7$ min, $t_2 = 1$ h), as well as the shorter (by approximately a factor of four) duration of the event (see Fig. 4). This also affected the loop half-length, which was about two-thirds that for the flare on UX Ari. Note that, for subsequent comparison with the observations, Figure 5 shows the emission measure of gas with $T > 30$ MK rather than $T > 50$ MK, as in Fig. 4; therefore, the actual emission measures for the two cases are similar.

We were also able to model the superflare on HR 5110. However, the result turned out to be similar to that already discussed above for UX Ari. A description of the entire process requires a somewhat slower decay of the heating function. The loop half-length is slightly greater than $l = 8 \times 10^{10}$ cm. The question of whether the whole set of flare activity on UX Ari on November 19–25, 1995 [18], should be considered a single flare or a superposition of series of bursts remains open. The shape of the light curve of the flare on HR 5110 is better described by a single flare event. A transition to greater heating fluxes results in the ejection of a system of loops. The
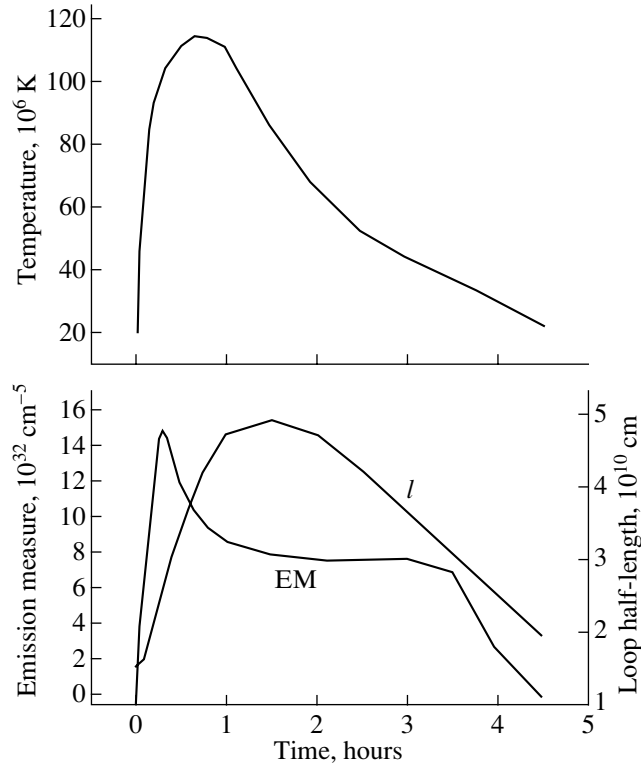
Fig. 5. Same as in Fig. 4 for a typical prolonged X-ray flare on AB Dor.

flare on Algol g [21] has similar parameters as that on HR 5110, and simulations also proved possible.

Our simulations enable us to estimate the area of the flares projected onto an image of the corona (i.e., onto the celestial sphere). Let us assume that the flare center consists of a set of m loops, each with a length $2l$ (Fig. 2b). In this case, the volume emission measure can be represented

$$\mathrm{EM}_V = S_1 \mathrm{EM}_l = 2md^2 \int\limits_0^l n_e^2 dl, \qquad (4)$$

where d is the loop diameter. The value of EM_V is obtained from observations, while $\mathrm{EM}_l = \int_0^l n_e^2 dl$ is yielded by the simulations.

The total energy of the process is

$$E = S_2 H_f = 2ml_{\mathrm{heat}}\, d \int\!\!\int H\, ds dt, \qquad (5)$$

where l_{heat} is the length of the heated part of the loop. During its operation, the code computes the total heating, i.e., integrated over the Lagrangian coordinate s and over time: $H_f = \int\!\int H\, ds\, dt$ (in units of erg cm^{-2}).

For example, for the flare on UX Ari we have considered, $H_f \approx 6.2 \times 10^{14}$ erg cm^{-2} and $\mathrm{EM}_l \approx$ 7×10^{32} cm^{-5} throughout the decay phase, which lasted 14 h. From the values in the table, $E = 5 \times 10^{36}$ erg and $\mathrm{EM} = 5.1 \times 10^{54}$ cm^{-3}, we obtain $S_1 \approx S_2 = 8 \times 10^{21}$ cm^2. Accordingly, for the flare on AB Dor, $H_f \approx 1.3 \times 10^{14}$ erg cm^{-2} and $\mathrm{EM}_l \approx$ 7×10^{32} cm^{-5} during the decay phase, which lasted about 4 h. From the values $E = 5 \times 10^{35}$ erg and $\mathrm{EM} = 5 \times 10^{54}$ cm^{-3}, we obtain $S_1 \approx 4 \times 10^{21}$ cm^2 and $S_2 \approx 7 \times 10^{21}$ cm^2. We can see that, for these two powerful flares with very different durations, the areas of the X-ray source were very large. This implies that a prolonged flare can indeed be considered to represent the evolution of stationary loops that diverge with height. Such ideas were developed in [25]. The difference between the S_1 values for the two flares testifies to their different L_{heat}/d ratios. Essentially, we can use the two above equations to estimate the number of loops m and diameter of each loop d. We can say only that our analysis favors a large number of thin loops; however, the accuracy of these estimates is low.

For the entire sample of prolonged X-ray flares considered, ranging from those occurring on the Sun, on red dwarf stars, and weak events on subgiants to powerful events on active late-type stars, our analysis leads us to conclude that flare power is to some extent related to the size of the coronal loop but very

strongly depends on the extent of the corresponding loop system along the neutral line of the magnetic field. In any case, prolonged heating of the plasma at appreciable heights in the loops is required for such flares to develop.

4. ESTIMATE OF THE TOTAL MAGNETIC-FIELD ENERGY

The energies of the prolonged stellar flares we are studying are very large. They would require, for example, the annihilation of oppositely directed magnetic fields with intensities of $(1-2) \times 10^3$ G in the entire volume of the system of giant loops $(V \approx \mathrm{EM}_V/n^2 \approx 10^{31}-10^{32}$ cm^3). Fields this strong cannot exist in the outer atmospheric layers of the stars considered, in particular, in their lower coronae. Therefore, reconnection of local magnetic fields cannot supply the energy required by these flares.

Attention was first drawn to the fact that some stellar activity may be related to the evolution of larger scale (not local) magnetic fields in [26]. For nonstationary processes, this refers first and foremost to prolonged posteruptive energy release resulting in the development of systems of giant coronal loops. We can imagine the reconnection of lines of force in the equatorial region of the global (dipole) field of the entire star, deformed by the stellar wind. For the Sun, this corresponds to the streamer belt, located above the region where the interplanetary current sheet adjoins the corona.

Let us estimate the energy of the current component of the magnetic field for the entire streamer belt around a star. We will use the stationary solution of the following problem [27]. We set a dipole magnetic field on a sphere of radius R, which stretches outward to a medium with a given magnetic Reynolds number Re_m. The stationary solution of the basic equation of ideal magnetic hydrodynamics with the boundary condition for the radial magnetic field component $B_r\big|_{r=R}= 2m\cos\theta/R^3$ on a sphere of radius R was sought in [27] as

$$B_r = \frac{1}{r^2}\frac{1}{\sin\theta}\frac{\partial\psi}{\partial\theta}, \qquad (6)$$

$$B_\theta = -\frac{1}{\sin\theta}\frac{\partial\psi}{\partial\theta}. \qquad (7)$$

Separating variables, we obtained in [27] the solution

$$\psi = \frac{a\sin^2\theta}{R(\mathrm{Re}_m+2)}\left(\mathrm{Re}_m+2\frac{R}{r}\right). \qquad (8)$$

The run of the field lines for $\mathrm{Re}_m = 10$ is shown in Fig. 7 in [27].

Integrating over the volume outside the sphere of radius R, we obtain the energy of this field:

$$E = 2\frac{m^2}{3\,R^3}\left(1 - \frac{2\,\mathrm{Re}_m+2}{(\mathrm{Re}_m+2)^2}\right) \approx 2\frac{m^2}{3\,R^3}. \qquad (9)$$

Taking into account the fact that the energy of the corresponding dipole magnetic field outside the sphere of radius R is

$$E = \frac{m^2}{3\,R^3} \qquad (10)$$

(see, for example, [28]), we find that, for large Reynolds numbers, the energy of the current components is close to the energy of the dipole field.

We can estimate the energy stored in a heliospheric current sheet as follows. At the solar minimum, the global solar magnetic field is close to dipolar, with the dipole axis close to the rotational axis. At large distances from the Sun, the lines of force of the interplanetary magnetic field are nearly radial. The simplest way the sources of such a field can be represented in the outer corona and distant parts of the heliosphere is as a superposition of a point-like dipole for the Sun and an infinitely thin ring current in the equatorial plane with surface current density $j_\phi \sim r^{-3}$ [29]. Tarasova et al. [30] estimated that the energy stored in this current is of the order of the dipole field energy contained above the onset of the wind outflow. This is consistent with the results of our integration of the distribution of a field with the form depicted in Fig. 2 in [27].

The previous relationship can be rewritten $E = (1/3)B_\odot^2 R_\odot^3$. With a field near the solar poles $B_\odot = 1$ G, we obtain a current energy of 1.1×10^{32} erg. Note that performing the integration starting from the sphere of the solar wind source does not substantially change this value. The estimated energy does not exceed the energy of prolonged solar flares.

Dipole-type magnetic fields on active late-type stars are now beginning to be measured, and the derived intensities are of the order of tens of gauss (see, for example, [31]). The stellar wind from active late-type stars, especially subgiants in RS CVn systems, is much more powerful than the solar wind. For UX Ari, whose K0 subgiant has a radius of $4.7R_\odot$ and a field on the dipole axis of 30 G, the estimated current energy is $E \approx 3 \times 10^{36}$ erg. The sizes of some other active late-type stars are not so large, but, in general, the fields can be somewhat stronger.

We emphasize that a prolonged stellar flare need not encompass the entire streamer belt. Most often, the flare process occurs in some interval of longitudes along the neutral line of the large-scale field. Observations of large, nonstationary events on the Sun show that two cases are possible. In the first,

the neutral line is frequently distorted and the surface of the interplanetary current sheet becomes nonplanar and corrugated. This occurs if unipolar regions with oppositely directed magnetic fields develop on opposite sides of the neutral line of the large-scale field. This corresponds to a four-sector structure of the interplanetary magnetic field, which most often exists in the heliosphere. Nonstationary processes that develop as stability is disrupted in some part of the streamer belt result in a global restructuring of the corona.

In the second case, from time to time during a cycle, large activity complexes form in the same longitude interval, in which powerful X-ray flares lasting from several hours to about a day can occur. This case is the closest to the prolonged stellar flares considered in this paper. The energy of such events can be estimated by approximating the magnetic field by that of a plane dipole, as is sometimes done for two-ribbon flares on the Sun. Here, we will present a very simple estimate, though it will be necessary to consider this problem in more detail as new results concerning the large-scale magnetic fields of stars become available.

Let us direct the z axis along the neutral line. We then have for the magnetic field of a horizontal dipole at some depth beneath the photosphere (see, for example, [32]):

$$H = \left\{ \frac{2\mu xy}{(x^2 + y^2)^2}, \quad \frac{\mu(y^2 - x^2)}{(x^2 + y^2)^2}, \quad 0 \right\}. \quad (11)$$

Here, generally speaking, the magnetic moment of the dipole μ can depend on time. The lines of force lie in the xy plane and are circles centered on the x axis and passing through the coordinate origin. We will assume that the x axis is directed radially and that the y axis is parallel to the photosphere at the position of the active region considered. Introducing the quantity $\rho = (x^2 + y^2)^{1/2}$, we readily obtain a relationship for the field energy in the region $\rho \geq \rho_1$:

$$E = \frac{\Delta z}{8\pi} \int H^2 \, ds = \frac{\zeta}{8\pi} \int \frac{\mu^2}{\rho^4} \, 2\pi\rho \, d\rho = \frac{\mu^2 \zeta}{8\rho_1^2}, \quad (12)$$

where $\zeta \equiv \Delta z$ is the extent of the arch system along the z axis.

The magnetic moment μ is related to the field intensity: when $y = 0$, $H_y = -\mu/\zeta^2$, with $x = \zeta$ at the loop top. The field energy in the region $\rho \geq \rho_1$ for $\rho_1 = 1/3 \, \zeta$ is then estimated as

$$E = (9/8)H_y^2 \zeta^3. \quad (13)$$

Thus, the estimated magnetic-field energy in a plane-dipole approximation does not differ very strongly from the case of a global dipole, with the natural distinction that this energy depends on the

extent of the system of loops along the neutral line. The distortion of the magnetic field of a plane dipole by a stellar wind is known [32], and the meaning of that problem is close to that demonstrated in [27] for a star as a whole. Repeating the analysis carried out at the beginning of this section for a global dipole, we find that the current energy arising from a distortion of the magnetic field of a plane dipole agrees with (13) to within a few tens of percent. This indicates that for the magnetic field the energies of prolonged X-ray stellar flares can be estimated using (13).

For giant arch systems in solar activity complexes, we can adopt $\zeta = 10^{10}$ cm (that is, $1/7R_\odot$ and less than 0.1 of the radius of the stars considered) and $H_y = 10$ G at the top of the loops. Then, (13) corresponds to $E \leq 10^{32}$ erg, in agreement with observations of solar flares. On some active late-type stars, the field strengths and sizes can exceed those typical of the solar corona by an order of magnitude. In particular, the field intensity in activity complexes on stars or in two oppositely directed unipolar regions can appreciably exceed the field intensity near the poles (tens of gauss), as indicated by data on variations of the intensities of global fields on some late-type stars. Therefore, flares with total powers up to 10^{37} erg are possible on the most active late-type stars, as was recently observed.

5. CONCLUSION

We have analyzed recent data on the physical conditions in the sources of soft X-ray emission in prolonged flares on active late-type stars. The appearance of a large amount of plasma heated to temperatures from 50 to 100 MK is due to flare processes in giant coronal loops. By modeling the gas-dynamic processes in such a loop heated from above, we have estimated the physical conditions in the sources of soft X-ray emission for both weak flares and the most powerful prolonged flares on active late-type stars.

Our calculations confirm the results of computations using the one-dimensional Palermo−Harvard gas-dynamical code, which indicate that such flares last as long as the necessary heating continues in the top part of the loop. Furthermore, both approaches show that heat transfer dominates over other dissipative processes, in particular, radiative losses in the bulk of the loop so that the time behavior of the temperature in the source of soft X-ray emission reflects variations in the heating.

In contrast to [17], we did not use any additional assumptions, such as the conservation of entropy or adoption of a similarity law for the physical conditions in the loop. This enabled us to more reliably determine the plasma parameters and the flare-source

size. We found that powerful heating can last from several hours to a day or more, with the plasma density in a coronal flare source exceeding 10^{11} cm^{-3}. Further development of these studies requires multi-wavelength observations making it possible to directly estimate the densities in flare arches on active late-type stars.

Strong, prolonged flares differ from similar weaker events in the size of the loops involved and the extent of the system of loops along the neutral line of the magnetic field. The flare process occupies a part of the streamer belt, possibly propagating along the entire magnetic equator during the most powerful prolonged phenomena.

Our calculations can be used to estimate the total energy necessary to realize each event. The total energy of such flares, which can reach 10^{37} erg, rules out the possibility that prolonged stellar flares are associated with the evolution of local magnetic fields, widely accepted in earlier studies.

We have estimated the energy of the current component of the large-scale magnetic field, which results from the ejection of lines of force by plasma outflows or stellar wind. We have considered two cases: a global stellar field and fields connecting regions with oppositely directed unipolar magnetic fields. The estimated energy of the magnetic-field current component associated with a distortion of the initial MHD configuration is close to the total soft X-ray energy from prolonged flares and also to values yielded by our gas-dynamical simulations. Therefore, it is quite natural to associate the origin of prolonged flare phenomena with the reconnection of large-scale magnetic fields, particularly in the immediate vicinity of the tops of giant coronal loops.

Note that the weak prolonged phenomena sometimes observed on typical flare stars (both red dwarfs and late-type subgiants), characterized by fairly low plasma temperatures at the loop tops (< 10 MK), may be associated with a purely posteruptive energy release localized in vertical current sheets at large distances from the stellar surface [14].

A comparison of prolonged X-ray events on red dwarfs (and the Sun) and active subgiants suggests that, in addition to their scale, these phenomena differ in the role of coronal mass ejections in their general nonstationary processes. In the events we have analyzed here, the main role of each CME is initiating new flare centers along the neutral line of the large-scale magnetic field. On the Sun, this type of flare process is observed much more rarely [5] than the evolution of dynamic flares—rising systems of giant arches with posteruptive energy release.

The development of the most powerful processes under conditions of relatively low gravity should result in disruption of the system of loops and the ejection of plasma. Therefore, there is every reason to believe that some fraction of the energy of prolonged superflares is directly transferred to nonstationary processes developing even in the space between the components of binary systems. Our analysis of superflares supports this possibility, suggested earlier for flares on HR 5110 [20].

ACKNOWLEDGMENTS

REFERENCES

1. A. Maggio, R. Pallavicini, F. Reale, and G. Tagliaferri, Astron. Astrophys. **356**, 627 (2000).
2. M. Güdel, J. L. Linsky, A. Brown, and F. Nagase, Astrophys. J. **511**, 405 (1999).
3. S. Tsuneta, Astrophys. J. **456**, 840 (1996).
4. T. G. Forbes and L. W. Acton, Astrophys. J. **459**, 330 (1996).
5. I. M. Chertok, V. V. Fomichev, A. A. Gnezdilov, and R. Gorgutsa, Sol. Phys. (2001) (in press).
6. Z. Svestka, F. Farnik, H. S. Hudson, *et al.*, Sol. Phys. **161**, 331 (1995).
7. R. C. Canfield, H. S. Hudson, and D. E. McKenzie, Geophys. Res. Lett. **26**, 627 (1999).
8. H. Wang, P. R. Good, C. Dencera, *et al.*, Astrophys. J. **536**, 971 (2000).
9. P. A. Sturrock, Nature **211**, 695 (1966).
10. R. A. Kopp and G. W. Pneuman, Sol. Phys. **50**, 85 (1976).
11. K. V. Getman and M. A. Livshits, Astron. Zh. **76**, 704 (1999) [Astron. Rep. **43**, 615 (1999)].
12. A. McAllister, M. Dryer, P. McIntosh, and H. Singer, J. Geophys. Res. **101** (A6), 13497 (1996).
13. S. L. Cully, G. Fisher, M. J. Abbott, and O. H. W. Siegmund, Astrophys. J. **435**, 449 (1994).
14. M. M. Katsova, J. Drake, and M. A. Livshits, Astrophys. J. **510**, 986 (1999).
15. K. V. Getman and M. A. Livshits, Astron. Zh. **77**, 295 (2000) [Astron. Rep. **44**, 255 (2000)].
16. G. Peres, R. Rosner, S. Serio, and G. S. Vaiana, Astrophys. J. **252**, 791 (1982).
17. R. M. Betta, G. Peres, F. Reale, and S. Serio, Astron. Astrophys., Suppl. Ser. **122**, 585 (1997).
18. R. Osten and A. Brown, Astrophys. J. **515**, 746 (1999).
19. R. Pallavicini and G. Tagliaferri, Palermo Astronomy Preprint No. 4 (1998).
20. V. G. Graffagnino, D. Wonnacott, and S. Schaeidt, Mon. Not. R. Astron. Soc. **275**, 129 (1995).
21. F. Favata, J. H. M. M. Schmitt, G. Micela, *et al.*, Astron. Astrophys. **362**, 628 (2000).
22. T. Tsuru, K. Makishima, and T. Ohashi, Publ. Astron. Soc. Jpn. **41**, 679 (1989).

23. R. Pallavicini, G. Tagliaferri, and L. Stella, Astron. Astrophys. **228**, 403 (1990).

24. R. Mewe, J. S. Kaastra, and D. A. Liedahl, Legacy **6**, 16 (1995).

25. G. H. J. Van Den Oord and F. Zuccarello, in *Stellar Surface Structure,* Ed. by K. G. Strassmeier and J. Linsky (Kluwer, Dordrecht, 1996), p. 433.

26. M. M. Katsova and M. A. Livshits, in *Proceedings of the 11th Cambridge Workshop on Cool Stars, Stellar Systems and the Sun, 2001,* Ed. by R. J. G. Lopes, R. Rebolo, and M. R. Z. Osorio; Astron. Soc. Pac. **223**, 979 (2001).

27. S. Kouchmy and M. A. Livshits, Space Sci. Rev. **61**, 393 (1992).

28. F. A. Ermakov, *Physics of Solar Activity* [in Russian], Ed. by E. I. Mogilevskiĭ (Nauka, Moscow, 1988), p. 25.

29. I. S. Veselovskiĭ, Geomagn. Aeron. **34** (6), 1 (1996).

30. I. S. Veselovsky, in *Proceedings of the 9th European Meeting on Solar Physics, Magnetic Fields and Solar Processes, Florence, 1999,* ESA SP-448, p. 1217.

31. T. N. Tarasova, S. I. Plachinda, and V. V. Rumyantsev, Astron. Zh. **78**, 550 (2001) [Astron. Rep. **45**, 475 (2001)].

32. B. V. Somov and S. I. Syrovatskiĭ, in *Neutral Current Layers in Plasma* [in Russian] (Nauka, Moscow, 1974), Tr. Fiz. Inst. Akad. Nauk SSSR, Vol. 74, p. 14.

Translated by G. Rudnitskiĭ

Three Types of Flows in the Structure of the Solar Wind

N. A. Lotova, V. N. Obridko, and K. V. Vladimirskiĭ

Institute of Terrestrial Magnetism, Ionosphere and Radio Propagation, Troitsk, Moscow Region, 142190 Russia
Lebedev Physical Institute, Leninskiĭ pr. 53, Moscow, 117924 Russia
Received June 20, 2000

Abstract—An experimental study of the source and formation of large-scale streams in the solar wind is presented. Radio-astronomical data from 1998 are compared with optical SOHO observations and solar coronal magnetic fields calculated from Zeeman data obtained at the Wilcox Observatory. A correlation between the geometry of the solar-wind transition region and the strength of coronal magnetic fields is revealed. For the moderate heliolatitudes studied, this correlation divides into three branches corresponding to three types of coronal magnetic-field structures: open structures with field lines escaping into interplanetary space, closed structures with loop-like field lines, and intermediate structures including both open and closed configurations. High-speed streams of solar wind originate in regions with open magnetic structures. These structures are connected with the lateral lobes of streamers at moderate heliolatitudes. Low-speed flows originate above closed magnetic structures, typical of the main bodies of streamers. The lowest-speed solar-wind flows are not associated with coronal streamer structures, and originate in coronal regions with intermediate magnetic configurations simultaneously containing open and closed field lines. In these regions, the white-light corona becomes an extended and amorphous area with high luminosity, which stratifies into a radial structure with narrow stripes at higher resolution. © 2002 MAIK "Nauka/Interperiodica".

1. INTRODUCTION

We investigate here the effect of solar coronal magnetic fields on the formation of large-scale stream structures of the solar wind, based on experimental data taken in 1998, when there was a strong increase in solar activity. Studies of the real structure of the solar-wind flow become most important in connection with the acceleration of solar plasma and the formation of supersonic flows in the solar wind. We also consider data for 1997, the year in which the increase in solar activity began [1]. Experimental data indicating a significant role of magnetic fields in acceleration of the solar wind have recently appeared. Recurring magnetic storms observed in the Earth's atmosphere in the 1970s were connected with high-speed flows of solar wind originating above coronal holes [2, 3]. In these regions, the magnetic field has an open structure, with the field lines escaping into interplanetary space. In this way, high-speed solar-wind flows can be directly related to an enhanced strength of the magnetic field penetrating the solar plasma environment. Many significant processes controlling the acceleration of the solar wind have been revealed in subsequent investigations [4–11]. The most important information about the structure of the solar wind flow has been obtained from ground-based radio-astronomical observations. In particular, such studies have shown the existence of a spe-

cial type of flow in an extended region between the subsonic solar wind near the Sun and supersonic streams escaping into interplanetary space. Regular observations of natural compact radio sources have revealed an extended region of enhanced scattering of radio waves $10-30$ solar radii (R_S) from the Sun [12, 13]. Comparisons with measurements of solar-wind velocities have identified this region of enhanced scattering as a transonic transition region, where the bulk of solar-wind acceleration occurs. Moreover, the structure of the velocity field of the solar wind [16, 17] indicates that this is a region of mixed flows containing coexisting subsonic and supersonic streams [12, 15, 18].

2. RADIO-ASTRONOMICAL DATA ON THE STRUCTURE OF THE SOLAR PLASMA ENVIRONMENT

Here, we study the formation of solar-wind flows over a wide range of moderate heliolatitudes in which the transition region indicated above is usually located. We use radio-astronomical data on the geometry of the transition region as a natural quantitative measure of the solar-wind acceleration, with the transition region being closer to the Sun when the plasma acceleration is more intense. These data reflecting the acceleration efficiency are compared with data
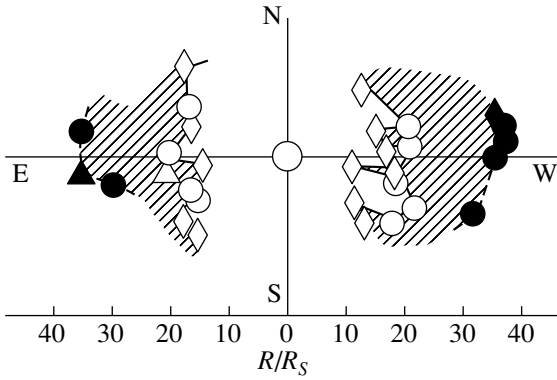
Fig. 1. Radio map of the transition region of the solar wind for 1998 (see text).

on coronal magnetic fields and optical data on the plasma-flow configuration close to the Sun.

Our objective is to study the sources of the solar wind and establish a classification for types of solar-wind flows that describes the relationship between the acceleration efficiency and the strength and configuration of magnetic fields penetrating the plasma streams.

Regular observations of natural compact radio sources—quasars and H_2O masers—have been performed since 1987 using two large radio telescopes of the Lebedev Physical Institute in Pushchino: DKR-1000 (initially at 103 MHz, and at 110 MHz since 1997) and RT-22 (at 22.2 GHz). The observation and data-reduction techniques used are presented in [12, 19]. Long series of daily observations can be used to derive the radial evolution of the radio-wave scattering defining the positions of the inner and outer boundaries of the solar-wind transition region. The inner boundary can be easily identified using the precursor, which is a narrow region with sharply decreased scattering observed near the inner boundary of the transition region in which the scattering is enhanced [12, 13, 15, 19].

Observations of radio waves scattered in the solar plasma at radial distances of $5-60R_S$ probe the entire region of the main solar-wind acceleration, which occurs at moderate heliolatitudes, within radial distances of $10-40R_S$. Observations of several sources passing near the Sun at various heliolatitudes simultaneously or almost simultaneously have been performed since 1987. This yields radio maps—two-dimensional projections of the transition region—that enable us to study the 11-year cycle of the large-scale structure of the solar-wind flow [20]. These maps cannot provide snapshots of the transition region, since there is significant evolution of the solar-wind flow during the time the data are accumulated. Nevertheless, they supply us with valuable information about the form and asymmetry of the transition

region. The experimental errors in R_{in} are estimated to be on the order of $0.5R_S$, based on the uncertainty in the scattering measurements.

Figure 1 presents a radio map of the transition region constructed from the 1998 observations. Deviations in the shape of the transition region from spherical symmetry are appreciable. The circles in Fig. 1 correspond to observations of the compact source 3C 144 in the Crab nebula and the quasars 3C 133, 3C 152, 3C 154, 3C 166, 3C 208, 3C 215, 3C 225, and 3C 228 in their approaches toward the Sun in June and August. The diamonds correspond to maser sources approaching the Sun in June (GGD4, S252A, and U Ori) and December (W31(2), IRC-20431, and W28A2(1)). The triangles correspond to the quasars 3C 2 and 3C 5 approaching the Sun in March. The transition region in Fig. 1 is shaded. The empty symbols show the inner boundary R_{inner} of the transition region, and the dark symbols, its outer boundary R_{outer}. The observations we have used correspond to moderate heliolatitudes and are consistent with new data on the extremely intense plasma acceleration in polar coronal holes obtained by instruments on spacecraft [21]. We note the common nature of these phenomena—high-speed flows of solar wind originate in regions with strong magnetic fields and open field structures.

3. STRUCTURES OF PLASMA FLOWS, OPTICAL OBSERVATIONS, AND SOLAR MAGNETIC FIELDS

To study the sources of the solar wind and formation of accelerated plasma streams, we used radio-propagation data in combination with optical observations of the white-light corona and measurements of the magnetic field near the Sun. We used SOHO observations and photospheric magnetic-field measurements obtained at the Wilcox Observatory and supplied via the Internet. We then solved the field equations for a narrow region of the solar corona, $R_S \leq R \leq 2.5R_S$, taking a sphere at $R = 2.5R_S$ to be the conventional source surface where the solar wind begins to be accelerated. We performed our calculations in a potential approximation using the method of Hoeksema and Obridko [22, 23], neglecting the influence of the solar environment. The calculation results are presented in two forms. For comparison with the geometry of the transition region, we determined the absolute values of the vertical components of the magnetic field at the source surface $|B_R|$, whose coordinates were fit to the position of the radio source when the inner boundary R_{in} of the transition region was observed. In addition, we used data specifying open or closed magnetic structures to trace the frozen-in magnetic field penetrating the solar-wind
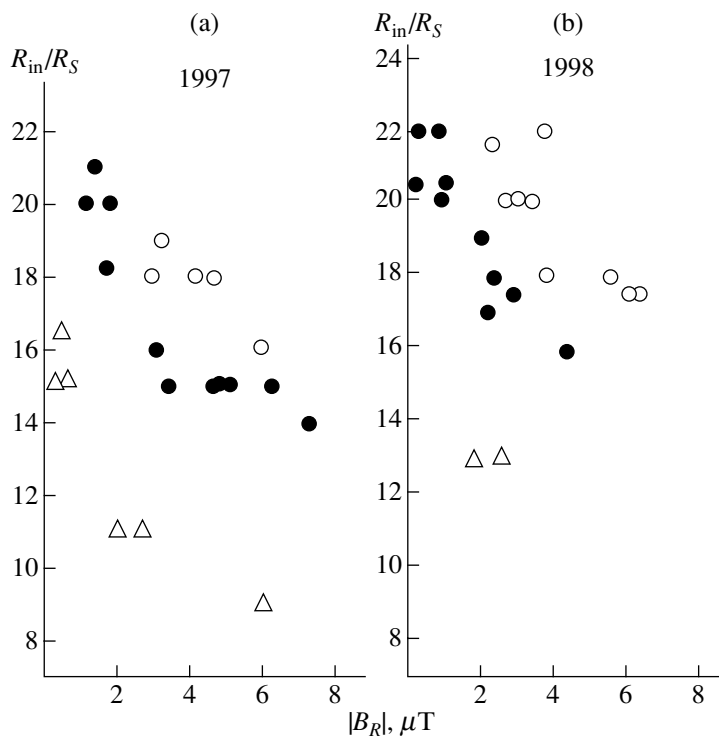
Fig. 2. Correlation between the inner boundary R_{in} of the solar-wind transition region and the strength of coronal magnetic fields $|B_R|$ at $R = 2.5R_S$ for (a) 1997 and (b) 1998.

flow. Fitting the coordinates when calculating $|B_R|$ assures that $|B_R|$ and R_{in} belong to the same solar-wind stream line. The quantity $|B_R|$ corresponds to the onset of the acceleration, while R_{in} describes its intensity. The more intense the acceleration, the closer the inner boundary corresponding to the beginning of the transition to supersonic velocities is to the Sun [24].

Below, we study processes associated with the main acceleration of the solar wind, at $R = 10–40R_s$, in the regions of the interplanetary medium that are closest to the Sun, where deviations from the radial direction can be neglected for the quiescent solar wind. We should also bear in mind that we are studying large-scale solar-wind structures, with angular sizes $\gtrsim 2.6'$ [1]; this estimate is associated with the angular resolution of experiments. In addition, this region of the interplanetary plasma coincides with that observed by SOHO, supplying us with images of the stream structure of the flow [25, 26], which, in general, confirm the soundness of our approach. The correlation analysis presented below based on a large amount of experimental data also confirms the validity of this approach.

In all, we obtained 22 pairs of $|B_R|$ and R_{in} estimates for 1997 (Fig. 2a) and 22 pairs for 1998 (Fig. 2b, the table). The table presents the radio sources used, dates of R_{in} measurements, coordinates

of the inner boundary of the transition region (the E/W hemisphere, heliolatitude φ, and radial distance from the Sun R_{in}/R_S), and corresponding $|B_R|$ values. The two last columns give the structures of the magnetic field (open, closed, or intermediate) and of the white-light corona visible in optical observations. The table does not immediately demonstrate any correlations between the magnetic-field strength and the geometry of the transition region. Nevertheless, the magnetic-field topologies and optical data enable us to distinguish three types of plasma flows, each of which shows an obvious correlation between the magnetic field $|B_R|$ and inner boundary R_{in} of the transition region (Fig. 2).

Type 1 (experiments 1, 2 in the table, triangles in Fig. 2). The magnetic-field lines escape into interplanetary space directly from the source surface, and the transition region is the closest to the solar surface. As was shown earlier [24], this structure exhibits a low level of turbulence and high flow velocities. The optical observations indicate that solar-wind stream lines start at the lateral lobes of streamers. This is rather unexpected, since streamers were not considered earlier as possible sources of high-speed flows of solar wind [5, 11]. This suggests that the lateral lobes of streamers differ considerably from their main bodies.

Solar-wind stream structures from radio, coronal magnetic field, and white-light coronal data for 1998

No.	Source	Date (1998)	E/W	φ	R_{in}/R_S	$|B_R|,$ μ T	Structure of magnetic field B_R	Structure of white-light corona
1	W28A2(1)	Dec. 12	E	−8.0	13.0	1.86	Open	Lateral lobe of streamer
2	W28A2(1)	Dec. 25	W	−10.0	13.0	2.61	−	−
3	3C 2	March 27	W	−5.0	20.5	0.19	Closed	Streamer
4	3C 166	June 28	E	−26.0	17.0	2.33	−	−
5	3C 144	June 21	W	−7.0	20.5	1.15	−	−
6	3C 154	June 20	E	24.2	19.0	2.11	−	−
7	3C 208	Aug. 09	W	−32.0	22.0	0.23	−	−
8	3C 215	Aug. 13	W	5.4	22.0	0.96	−	−
9	3C 225	Aug. 10	E	−2.0	20.0	1.00	−	−
10	GGD4	June 22	W	13.0	17.5	2.98	−	−
11	S252A	June 27	W	−31.0	16.0	4.43	−	−
12	IRC-20431	Dec. 28	W	6.0	18.0	2.41	−	−
13	3C 5	March 19	E	−6.0	20.0	2.76	Intermediate	Radial
14	3C 144	June 10	E	−23.0	17.5	6.06	−	−
15	3C 212	Aug. 11	W	−20.0	24.0	1.80	−	−
16	3C 228	Aug. 23	W	13.0	21.5	2.31	−	−
17	S252A	June 18	E	−38.5	20.0	2.98	−	−
18	U Ori	June 17	E	−45.0	20.0	3.18	−	−
19	U Ori	June 24	W	−38.5	17.5	6.31	−	−
20	IRC-20431	Dec. 19	E	21.0	18.0	5.65	−	−
21	W31(2)	Dec. 19	E	43.0	22.0	3.83	−	−
22	W31(2)	Dec. 27	W	38.0	18.0	3.81	−	−

Type 2 (experiments 3−12 in the table, dark circles in Fig. 2). The magnetic-field structure is closed, field lines become loop-like within radial distances of $(2-3)R_S$, and the transition region is further from the Sun. This structure exhibits higher turbulence and lower flow velocities. According to the SOHO data on the white-light corona, the solar-wind streams start at the main bodies of streamers.

Type 3 (experiments 13−22 in the table, empty circles in Fig. 2). The magnetic-field structure is intermediate, including both open and loop-like configurations. The transition region is the most distant from the Sun, and the flow velocities are lowest. Optical observations of the solar corona show the presence of an extended, amorphous area with high luminosity (LASCO 3). At higher resolution, this area displays fine radial structure (LASCO 2). Figure 2

shows that $|B_R|$ and R_{in} are obviously correlated in each of the three groups of observations: a decrease in the magnetic-field strength is accompanied by lower solar-wind acceleration and a more distant position of the transition region. The difference between the distances along the vertical axis in Fig. 2 for the second and third groups of observations is modest, but the significant difference in their coronal structures indicated by the SOHO data shows that they correspond to different types of solar-wind flow.

Taking into account the correlation presented in [24], we conclude that the different types of solar-wind flows are associated with the structures of magnetic fields in the near environment of the Sun. There is no doubt that the observed correlations are due to frozen-in magnetic fields and the penetration of these fields and plasma flows into interplanetary space. We
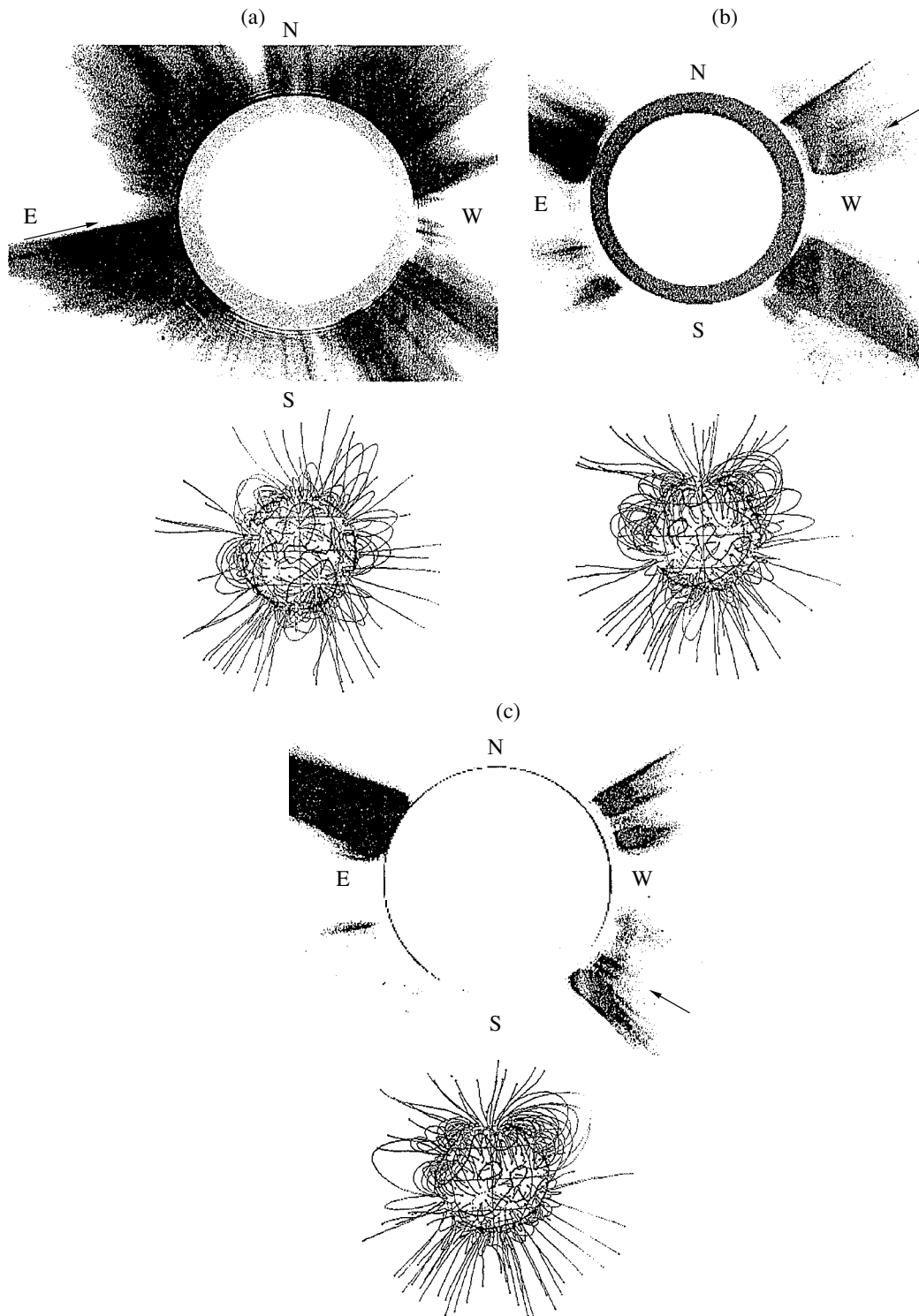
Fig. 3. Structures of the white-light corona and magnetic field for three types of solar wind flow. The results are for experiments (numbers correspond to the table) (a) 1, (b) 10, and (c) 19.

can see in Fig. 2 that variations of $|B_R|$ are not very large and lie in the range $1-7$ μT. This means that the magnetic-field topology (i.e. , open or closed) is the determining factor, rather than the magnetic-field

strength in the corona $|B_R|$. Figure 3 illustrates the three types of solar-wind flows. Each is characterized by an image of the solar corona (obtained by SOHO) and a corresponding diagram of the magnetic-field

lines. The arrows show the directions of the line of sight of the radio telescope during observations of the boundary of the transition region. The magnetic-field diagrams were constructed using initial points evenly distributed over the solar surface ($R = R_S$). Figure 3 illustrates the fundamental distinctions in the structures of the solar corona and magnetic fields, which directly lead to significant differences between the structures of the solar-wind flows.

The 1998 observations confirm the existence of three types of flows revealed in the earlier 1997 observations (Figs. 2a, 2b). In addition, Fig. 2 displays the evolution of the solar-wind flow structure in years when the solar activity is increasing. In 1998, the number of high-speed solar-wind flows had significantly decreased in comparison with 1997. The number of low-speed flows originating at streamers remained virtually constant, while the number of flows with the lowest speeds, which are not associated with streamers, considerably increased. A comparison of the radio map in Fig. 1 with that for 1997 [25] confirms this evolution. In 1998, the boundary of the transition region had moved away from the Sun, due to the dominance of intermediate magnetic structures accompanied by a decrease in the intensity of plasma acceleration in years of higher solar activity.

4. CONCLUSIONS

Our joint study of the position of the inner boundary of the solar-wind transition region R_{in} and the magnetic-field strength in the corona $|B_R|$ at a radial distance of $2.5R_S$ has revealed a correlation between these quantities. When $|B_R|$ is higher, the boundary of the transition region R_{in} lies closer to the Sun. This correlation divides into three branches corresponding to three types of magnetic-field structures in the solar corona near the sources of the solar wind. These three types of magnetic fields are associated with three types of solar-wind flows with considerably different intensities of acceleration. It is well established that powerful sources of high-speed solar wind are associated with polar coronal holes, as well as with local coronal holes at moderate heliolatitudes. Our work has identified sources of high-speed solar-wind flows located at the lateral lobes of streamers, also situated at moderate heliolatitudes. We have also verified that the main bodies of streamers are the usual sources of low-speed solar-wind flows. Regions with intermediate magnetic-field structures including both open and loop-like field lines prove to be a third source of solar-wind, creating flows with the lowest speeds. The white-light corona does not display streamers in these structures and instead has extended areas of intense luminosity, which exhibit fine radial structures at higher resolution.

REFERENCES

1. N. A. Lotova, V. N. Obridko, and K. V. Vladimirskii, Astron. Astrophys. **357**, 1051 (2000).
2. A. S. Krieger, A. F. Timothy, and E. C. Roelof, Sol. Phys. **29**, 505 (1973).
3. W. M. Neupert and V. Pizzo, J. Geophys. Res. **79**, 3701 (1974).
4. A. I. Efimov, I. V. Chasheĭ, V. I. Shishov, and O. I. Yakovlev, Kosm. Issled. **28**, 581 (1990).
5. R. Schwenn, *Physics of the Inner Heliosphere,* Ed. by R. Schwenn and E. Marsch (Springer-Verlag, Berlin, 1990), Vol. 2, p. 99.
6. M. Kojima and T. Kakinuma, Space Sci. Rev. **53**, 173 (1990).
7. B. J. Rickett and W. A. Coles, J. Geophys. Rev. **96**, 1717 (1991).
8. A. I. Efimov, Space Sci. Rev. **70**, 397 (1994).
9. A. P. Rao, S. Ananthakrishnan, V. Balasubramanian, *et al.*, AIP Conf. Proc. **383**, 511 (1996).
10. M. Tokumaru, H. Mori, T. Tanaka, *et al.*, J. Geomagn. Geoelectr. **47**, 1113 (1995).
11. I. S. Veselovsky and O. A. Panasenko, Phys. Chem. Earth (C) **25** (1-2), 113 (2000).
12. N. A. Lotova, D. F. Blums, and K. V. Vladimirskii, Astron. Astrophys. **150**, 266 (1985).
13. N. A. Lotova, Sol. Phys. **117**, 399 (1988).
14. R. D. Ekers and L. T. Little, Astron. Astrophys. **10**, 310 (1971).
15. N. A. Lotova, in *Proc. 3rd COSPAR Colloquium: Solar Wind Seven,* Ed. by E. Marsch and R. Schwenn (Pergamon, Oxford, 1992), Vol. 3, p. 217.
16. J. W. Armstrong and R. Woo, Astron. Astrophys. **103**, 415 (1981).
17. S. L. Scott, W. A. Coles, and G. Bourgois **123**, 207 (1983).
18. L. D. Landau and E. M. Lifshitz, *Course of Theoretical Physics,* Vol. 6: *Fluid Mechanics* (Nauka, Moscow, 1986; Pergamon, New York, 1989).
19. N. A. Lotova, A. A. Rashkovetskiĭ, P. B. Kazimirskiĭ, *et al.*, Astron. Zh. **66**, 114 (1989) [Sov. Astron. **33**, 61 (1989)].
20. N. A. Lotova and K. V. Vladimirskii, Sol. Phys. **172**, 225 (1997).
21. P. Janardhan, M. K. Bird, P. Edenhofer, *et al.*, Sol. Phys. **184**, 157 (1999).

22. J. T. Hoeksema, J. M. Wilcox, and P. H. Scherrer, J. Geophys. Res. **87**, 1033 (1982); **88**, 9910 (1983).

23. V. N. Obridko and B. D. Shelting, Sol. Phys. **137**, 167 (1992); **184**, 187 (1999).

24. N. A. Lotova, K. V. Vladimirskiĭ, I. Yu. Yurovskaya, and O. A. Korelov, Astron. Zh. **72**, 757 (1995) [Astron. Rep. **39**, 675 (1995)].

25. N. R. Sheely, Jr., Y.-M. Wang, S. H. Hawleg, *et al.*, Astrophys. J. **484**, 472 (1997).

26. N. Srivastava, R. Schwenn, B. Inhester, *et al.*, in *Proc. 9th International Solar Wind Conference*: *Solar Wind Nine,* Ed. by S. R. Habbal, R. Esser, J. V. Hollweg, and P. A. Insenberg, AIP Conf. Proc. **471**, 115 (1999).

27. N. A. Lotova, K. V. Vladimirskii, and V. N. Obridko, Phys. Chem. Earth (C) **25** (1-2), 121 (2000).

Translated by V. Badin